

Center for Photonics and Quantum Materials, Skolkovo Institute of Science
and technology
Department of Applied Physics, Aalto University

Advanced synthesis of single-walled carbon nanotube films by aerosol CVD method for electro-optical applications

Vsevolod Ya. Iakovlev

Skoltech

Skolkovo Institute of Science and Technology

A” Aalto University

DOCTORAL
DISSERTATIONS

Skolkovo Institute of Science and Technology / Doctoral Program in Physics
DOCTORAL THESIS

Advanced synthesis of single-walled carbon nanotube films by aerosol CVD method for electro-optical applications

Vsevolod Ya. Iakovlev

- Supervisors:** Professor Albert G. Nasibulin,
Skolkovo Institute of Science and Technology, Russia
Professor Esko I. Kauppinen, Aalto University, Finland
- Defense Jury:** Professor Keith Stevenson (Chairman), Skolkovo Institute of
Science and Technology, Russia
Professor Krisztian Kordas, University of Oulu, Finland
Professor Georgy E. Fedorov, Moscow Institute of Physics
and Technology, Russia
Assistant Professor Toma Susi, University of Vienna, Austria
Professor Sergey D. Shandakov, Kemerovo State University,
Russia
Professor Alexander V. Okotrub, Novosibirsk State University
Russia
- Date & Time:** October 4, 13:00
- Venue:** Skolkovo Institute of Science and Technology, 30,
Bolshoi Boulevard, bld. 1, Room B4-3007a

Author

Vsevolod Ya. Iakovlev

Name of the doctoral dissertation

Advanced synthesis of single-walled carbon nanotube films by aerosol CVD method for electro-optical applications

Publisher School of Science

Unit Department of Applied Physics

Series Aalto University publication series DOCTORAL DISSERTATIONS / 177/2019

Field of research Engineering Physics

Manuscript submitted 18 June 2019

Date of the defence 4 October 2019

Permission for public defence granted (date) 11 September 2019

Language English

Monograph

Article dissertation

Essay dissertation

Abstract

Single-walled carbon nanotubes (SWCNTs) are of a unique family of materials emerging high-performance applications in electronics and optoelectronics. However, despite significant progress over the last 25 years, the problem of SWCNT production with tailored characteristics, the absence of the growth models and post-synthesis methods to improve specific SWCNT properties are still the main barriers towards a wide range of applications. The methods of the SWCNT synthesis, data processing and SWCNT treatment developed so far are still not fully optimized.

In the current thesis, the abovementioned problems were addressed with the following demonstration of advanced applications of SWCNT films:

A new reactor for the aerosol CVD growth of SWCNTs equipped with a spark discharge generator of catalyst nanoparticles was developed. The design proposed resulted in a robust apparatus when compared with the ferrocene CVD reactor. The stability and scalability of the SWCNT synthesis are the main benefits of the spark discharge generator.

An advanced control on the diameter distribution, defectiveness, and the yield for the first time was achieved through the use of the artificial neural networks (ANN). This allowed us to achieve a precise control towards mutual relation between the reactor parameters and key SWCNT characteristics. The methodology proposed can help with adjusting the diameter distribution, yield and quality of SWCNTs with prediction error 4%, 14%, 23% respectively for very a limited data set.

A novel technique for the post-synthesis improvement of electro-optical characteristics of SWCNT films by a laser treatment was proposed. In this process by a short pulse laser irradiation, the transparency of SWCNT films increases without any changes in conductivity presumably due to the oxidation of the catalyst particles. We improved transparency by 4%, and decreased equivalent sheet resistance by 21%.

All developed techniques and methods contributed to the synthesis of SWCNTs with defined characteristics open a new possibility for their applications. Thesis work includes three different electro-optical devices with advanced performance: i) a bolometer based on a freestanding SWCNT film showing response time of 2.6 ms at room temperature and 1 mbar (several times faster than the corresponding industrially applied devices); ii) an SWCNT-based heating element of fiber Bragg grid for smooth tuning of the resonant wavelength and a stable laser signal; iii) a saturable absorber based on SWCNT films showing femtosecond pulse generation and low degradation rate.

Keywords SWCNT, spark discharge generator, artificial neural networks, CVD, synthesis

ISBN (printed) 978-952-60-8739-9

ISBN (pdf) 978-952-60-8740-5

ISSN (printed) 1799-4934

ISSN (pdf) 1799-4942

Location of publisher Helsinki

Location of printing Helsinki

Year 2019

Pages 159

urn [http://urn.fi/URN:ISBN: 978-952-60-8740-5](http://urn.fi/URN:ISBN:978-952-60-8740-5)

Supervising professors

Esko I. Kauppinen, Aalto University, Finland

Albert G. Nasibulin, Skolkovo Institute of Science and Technology, Russia

Thesis advisor

Dr. Dmitry V. Krasnikov, Skolkovo Institute of Science and Technology, Russia

Preliminary examiners

Professor Krisztian Kordas, University of Oulu, Finland

Professor Georgy E. Fedorov, Moscow Institute of Physics and Technology, Russia

Opponent

Professor Krisztian Kordas, University of Oulu, Finland

Aalto University publication series
DOCTORAL DISSERTATIONS /

© Vsevolod Ya. Iakovlev

ISBN 978-952-60-8739-9 (printed)

ISBN 978-952-60-8740-5 (pdf)

ISSN 1799-4934 (printed)

ISSN 1799-4942 (pdf)

[http://urn.fi/URN:ISBN: 978-952-60-8740-5](http://urn.fi/URN:ISBN:978-952-60-8740-5)

Unigrafia Oy
Helsinki 2019

Finland



Printed matter
4041-0619

ACKNOWLEDGMENTS

Many people to whom I am thankful have directly or indirectly contributed to the creation of my thesis. First and foremost, this work would have been impossible without my PhD supervisors, Professor Albert Nasibulin and Professor Esko Kauppinen. Over the past years they guided me in my study and taught how to do high level scientific research. Your advices will serve me well during all my life. I would like also to thank my jury members, and all committee for kindly accepting to read this thesis. I am very grateful to my thesis advisor Dr. Dmitry Krasnikov for taking care about all my questions and becoming my true friend. I thank all my colleagues and coauthors Y.A. Sklyueva, Dr. F. S. Fedorov, E. M. Khabushev, J. V. Kolodiazhaia, A. A. Alekseeva, A. K. Grebenko, A. P. Tsapenko, B. Y. Zabelich, Dr. Y. G. Gladush, Dr. D. S. Kopylova, A. A. Mkrtyan. I am grateful for your support and helpful discussions. I would like also to thank the education office for the administrative support. I am grateful to Aalto University and to Skolkovo Institute of Science and Technology. And many thanks to my family and friends

This research was supported by the Russian Science Foundation No. 17-19-01787. Skoltech Biomedical Initiative project (No 2017-7/SBI) is acknowledged for the financial support.

CONTENT

| | |
|--|-----|
| ACKNOWLEDGMENTS | I |
| CONTENT | II |
| THESIS PUBLICATIONS | III |
| AUTHOR'S CONTRIBUTION | IV |
| SYMBOLS AND ABBREVIATIONS | V |
| 1. INTRODUCTION | 1 |
| 2. CARBON NANOTUBES | 4 |
| 2.1. STRUCTURE | 4 |
| 2.2. OPTOELECTRICAL PROPERTIES OF CNT FILMS | 7 |
| 2.3. METHODS FOR SWCNT SYNTHESIS | 11 |
| 2.4. OPTOELECTRONIC APPLICATIONS OF SWCNT FILMS | 14 |
| 3. CHARACTERIZATION TECHNIQUES | 17 |
| 3.1. SPECTROSCOPIC METHODS | 17 |
| 3.1.1. UV-VIS-NIR SPECTROSCOPY | 17 |
| 3.1.2. FOURIER TRANSFORM INFRARED SPECTROSCOPY | 19 |
| 3.1.3. X-RAY PHOTOELECTRON SPECTROSCOPY | 20 |
| 3.1.4. RAMAN SPECTROSCOPY | 20 |
| 3.2. MICROSCOPIC METHODS | 22 |
| 3.2.1. SCANNING ELECTRON MICROSCOPY | 22 |
| 3.2.2. TRANSMISSION ELECTRON MICROSCOPY | 23 |
| 3.2.3. ATOMIC FORCE MICROSCOPY | 23 |
| 3.3. ELECTRICAL PROPERTIES | 23 |
| 3.4. AEROSOL STUDIES | 24 |
| 3.5. THERMOGRAVIMETRIC ANALYSIS | 25 |
| 4. SWCNT GROWTH | 26 |
| 4.1. FERROCENE REACTOR | 26 |
| 4.2. SPARK DISCHARGE GENERATOR REACTOR | 27 |
| 4.3. INFLUENCE OF THE DISCHARGE PARAMETERS | 29 |
| 4.4. THE ROLE OF TEMPERATURE AND CO ₂ CONTENT | 38 |
| 5. DATA ANALYSIS AND PROCESSING | 47 |
| 5.1. DATA PREPARATION | 47 |
| 5.2. DESIGN OF ANN MODEL | 49 |
| 5.3. PERFORMANCE VALIDATION OF ANN | 51 |
| 6. LASER TREATMENT OF SWCNT FILMS | 54 |
| 7. APPLICATIONS OF THIN FILMS | 59 |
| 7.1. BOLOMETERS | 59 |
| 7.2. SATURABLE ABSORBERS | 63 |
| 7.3. FIBER BRAGG GRATINGS | 68 |
| 8. CONCLUSIONS | 73 |
| 9. REFERENCES | 74 |
| APPENDIX: SWCNT SYNTHESIS CONDITIONS | 83 |

THESIS PUBLICATIONS

I. **VY Iakovlev**, YA Sklyueva, FS Fedorov, DP Rupasov, Improvement of optoelectronic properties of single-walled carbon nanotube films by laser treatment, *Diamond and Related Materials* (2018), 88, 144.

II. **VY Iakovlev**, DV Krasnikov, EM Khabushev, JV Kolodiaznaia, AG Nasibulin, Artificial neural network for controlled synthesis of single-walled carbon nanotubes by aerosol CVD method, *Carbon* (2019), 153, 100.

III. **VY Iakovlev**, DV Krasnikov, EM Khabushev, AA Alekseeva, NI. Raginov, AK Grebenko, AP Tsapenko, BY Zabelich, JV Kolodiaznaia, AG Nasibulin, A comparative study of ferrocene and spark-discharge aerosol CVD reactors for single walled carbon nanotube growth: the role of ex situ nucleation, *Chemical Engineering Journal* (2019), submitted (15 pages).

IV. DV Krasnikov, BY Zabelich, **VY Iakovlev**, AP Tsapenko, SA Romanov, AA Alekseeva, AK Grebenko, AG Nasibulin, A spark discharge generator for scalable aerosol CVD synthesis of single-walled carbon nanotubes with tailored characteristics, *Chemical Engineering Journal* (2019), V. 372, 462.

V. DS Kopylova, NY Boldyrev, **VY Iakovlev**, YG Gladush, AG Nasibulin, A bolometer based on single-walled carbon nanotubes and hybrid materials, *Quantum Electronics* (2016), 46, 1163.

VI. YG Gladush, OI Medvedkov, SA Vasil'ev, DS Kopylova, **VY Yakovlev**, AG Nasibulin, Control over the resonance wavelength of fiber Bragg gratings using resistive coatings based on single-wall carbon nanotubes, *Quantum Electronics* (2016), 46, 919.

VII. AA Mkrtyan, YG Gladush, DI Galiakhmetova, **VY Yakovlev**, VT Ahtyamov, AG Nasibulin, Dry-transfer technique for polymer free single-walled carbon nanotube saturable absorber on a side-polished fiber, *Optical materials express* (2019), 9, 1551.

AUTHOR'S CONTRIBUTION

- **VY Iakovlev**, YA Sklyueva, FS Fedorov, DP Rupasov, Improvement of optoelectronic properties of single-walled carbon nanotube films by laser treatment, *Diamond and Related Materials* (2018), 88, 144.

- Fabrication of samples, treatment process, electrical and optical characterization, data analysis, preparation of the manuscript.

- **VY Iakovlev**, DV Krasnikov, EM Khabushev, JV Kolodiazhnaia, AG Nasibulin, Artificial neural network for controlled synthesis of single-walled carbon nanotubes by aerosol CVD method, *Carbon* (2019), 153,100.

- The design of a reactor, optical characterization, data processing, methodology development, preparation of the manuscript.

- **VY Iakovlev**, DV Krasnikov, EM Khabushev, AA Alekseeva, NI. Raginov, AK Grebenko, AP Tsapenko, BY Zabelich, JV Kolodiazhnaia, AG Nasibulin, A comparative study of ferrocene and spark-discharge aerosol CVD reactors for single-walled carbon nanotube growth: the role of ex situ nucleation, *Chemical Engineering Journal* (2019), submitted (15 pages).

- Design of a reactor, optical characterization, fabrication of samples, data preparation, preparation of manuscript.

- DV Krasnikov, BY Zabelich, **VY Iakovlev**, AP Tsapenko, SA Romanov, AA Alekseeva, AK Grebenko, AG Nasibulin, A spark discharge generator for scalable aerosol CVD synthesis of single-walled carbon nanotubes with tailored characteristics, *Chemical Engineering Journal* (2019), V. 372, 462.

- Development of reactor concept, assembly of setup, tuning of SDG, discussion of the results.

- DS Kopylova, NY Boldyrev, **VY Iakovlev**, YG Gladush, AG Nasibulin, A bolometer based on single-walled carbon nanotubes and hybrid materials, *Quantum Electronics* (2016), 46, 1163.

- Synthesis and optimization of SWCNTs, sample fabrication, discussion of the results.

- YG Gladush, OI Medvedkov, SA Vasil'ev, DS Kopylova, **VY Yakovlev**, AG Nasibulin, Control over the resonance wavelength of fiber Bragg gratings using resistive coatings based on single-wall carbon nanotubes, *Quantum Electronics* (2016), 46, 919.

- Synthesis and optimization of SWCNT properties, sample fabrication, electrical and optical characterization, discussion of the results.

- AA Mkrtychyan, YG Gladush, DI Galiakhmetova, **VY Yakovlev**, VT Ahtyamov, AG Nasibulin, Dry-transfer technique for polymer-free single-walled carbon nanotube saturable absorber on a side polished fiber, *Optical materials express* (2019), 9, 1551.

- Synthesis and optimization of SWCNT properties, sample fabrication, optical sample characterization, discussion of the results.

SYMBOLS AND ABBREVIATIONS

| | |
|------------|--|
| 0D | 0-dimensional |
| 1D | 1-dimensional |
| 2D | 2-dimensional |
| AFM | Atomic force microscopy |
| ANN | Artificial neural network |
| CVD | Chemical vapor deposition |
| DMA | Differential mobility analyzer |
| DOS | Density of states |
| DTA | Differential thermal analysis |
| FBGs | Fiber Bragg gratings |
| FTIR | Fourier transform infrared |
| FWHM | Full width at half maximum |
| HiPCO | High pressure CO |
| HML | Harmonic mode-lock |
| IR | Infrared |
| ITO | Indium tin oxide |
| LPFG | Long-period fiber grating |
| NEP | Noise-equivalent power |
| PDL | Polarization depended losses |
| PMMA | Polymethyl methacrylate |
| RBM | Radial breathing modes |
| SA | Saturable absorbers |
| SDG | Spark discharge generator |
| SEM | Scanning electron microscopy |
| SESAM | Semiconductor saturable absorber mirror |
| SMF28 | Standard single-mode fiber |
| SWCNT | Single-walled carbon nanotube |
| TEM | Transmission electron microscopy |
| TGA | Thermogravimetric analysis |
| UV-vis-NIR | Ultra-violet, visible and near infra-red |
| XPS | X-ray photoelectron spectroscopy |

1. INTRODUCTION

All human history is strongly connected with technology: the current advances shape our lifestyle and even a vision of the future. Moving through the epochs (stone age when people get first mechanical tools, bronze age with innovative construction and military, iron changed logistics with railways and large ship), we are still examining our understanding of the limits: the planet is already too small while space is still too inhospitable. Silicon gave us electronics and changed all rules on the market of information. Now we are on the brink of a new era shaped by nanotechnology, genetic therapy, artificial intelligence. And, as in the past, materials are a basement of this age to come.

Single-walled carbon nanotubes (SWCNTs) has been one of the pioneer materials of nanotechnology attracting an extensive attention of the scientific community during the last 30 years. Due to a unique set of mechanical, optical, and electronic properties SWCNT are considered to be a promising component of various applications: from aerospace to nanoelectronics, from catalysis to construction materials. The efforts devoted to the research (> 50 000 publications since landmark publication in 1991 [1]) resulted in several methods for the nanotube synthesis. This led not only to a considerable fundamental progress [2], [3], but also to establishing of a commercial market [4] – catalytic chemical vapor deposition (CVD) in fluidized beds [5], [6], floating bed of catalyst [7], [8], high pressure CO (HiPCO) decomposition of ferrocene [9] are the methods to provide a wide variety of nanotube-based products. While a large-scale nanotube production [10] mostly relies on fluidized beds and floating catalyst reactors covering the composite and functional material applications, the fabrication of “next generation” electronics, sensors, and transparent conductors is inseparably connected with individual carbon nanotubes with predefined properties, namely chirality and length distributions, alignment, and agglomeration degree [11]. The last parameter can be even considered as a key barrier for the advanced applications as the disentanglement of the

agglomerates produced by large-scale synthesis implies a challenging task: the Van der Waals interaction usually considered to be a weak one coaxially glues two SWCNTs with an energy of about $950 \text{ eV}/\mu\text{m}$ [12] providing enough energy even for ion excitations [13]. The techniques for dispersion of carbon nanotubes developed so far (e.g. ball milling, ultrasonication, calendaring) lead either to a low degree of disentanglement or to a certain damage of carbon nanotube structure by a reduction in length or increase in defectiveness [14]. Thus, aerosol CVD [15] – the specific case of the reactor type with a floating bed of extremely diluted catalyst – is considered to be the most promising technique for the SWCNT synthesis for advanced electronic devices [11], [16], [17].

However, despite significant progress in the aerosol CVD, the problem of SWCNT production with tailored characteristics is still challenging being one of the main barriers towards a wide range of applications. The methods of SWCNT synthesis developed to date as well as techniques for post-synthesis treatment and kinetic models are still not fully optimized. This can be attributed to the following aspects. The historical development of the SWCNT synthesis technology can be characterized by a manual search of the best synthesis conditions and a local troubleshooting. However, such a strategy resulted in reduced scalability of the technologies for the SWCNT growth and poor prediction models. This can be attributed to a complex nature of the mechanisms for SWCNT nucleation, growth, and termination that complicates employment of classical analytical models. We propose an advanced method of synthesis with a stable reactor with modern design for a robust synthesis process and artificial neural networks for complex multi-parameter tasks inspiring the corresponding research.

The current thesis is devoted to the synthesis of SWCNTs with tailored characteristics: starting from a brief overview, we focus on novel approaches for SWCNT synthesis targeting on aerosol CVD, advanced data processing and further post-synthesis modification of carbon nanotubes, while the advances achieved are proven by a few pronounced electro-optical applications. At the same time, the optical transition of SWCNTs is one of the main parameters for devices like

transparent conductors, and we paid attention to the improvement of optical properties by the additional non-distractive post-synthesis method. All these steps can make SWCNT films one of the most desirable materials for electro-optical applications.

2. CARBON NANOTUBES

2.1. STRUCTURE

A unique balance between hybridization (up to four covalent bonds) and energy of C-C bonds (>300 kJ/mole) provides an enormous amount of stable combinations, while the allotropes of sp^2 nanocarbons, namely fullerenes, carbon nanotubes, and graphene can be respectively described as 0D, 1D and 2D structures (Fig. 1.1) leading to a variety of interesting peculiarities in electronic structure and, thereby, physical characteristics.

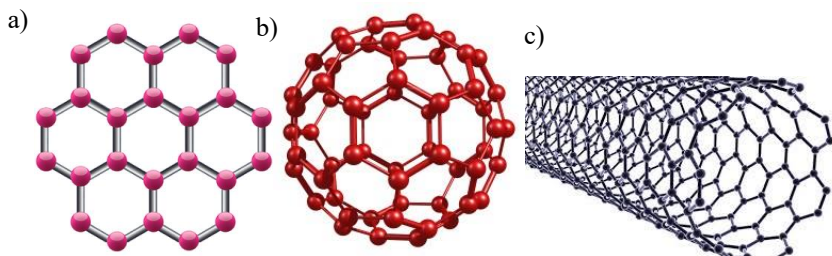


Figure 1.1: Schematic representation of a) graphene, b) fullerene, c) single-walled carbon nanotube.

A SWCNT can be represented as a graphene sheet rolled in a tube (Fig. 1.1, c) in certain circumstances with fullerene-like caps on the tips. Multi-walled carbon nanotubes can be attributed to a superposition of two extreme cases – a Russian-doll structure (Fig. 1.2, a) and spiral (Fig. 1.2, b). Moreover, the structure can be affected by defects leading to partially disordered (the most experimentally abundant; Fig. 1.2, c) or polygonal forms (Fig. 1.2, d). These variety of structures itself allows considering carbon nanotubes as a class of materials with a wide range of properties.

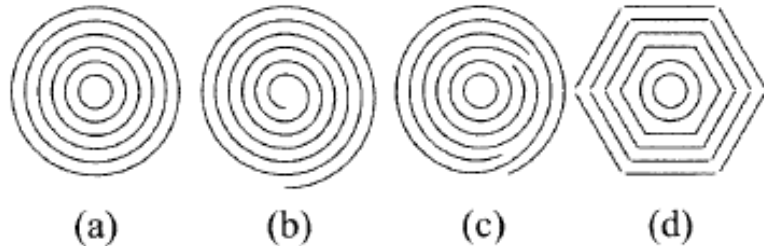


Figure 1.2: Schematic representation of different structures of multi-walled carbon nanotubes a) Russian-doll, b) spiral, c) partially disordered d) polygonal. [18]

The variety of possible nanotube structures enhances when a simple virtual rolling of a SWCNT from a graphene sheet is considered: there is an infinite number of patterns for rolling. This results not only in different SWCNT diameters but also, as it will be shown below, affects electronic and mechanical properties of carbon nanotubes to be formed. Due to 2D nature of graphene, the rolling procedure can be usually described with a pair of parameters: diameter and chirality angle (Fig. 1.3) or so-called chirality vectors (a_1 and a_2) or chirality indices (n and m). One of the most interesting features concerning the chiral aspects of carbon nanotubes is the direct relation between the chirality vectors and the band structure (Fig. 1.3): when $a_1 - a_2 = 3k$ (where k is an integer: 0, 1, 2...) a SWCNT has a bandgap $< RT$ resembling metallic properties at room temperature, while the case of $n = m$ is exceptional and considered to be truly metallic (so called armchair configuration). All the other possibilities are attributed to the semiconducting behavior at room temperature.

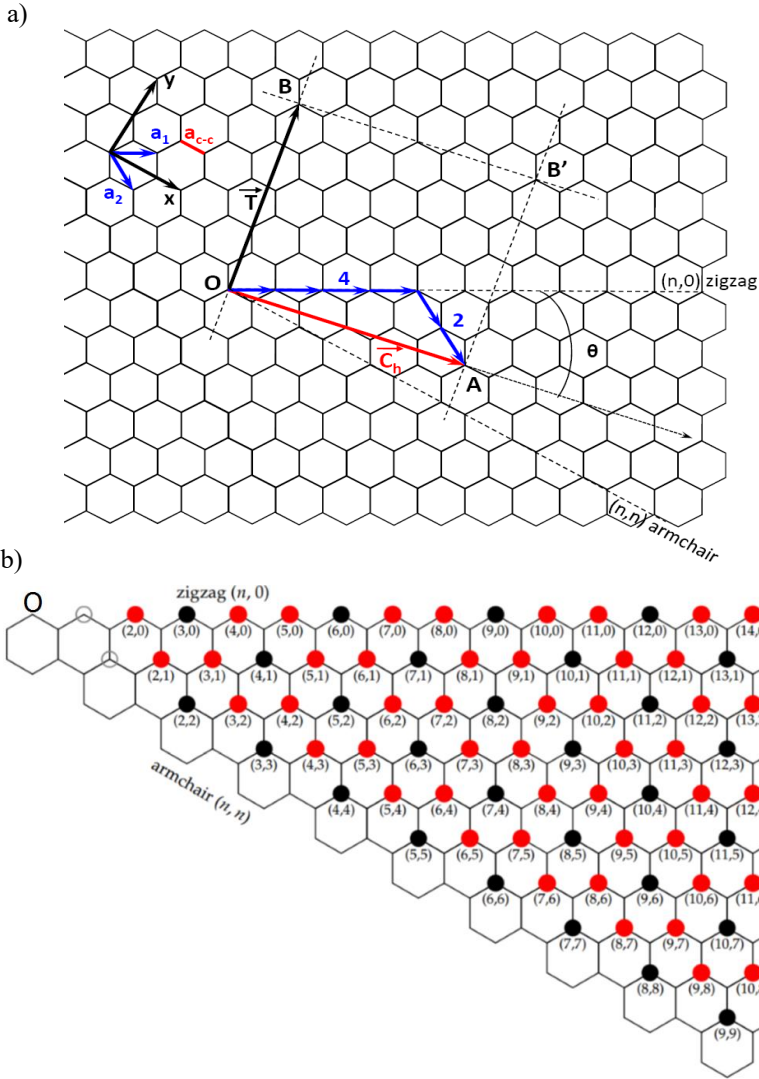


Figure 1.3: a) The unrolled honeycomb lattice of a nanotube. Determining the chiral vector and the translation vector of the nanotube, respectively. The figure corresponds to a chiral vector (4, 2) SWCNT. The chiral angle is indicated by θ , b) chirality map indexes of chirality vector marked with red and black semiconducting and metallic SWCNTs correspondingly.

The structure of a carbon nanotube defines the physical (mechanical, optical, electrical) properties forming not only a class of materials with a wide range of characteristics but also providing an opportunity to tune those properties for certain applications. For example, the chirality

distribution defines, in general, electrical conductivity of the SWCNTs. Their thin films are affected by the connections between metallic and semiconducting nanotubes that behave as Schottky barriers. As the equilibrium fraction of metallic and semiconducting nanotubes is respectively 1/3 and 2/3 [19], tuning the distribution (by targeted synthesis or by post synthesis treatment) opens an avenue for the improvement of opto-electrical properties of SWCNTs.

2.2. OPTOELECTRICAL PROPERTIES OF CNT FILMS

Carbon nanotubes were shown to provide a unique set of characteristics (e.g., high aspect ratio (up to $5 \cdot 10^8$ [20]) which results in a low percolation threshold for composites or thin films, heat conductivity up to 6600 W/(m*K) is two times higher than that of diamond, the Young's modulus up to 1 TPa is higher than that for the high strength steel) [21].

High aspect ratio combined with a certain cohesion energy provide a route for formation of thin transparent films, while the high electrical conductivity opens an avenue for a set of applications: thin film electrodes, flexible transistors, integrated circuits *etc.* Indeed, the films especially in a freestanding form [22] are mostly resemble aerogel-like structure where only a small volume fraction is occupied by the nanotubes providing a certain transparency in visible light for varying thicknesses from around hundreds of nanometers and down to the submonolayer configuration (Fig. 2.1).

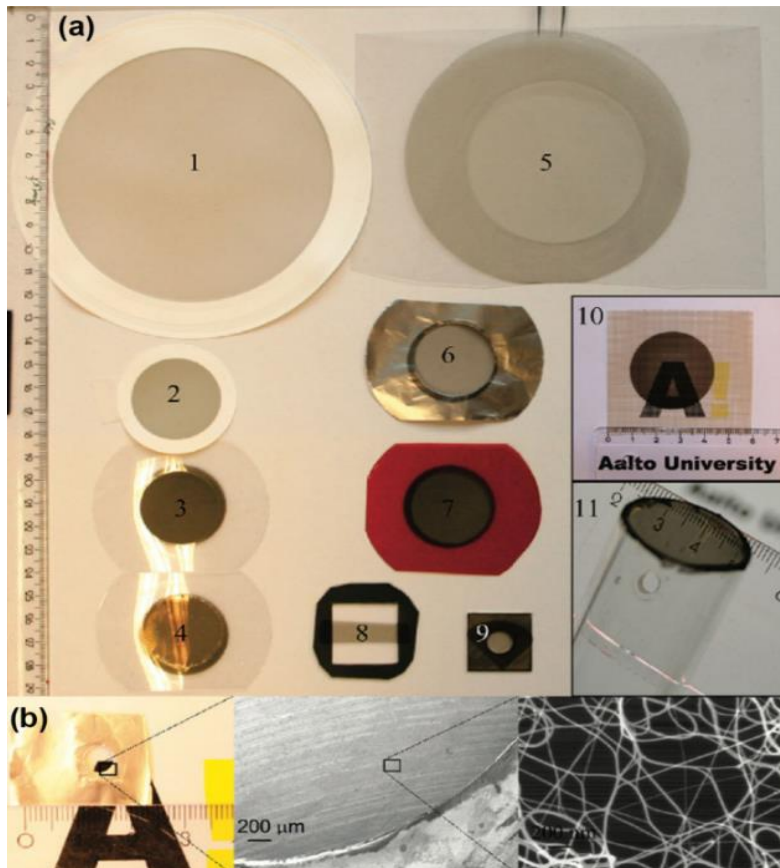


Figure 2.1: a) Free standing SWCNT films of different thicknesses over holes on different substrates, b) structure of submonolayer SWCNT film on electron microscopy [22].

The properties of thin SWCNT films are strongly connected with characteristics of individual nanotubes. The electronic properties of SWCNTs are mainly defined by Van Hove singularities – a set of levels with enormous density nearly symmetrically located with respect to the Fermi level induced mostly by 1D-like structure of carbon nanotubes. Moreover, the optic spectrum of SWCNTs is strongly affected by those singularities: the transitions between symmetric zones (so-called S_{11} , S_{22} , M_{11} , etc.) shown at Fig 2.2, are more intense in UV-vis-NIR range (200-3000 nm) presented at Fig. 2.3 when compared to other counterparts. The positions of absorption peaks are characteristic towards the SWCNT structure and mainly dependent on the chirality. However, due to the thermal broadening and doping effect (due to bundling or other chemical

8

compounds), it is impossible to unambiguously determine the chirality distribution in SWCNT samples limiting only to the diameter distribution [23]. The chirality (and, thereby, diameter) dependence of the transition energies is represented by so-called Kataura plot. Interestingly, the Kataura plot has found a “reverse” history for Raman spectroscopy, where energy (in this case laser excitation energy) defines an ensemble of the SWCNT chiralities providing resonant scattering usually observed as radial breathing modes (more information is given in section 3.1.4 “Raman spectroscopy”).

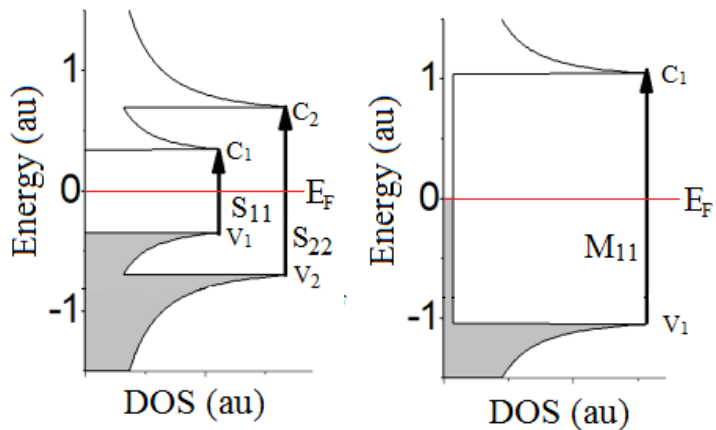


Figure 2.2: Schematic presentation of the density of states (DOS) for semiconducting (left) and metallic (right) SWCNTs. E_F – the Fermi energy [24].

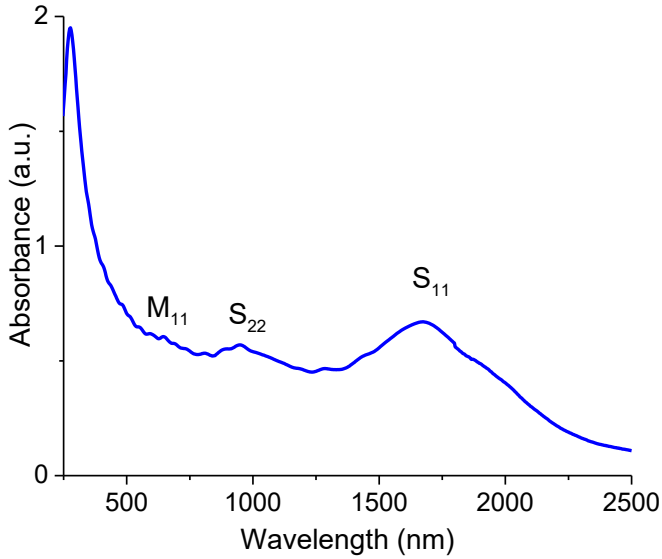


Figure 2.3: Typical absorbance spectra of SWCNT films in UV-vis-NIR range. The intraband transition bands (S_{11} , S_{22} , M_{11}) are designated.

Thin films of SWCNTs were also shown to satisfy the Beer-Lambert law [25]:

$$I = I_0 e^{-ah}, \quad (2.1)$$

where I_0 is the intensity of the incidental beam, h is the thickness of the SWCNT film, and a corresponds to the wavelength dependent absorption coefficient. This equation can be employed for estimation of the film thickness by assessment of a UV-vis-NIR spectrum [26].

Like other properties, it is the carbon nanotube structure what defines the electrooptical properties of SWCNT films in a wide range. For example, recently Liao *et al.* [27] have shown that with a certain tuning of the diameter distribution of SWCNT samples it is possible to obtain color films (Fig. 2.2).

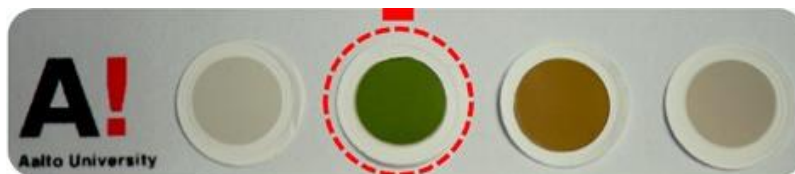


Figure 2.4: SWCNT films collected on filters. Different diameter distributions cause different colors of the films [27].

2.3. METHODS FOR SWCNT SYNTHESIS

The formation of carbon nanotubes is affected by certain aspects [28]. Being a sp^2 allotrope of graphite with melting point > 4000 K, carbon nanotubes cannot be reconstructed by a lattice diffusion under the temperatures lower *c.a.* 2600 K [29]

These factors determine the necessity of a catalyst; generally it shapes the form of a carbon precipitate, provides a route for the transformation of the carbon-containing species at temperatures lower than the melting point [30]. Methods for SWCNT production are usually classified by a route of carbon transformation: so-called physical and chemical methods.

The physical methods for the CNT growth are based on a sublimation and precipitation of carbon (Fig. 2.5) and deal with high temperature [31], [32]: arc discharge, laser ablation, and other heating-based techniques, which might result in generation of atomic carbon. The catalyst in a physical method facilitates the carbon transformation and inhibits the formation of collateral carbon species. Nevertheless, SWCNTs produced by the physical methods are obtained as bundles and agglomerates of random shape and require further separation and purification from catalyst particles and amorphous species. Moreover, the high temperature of the growth zone provides a route for reversible precipitation resulting in SWCNT samples of high quality. Being historically first to be implemented to produce gram-scale SWCNT samples, the physical methods played a great role in the development of the carbon nanotube science. However, the common poor scalability and

high relative cost of heating up to the graphite melting point inhibited their applications in industry unlike the chemical ones.

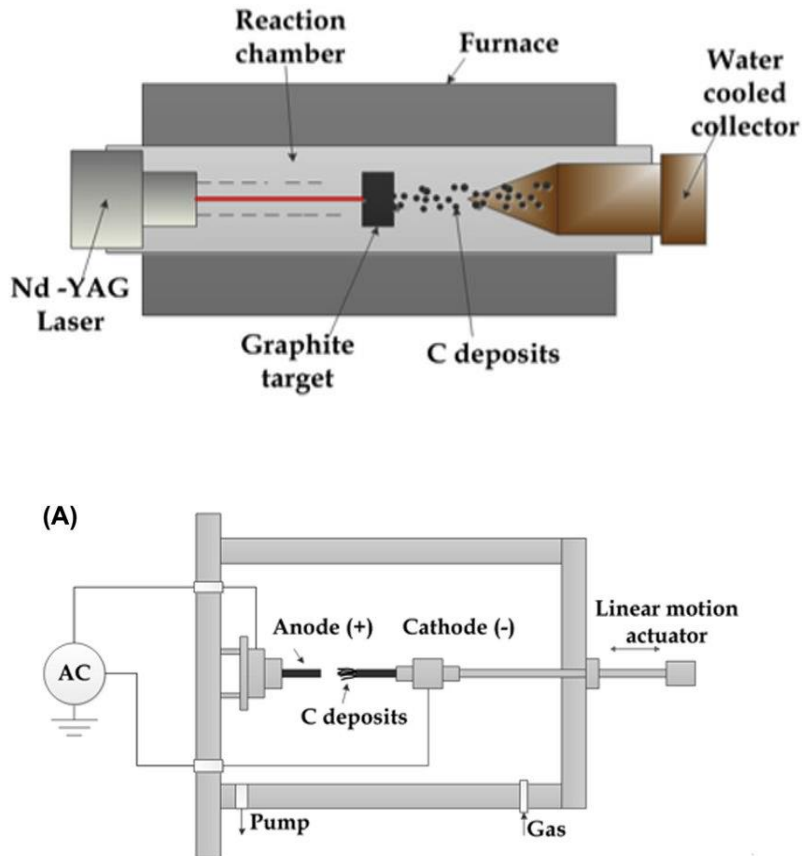


Figure 2.5: Physical methods of CNTs production laser ablation reactor for CNT synthesis, and ark discharge reactor for CNT synthesis. [33]

Chemical methods for the SWCNT synthesis are based on the catalytic decomposition of carbon-containing precursors and mostly limited to CVD technique [34]. The main advantage of this method is the possibility of the growth of carbon nanotubes at relatively low temperatures ($<1000\text{ }^{\circ}\text{C}$). Moreover, CVD provides an enhanced control towards the growth zone and the catalytic performance opening a wide variety of subclasses: plasma enhanced CVD, laser induced CVD, *etc.* When the evolution of the catalyst is considered, there are two main choices:

- substrate CVD (a catalyst constantly stays in a reactor zone);
- floating catalyst (a catalyst gradually moves through a reactor).

Generally, each of the above-mentioned techniques demonstrate its own set of strengths and weaknesses: substrate CVD provides a simple route for patterning. Moreover, the substrate CVD method can be also realized in a fluidized bed configuration, in which a catalyst on the surface of small inert particles is moving through the growth zone with subsequent removal at a certain point [5]. Then, the fluidized beds are the best for industrial high-yield synthesis of SWCNT powder while fails to yield in carbon nanotubes with predefined morphology. However, the need of the purification from the substrate makes the process of the substrate CVD method complicated. The aerosol CVD – a specific case of floating catalyst technique with extremely diluted catalyst – is not suitable for generating the product in tons while leading to individual SWCNTs with ability to provide any patterning desired.

As the thesis considers thin SWCNT films for optoelectronics the aerosol CVD is the most promising technique to be applied. Generally, in the aerosol CVD method, the growth of a SWCNT occurs on the surface of particles suspended in a gas. Fe, Ni,Co or their alloys are the most abundant catalysts. Generally, the role of a catalyst in the aerosol CVD is the accumulation of carbon from the precursor and carbon precipitation in the form of a SWCNT. A volatile hydrocarbon, an alcohol or carbon monoxide can be used as a carbon precursor in the chemical method.

Aerosol CVD method was first introduced in 1999 in the form of so-called HipCO process. During next years this method has experienced many modifications and upgrades. In 2006 Moisala *et al.* [15] proposed a vertical reactor with a continuous SWCNT growth, which operates at atmospheric pressure (Fig. 2.6) and employs ferrocene as a catalyst precursor. They also improved methods of collecting samples, introduced the method of formation of thin homogenous films based on randomly oriented nanotubes and their transfer to the substrate or in free-standing film configuration.

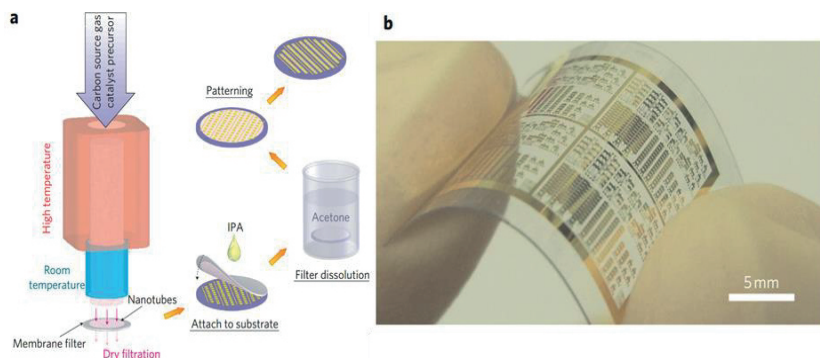


Figure 2.6: a) scheme of aerosol method of synthesis and sample transfer, b) flexible substrate with metal electrodes and SWCNTs [35].

Thus, to date, a number of methods there have been developed for the SWCNT growth. Due to a great variety of possible SWCNT applications and a need for nanotubes with a set of properties specifically optimized for each particular device, each synthesis method finds a certain niche. To obtain thin SWCNT films for advanced electro-optical appliances, the aerosol CVD is employed in this work as the most promising method. However, due to the complex relation between the synthesis conditions and the nanotube, the problem of optimally organizing the aerosol CVD reactor is still challenging.

2.4. OPTOELECTRONIC APPLICATIONS OF SWCNT FILMS

The unique combination of electronic, structural, and optical properties of SWCNT films leads to various optoelectronic devices and components. One of the most popular applications is transparent electrodes, which have recently become one of the main candidates for replacing indium tin oxide (ITO). Unlike ITO, SWCNTs can be used for the creation of flexible and stretchable conductors. The advantage of SWCNT films is compatibility with flexible polymers, as well as with glass, quartz, silicon. Despite significant progress during the last decade, current advance to 42 Ohm/sq. with a transparency of 90% is still inferior to ITO performance. However, the theoretical estimations predict the

SWCNT films with specifically predefined structure and morphology to outrun the current competitor.

SWCNT films can be used as optically transparent chemical electrodes. Combination of high conductivity, high surface, and electrocatalytic activity in many electrochemical reactions make this material more and more popular in electrochemistry [36].

Recently, solar cells based on amorphous or polycrystalline silicon and SWCNT films used as a transparent window electrode and active p-type layer have shown a superior efficiency in a rigid form and as in flexible devices [37].

Bolometers (photodetectors), where SWCNT films used as a sensing material, are a novel class of devices, which allow to measure the intensity of the infrared wavelength radiation by means of resistance change of the material under its heating [38].

Transistors based on both individual and SWCNT films owe the semiconducting band structure and high mobility which is a promising set of properties in combination with a simple production technique when compared to Si-based transistors [39].

Saturable absorbers are a key component for mode-locking femtosecond lasers. Their working principle is based on non-linear absorption of the light in the material. Single-walled carbon nanotube films have been already developed and demonstrated in the laser applications [40].

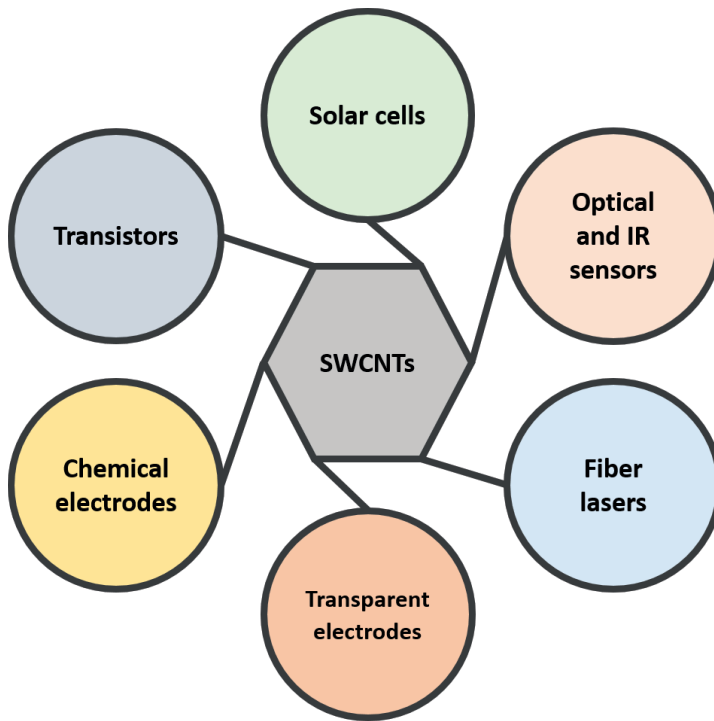


Figure 2.7: Fields of potential applications of SWCNT films.

Single-walled carbon nanotubes show the potential to become one of the central materials of next-generation optoelectronics (Fig. 2.7). However, as each application requires precise control over SWCNT structure, a solution for nanotubes with tailored characteristics becomes crucial.

3. CHARACTERIZATION TECHNIQUES

In order to obtain a reliable technique for the synthesis of single-walled carbon nanotubes with tailored characteristics, a comprehensive set of methods was employed within the thesis.

3.1. SPECTROSCOPIC METHODS

3.1.1. UV-VIS-NIR SPECTROSCOPY

UV-vis-NIR spectroscopy is a facile and non-destructive method for SWCNT synthesis. In principle, UV-vis-NIR spectroscopy should be to provide the chirality distribution of SWCNT films (on the basis effect of chirality of van Hove intraband transitions (Fig. 2.2) and the film thickness (based on the Berr-Lambert law). However, due to the thermal broadening and doping effect (due to bundling or other chemical compounds), it is not possible to unambiguously determine the chirality distribution [23]. Moreover, lack in verified data on extinction coefficients for corresponding chiralities inhibits the assessment of the ratio for metallic/semiconducting SWCNTs. This is why, in the thesis, the yield and the diameter distribution of nanotubes obtained were assessed by UV-vis-NIR spectroscopy.

Dual-beam spectrometer Perkin Elmer Lambda 1050 (Fig. 3.1) collects the signal within the wavelength range of 175 – 3200 nm with the resolution of 1 nm. Usually, the SWCNT films were transferred on a glass/quartz substrate for assessment with UV-vis-NIR spectroscopy. The characteristic peaks of the UV-vis-NIR spectra for SWCNTs (e.g. S₁₁, S₂₂, M₁₁) were attributed to certain diameters using the Kataura plot [41] (Fig. 3.2). The Berr-Lambert (equation 2.1) law provides a direct correlation between the absorbance and thickness of SWCNT films. Mikheev et al. [26] deduced the empirical formula:

$$h[nm] = -417\text{Log}(A_{550}), \quad (3.1)$$

where h is the thickness of SWCNT film in nm, A_{550} is the absorbance of the film at a wavelength of 550 nm (corresponds to the middle region

of the visible light spectra and usually is not affected by intensive intraband transition peaks).

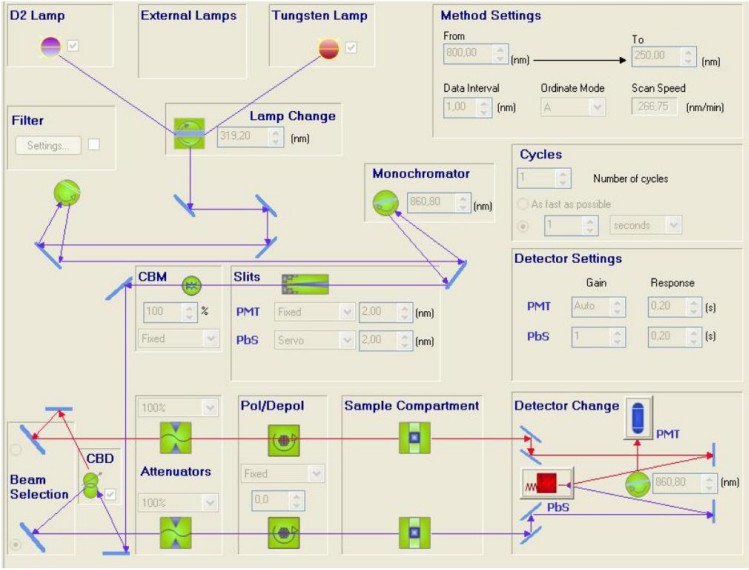


Figure 3.1: Principal scheme of the UV-vis-NIR dual-beam spectrometer Perkin Elmer Lambda 1050.

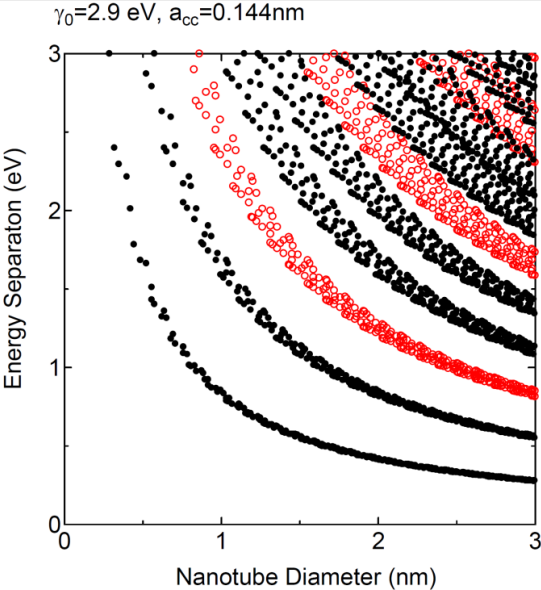


Figure 3.2: The Kataura plot representing the dependence of energy transitions vs nanotube diameter [41].

3.1.2. FOURIER TRANSFORM INFRARED SPECTROSCOPY

Fourier transform infrared spectroscopy (FTIR) is a technique which is used to obtain an infrared spectrum of absorption or emission of a solid, a liquid or a gas. An FTIR spectrometer simultaneously collects high spectral resolution data in a wide spectral range providing a significant advantage over a dispersive spectrometer (like Perkin Elmer Lambda 1050) which measures the intensity in a narrow range of wavelengths at a time. The principle of the FTIR spectrometer is represented in Fig. 3.3. First, a signal called an interferogram is generated by the interferometer (Fig. 3.3 a). The interferogram obtained is a record of the signal (intensity) by the infrared detector as a function of the difference in the path x for the two beams of the interferometer. Further Fourier transformation results in a characteristic spectrum (Fig. 3.3b)

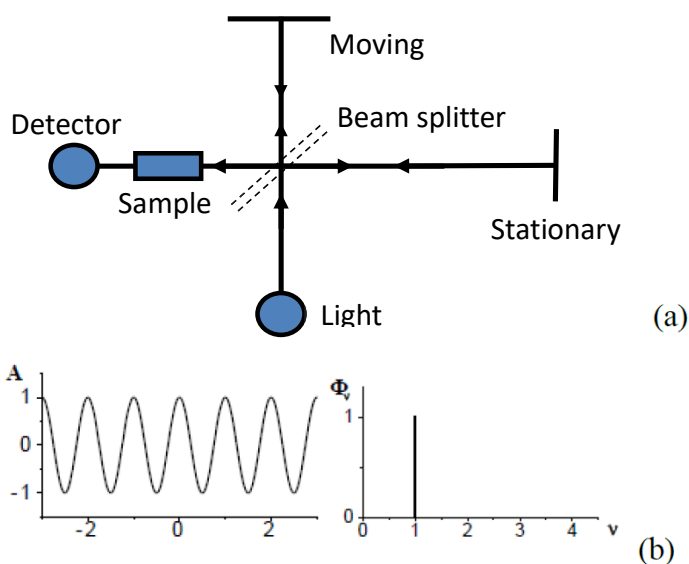


Figure 3.3: Principle scheme of FTIR spectrometer. (b) interferogram of the monochromatic source (left) and corresponding spectrum (right).

In this work, VERTEX 70v (Bruker, Germany) evaluable, fully digital FTIR spectrometer was used to measure characteristics in the range of $6000 - 50 \text{ cm}^{-1}$ (corresponds to the wavelength region $1.67 - 20 \text{ mm}$). A

standard globar forming part of a Vertex-70v FTIR spectrophotometer, which spectrum is close to the blackbody spectrum, was used as a source of IR radiation. The modulated radiation of the globar was fed to the sample under study. The spectral response of the sample to the modulated IR radiation of the globar is measured. In this case, each wavelength corresponds to a specific signal modulation frequency.

3.1.3. X-RAY PHOTOELECTRON SPECTROSCOPY

The chemical composition of the SWCNT film was explored with X-ray photoelectron spectroscopy (XPS) using electron spectrometer SPECS with a MgK α -source ($h\nu = 1253.6$ eV) at the energy transmission power analyzer Phoibos-150 of 15 eV. The vacuum in the analyzer chamber remained around 4×10^{-10} Torr. Spectra of C1s, O1s and Fe2p core levels were refined by multiple scanning. The deconvolution of the multicomponent spectra was performed using software package CasaXPS. The peaks were approximated by the Lorentz - Gauss function or Voigt profiles, C1s sp²-peak was fitted by the Doniach-Šunjić function.

3.1.4. RAMAN SPECTROSCOPY

Raman spectroscopy is one of the most abundant techniques for the SWCNT characterization as it provides a non-destructive approach for fast assessment of the sample purity and defectness, doping level, and chirality distribution of SWCNTs.

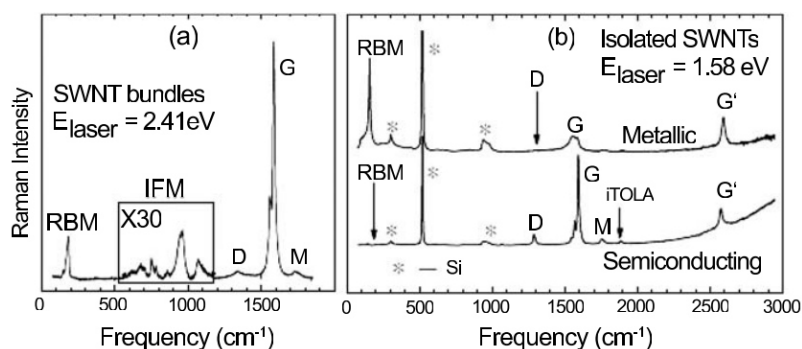


Figure 3.4: a) Raman spectra of HiPco SWCNT bundles, b) Raman

spectra of a metallic (top) and a semiconducting (bottom) SWCNTs at the single nanotube level [42].

A typical Raman spectrum of SWCNTs (Fig. 3.4) exhibits a number of modes corresponding to certain vibrations. The ideal graphene structure provides 6 vibrations satisfying the selection rules for Raman spectroscopy A_{2u} , B_{2g} , E_{1u} , E_{2g} , E_{2g} (Fig. 3.5).

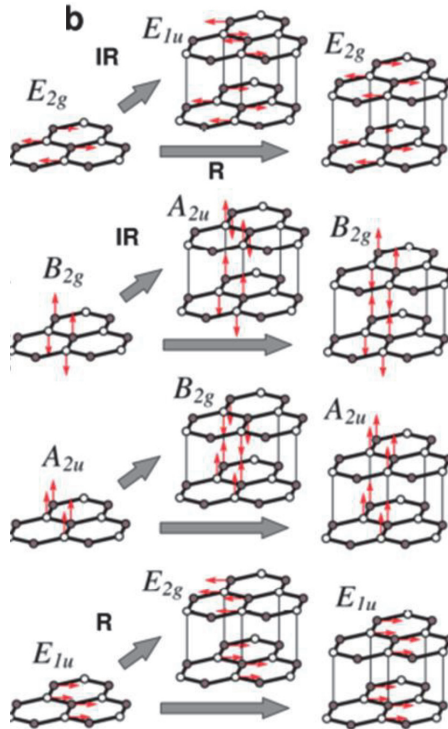


Figure 3.5: Illustration of A_{2u} , B_{2g} , E_{1u} , E_{2g} , E_{2g} for carbon structure [43].

In the thesis, the main attention was paid to the

- G mode (Lorentzian peak at $\sim 1582 \text{ cm}^{-1}$ split into lower energy G- peak and a higher energy G+ peak caused by the curvature of SWCNTs, which induces an energy difference between the axial and transverse in-plane(planar) vibrational modes).
- D mode, which does not satisfy the selection rules of Raman spectroscopy in the case of an ideal structure. It is attributed to phonon scattering on defects or inconsistencies in the crystal lattice. D mode

shows the Raman spectra of SWCNTs as a small peak of about 1350 cm^{-1} . The ratio of the G/D modes in Raman spectra is conventionally used to assess the structural quality of carbon nanotubes.

- The last major Raman feature is a series of peaks below 400 cm^{-1} . These peaks, so-called radial breathing modes (RBMs), are the result of a phonon excitation unique to SWCNTs. RBM is a purely radial mode, where the diameter of the entire SWCNT oscillates, appearing as though it were “breathing”. The Raman intensity of the RBM is strongly enhanced when the incident photon is in resonance with the SWCNT energy gap referring to the Kataura plot (Fig.3.2). Thus, by collecting Raman spectra produced by many different laser sources, a comprehensive characterization of the chirality distribution can be obtained.

The SWCNTs were examined with(using) Raman spectroscopy (Horiba LabRAM HR Evolution system; $\lambda = 532 \text{ nm}$ (2.33 eV); laser power of 0.1 mW). The laser spot diameter (a 50x objective with numerical aperture of 0.50) on the film surface was about 11.2 μm . In order to avoid the destruction of the SWCNTs during the long exposure and to avoid heating that causes changes in the response, the integral power density of the incident radiation was set at 0.4 kWcm^{-2} when measuring spectra. The obtained spectra were normalized to the intensity of G-peak maxima. Each measurement was taken at least 5 times in different areas of the sample and then averaged; the precision was $\pm 1 \text{ cm}^{-1}$.

3.2. MICROSCOPIC METHODS

3.2.1. SCANNING ELECTRON MICROSCOPY

The morphology of SWCNT films was assessed with scanning electron microscopy (SEM; FEI Helios Nanolab 660 DualBeam System; magnification 30 x – 1280 kx; maximum possible resolution 0.7 nm). We used secondary electron mode at an accelerating voltage of 2 kV.

3.2.2. TRANSMISSION ELECTRON MICROSCOPY

The SWCNT structure and the morphology of the thin films were studied by transmission electron microscopy (TEM; FEI Tecnai G2 F20 TEM; TEM lacey Cu-300 grid) system). TEM point resolution: to 0.24 nm. TEM line resolution: 0.144 nm. Ultra-high vacuum for contamination-free observation. Vacuum levels of specimen chamber & electron gun are $2.7 \cdot 10^{-5}$ Pa. To collect samples, a TEM lacey Cu-300 grid was placed on the filter in the flow of SWCNTs for 20-200 s to obtain the desired density.

3.2.3. ATOMIC FORCE MICROSCOPY

Topography images and the length distributions of SWCNTs were acquired by atomic force microscopy (AFM; Bruker Multimode V8) in Peak-Force™ mode. Bruker ScanAsist-Air cantilevers were used.

3.3. ELECTRICAL PROPERTIES

The performance of SWCNT films for various optoelectronic applications (e.g. thin-film electrodes) is usually attributed to the combination of the conductivity and optical transparency (typically at 550 nm as a reference wavelength). Since the thickness of the conducting layer in thin films is often unknown or unclearly defined [22], their electrical properties are characterized by the sheet resistance R (expressed in Ohms per square, Ohm/sq.).

For the sheet resistance measurements, the SWCNT thin films were transferred on a glass/quartz substrate. The films were measured by a linear direct contact four-probe method (with a distance of 1 mm between the needles) using Jandel RM3000 Test Unit that served as a current source and a digital voltmeter. For every point of the sheet resistance, at least 5 measurements were carried out.

Typically, industrial applications require a transparency of 90% (or even higher) at visual wavelengths with the least possible sheet resistance (values). To compare different films and materials with each other, we employed the following parameters:

- The Figure of Merit: $FoM = \frac{1000}{R \cdot A_{550}}$; (3.2)

- The equivalent sheet resistance, normalized to 90% transmittance film: $R_{90} = R \cdot \frac{A_{550}}{\lg\left(\frac{10}{9}\right)}$. (3.3).

For optical fibers, the electrical resistance of the coating was measured as a function of its length by the four-probe method using an MPI TS150 probe station contacting directly by the probes and Keysight 34410A multimeter, and the results confirmed that the coating was spatially uniform. Electrodes were secured(attached) to the SWCNT coating surface with a CW2400 conductive epoxy. To ensure a better temperature distribution uniformity in the FBG-containing fiber section, the electrodes were located at a distance of about 5 mm from the grating edges.

3.4. AEROSOL STUDIES

The number size distributions of both Fe catalyst nanoparticles and SWCNT aerosols were studied using differential mobility analyzers (DMA) (TSI, scanning mobility particle sizer spectrometer 3938) capable to measure the particles of effective diameter from 0.7 nm to 60 nm (1nm Scanning Mobility Particle Sizer Spectrometer, TSI, USA) and from 6 nm to 230 nm (Scanning Mobility Particle Sizer Spectrometer 3938, TSI, USA). It should be mentioned that the separation is based on the electrical mobility followed by the data processing based on the implication of the spherical shape of the aerosol particles (standard software of Scanning Mobility Particle Sizer Spectrometer). This results in the effective diameter of SWCNT to be observed by this technique in the range of 40-100 nm. Moreover, the possible formation of the non-cylindrical agglomerates will also affect the distribution and cannot differ from an individual SWCNT. Though such values of effective diameter mainly correspond to the projected area diameter, this allows us to distinguish the nanotubes from metal nanoparticles (effective diameter of 1-20 nm; Fig. 3.5). In the case of nanoparticles produced by a spark discharge generator, a direct correlation between TEM statistics and DMA measurements was reported elsewhere [44].

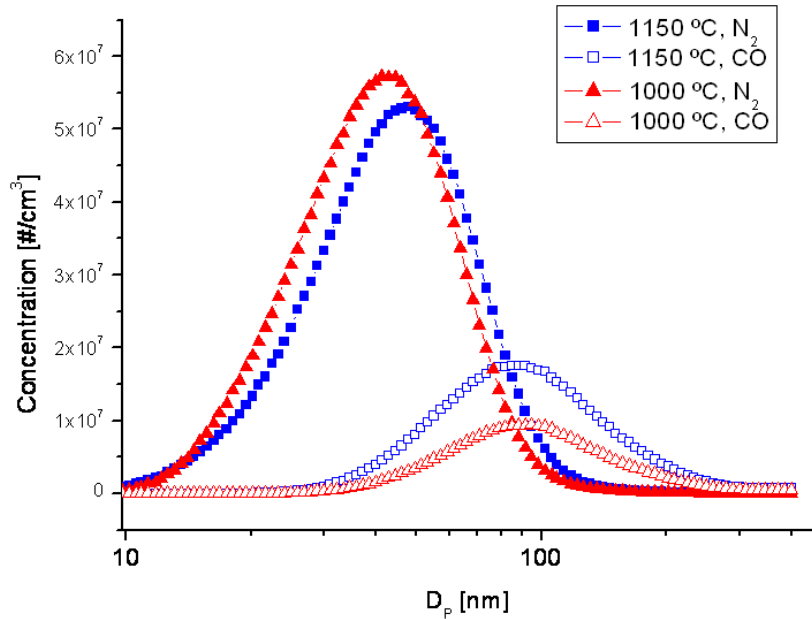


Figure 3.5: Number size distribution measurements of the aerosols of the nanoparticles (product formed in N_2) and carbon nanotubes (CO atmosphere) [44].

3.5. THERMOGRAVIMETRIC ANALYSIS

To study the thermal stability of SWCNTs and to estimate the Fe content in the nanotube films, thermogravimetric (TGA) and differential thermal analyses (DTA) were carried out. The TGA studies were coupled with the mass-spectrometry unit using NETZSCH STA. The experiments were conducted in the air with a heating rate of 10 °C/min. In relation to SWCNT films, TGA identifies data such as moisture loss, loss of volatiles, oxidation, pyrolysis, and ash content (oxidized catalyst residuals).

4. SWCNT GROWTH

During the last 15 years, aerosol CVD setups have been equipped with a number of catalyst producing units: decomposition of catalyst precursors (ferrocene, iron pentacarbonyl, *etc.*) followed by sintering and *in situ* nucleation of nanotubes [27], [45], hot-wire generator [44] and a spark discharge generator producing vapors of active metals [46], [47]. Here, the ferrocene-based reactor and spark-discharge method will be shortly introduced.

4.1. FERROCENE REACTOR

The most abundant apparatus for the aerosol CVD, so-called ferrocene reactor, was employed to provide a justified comparison of the results obtained in the thesis. The reactor is assembled as follows. A ferrocene cartridge (Fig. 4.1) is filled with a mixture of $\text{Fe}(\text{C}_5\text{H}_5)_2$ (Sigma Aldrich, 98%) and SiO_2 spheres (c.a. 0.7 mm) to facilitate the flow. Volatile ferrocene ($P \sim 0.6$ Pa at 20 °C [48]) is then transferred by the nitrogen stream via a warm gas line (~ 70 °C) into the heated zone for the further decomposition (at $T > 400$ °C [49]).

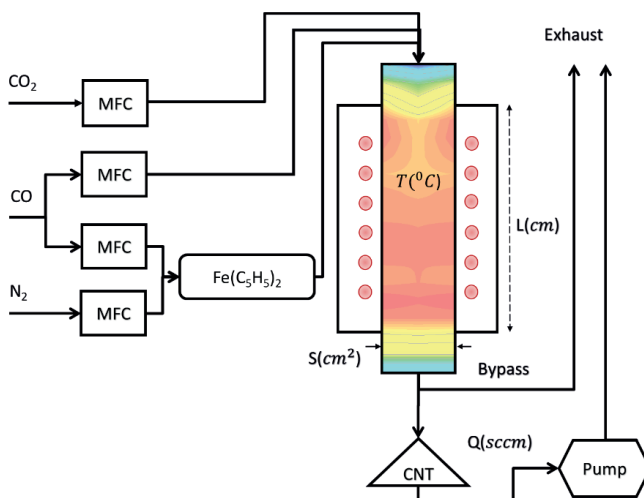


Figure 4.1: Schematic representation of ferrocene reactor.

Fe(C₅H₅)₂/N₂ vapor mixture was introduced near the hot zone of the reactor (at T~500 °C) and mixed with the carbon source (CO; 99.999%) and CO₂ (99.995%) as a promotor of the Boudouard reaction (2CO=C+CO₂). The process is taking place on the catalyst surface within the hot zone of a quartz tubular reactor results in the SWCNT growth. The synthesis was realized at ambient pressure with a residence time of 6 s, with 28 % vol., 72-70 % vol., 0-2 %vol. respective concentration of N₂, CO, CO₂, the temperature in the reactor from 680 to 1080 °C.

4.2. SPARK DISCHARGE GENERATOR REACTOR

The aerosol CVD reactor for SWCNT growth equipped with a spark-discharge generator of catalytic nanoparticles was developed by Kaskela *et al.* [46] in 2015. The method demonstrated to produce the carbon nanotubes with the length of ~ 4 μm, though only a small fraction of the resulting metal particles was employed for the SWCNT growth (0.4-3%) [47], while the most of the catalyst was subjected to exhaust. In this work, there has been developed a spark discharge generator for scalable synthesis of ultrashort single-walled carbon nanotubes with controlled diameter distribution and defect concentration with a secondary goal of eliminating the loss of the most of the catalyst to exhaust.

Spark discharge generator was equipped with two Fe electrodes (99.99%; 40-mm long cylinders with $d = 4$ mm) with a variable distance between of 0.1-5 mm controlled by a micrometric manipulator, a nozzle for effective mass transfer, and flow channel for transporting the iron nanoparticles produced in the aerosol CVD reactor for the SWCNT growth. We used a high voltage generator Heinzinger PNC 20000-10 (DC Voltage of 0-20 kV, current of 0-10 mA; Germany) combined with a 45 nF (C) capacitor for collecting a charge until a discharge with frequency occurs:

$$f = \frac{I}{CV}, \quad (4.1)$$

where V is recharge voltage (0.1-3 kV in this work), I is the current (0.05-1 mA). The energy (E) of a single charge can, thereby, be presented as:

$$E = \frac{CV^2}{2}. \quad (4.2)$$

The discharge leads to a plasma formation followed by fractional evaporation of the electrode material. The electrodes were subjected to a flow of a carrier gas (0.5-5 LPM; Ar (99.999%), H₂ (99.999%), or N₂ (99.999%)) that carried the Fe vapor to the reactor (Fig. 4.2) for the forthcoming SWCNT synthesis (time from the spark to the reactor hot zone is of 0.05-0.5 s).

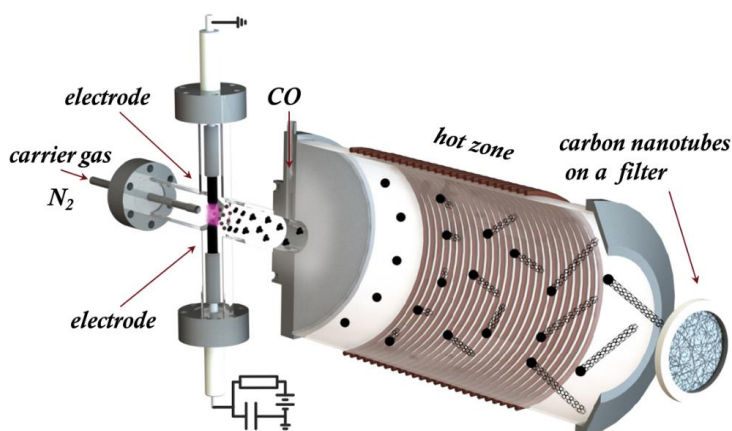


Figure 4.2: General scheme of the spark discharge generator integrated with a tubular growth zone to provide the aerosol SWCNT synthesis.

The obtained nanoparticles were then subjected to the tubular quartz reactor (isothermic zone ~800 mm, $d = 50$ mm) and mixed with the carbon source, CO (99.999%; 1-5 LPM). The Boudouard reaction on the catalyst surface occurring in the hot zone results (residence time is 6 s; the reactor is operated at ambient pressure) in the SWCNT growth. The SWCNTs obtained were filtered through HAWP filter (Merck Millipore, USA) with a typical collection time of 15 min for further dry transfer to a glass/quartz substrate suitable for Raman and UV-vis-NIR studies [50] or to provide a free-standing film (Fig 4.3). It should be stressed that unlike the most spark-discharge processes [46], [47] the reactor developed is exhaust-free, i.e. all the nanoparticles are delivered to the reactor.



Figure 4.3: Photo of a free-standing thin film (left) and thin film on a filter of SWCNTs (thickness of the film is about 60 nm in both cases) produced by the spark discharge aerosol CVD method.

4.3. INFLUENCE OF THE DISCHARGE PARAMETERS

The frequency of the spark discharge within the generator is proportional to the current between the electrodes according to eq. (4.1). In terms of materials produced, this gives us an opportunity to increase the yield of both iron nanoparticles and SWCNTs produced while the number size distributions might be monitored using the DMA (Fig. 4.4 a, b). Indeed, we observed the linear dependence of the yield of carbon nanotubes (Fig. 4.4 b, c), while the average diameter was proven to be constant of 1.0 nm (as calculated based on the energy of S_{11} transition) [51]. Such increase in the yield without any harm to the diameter and the length distribution is not typical for both aerosol science and carbon nanotube growth in general: usually the particles of higher concentration tend to agglomerate faster providing about the same concentration [52], while the carbon nanotube synthesis mechanism is still challenging [53]–[55] due to the entanglement of different kinetic steps (e.g., complex relation between the reaction parameters, diameter, and yield). This allow us to consider the most part of the active catalyst particle agglomeration to be performed in plasma or nearby hot zone (~ 1 mm from the spark [56]) while the subsequent transport to the SWCNT synthesis zone of the reactor has a minor effect (Fig. 4.4).

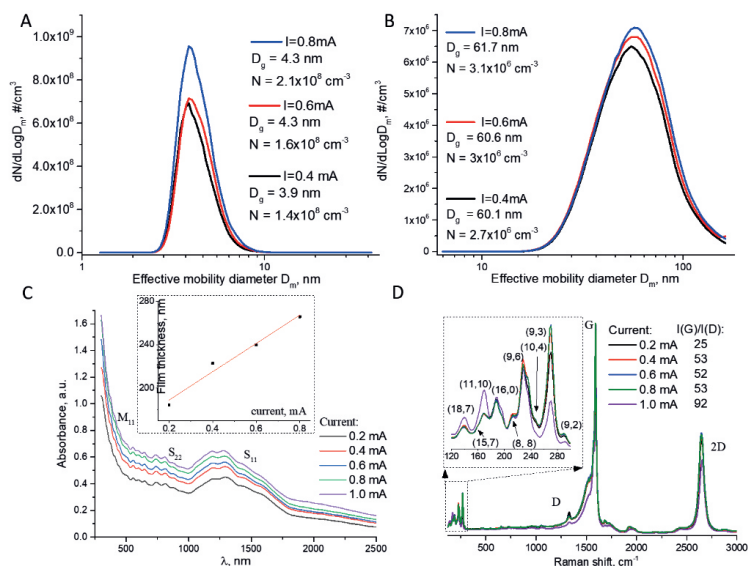


Figure 4.4: Influence of current between electrodes on nanoparticle generation and SWCNT growth: DMA number size distributions of a) iron nanoparticles at the end of the spark apparatus (distance between the electrodes of 6 mm; $U \sim 1.3 \text{ kV}$; D_g is the geometric mean), b) carbon nanotubes produced in the reactor with additional spark generator parameters (880 °C; 2 LPM N_2 ; 4 LPM CO); c) UV-vis-NIR spectra of SWCNT thin films, the inset shows the current dependence of the film thickness; d) Raman spectra (2.33 eV) of SWCNT thin films obtained at different current parameters of spark discharge generator, the inset shows enlarged zone of radial breathing modes.

Interesting feature of the developed spark generator is an enhancement in the quality of SWCNTs with a higher yield. This can be accounted for etching role of the product of the Boudouard reaction – CO_2 : the higher yield results in a higher conversion of the carbon monoxide providing the more effective etching of amorphous or defective carbon impurities of nanotubes [57].

Oppositely to the current, the breakdown voltage shows an almost negligible effect of the defect concentration within the SWCNTs (Fig. 4.5d). This may be due to the parabolic enhance of the yield producing

so much CO₂ that it can etch the SWCNT structure [58]. The diameter distribution of SWCNTs is not affected by both the current and breakdown voltage (Fig. 4.5 b, c) which means that the particles are mostly formed in the plasma zone near the spark discharge. Nevertheless, the influence of the breakdown voltage on SWCNT yield can be described well with parabolic function (Fig. 4.5 c); inset) analogous to the equation (2), taking into account the direct correlation between the amount of nanoparticles formed and SWCNT concentration (Fig. 4.5 a, b). It should be mentioned that we did not observe any additional chiral indexes in the pool while varying the breakdown voltage. Thus, the breakdown voltage and current allow us to manipulate precisely the yield of single-walled carbon nanotubes and their defective structure while maintaining the diameter distribution. This may be due to the unusual situation of carbon nanotube growth – a relatively inhibited sintering of the active particles in the zone of the reactor preceding the nucleation – formation of carbon nanotube cap [5], [59], [60]. Thus, we can consider the two fundamental steps of the carbon nanotube nucleation, namely, the sintering of the active particles and their saturation with carbon intermediate species [28], [61], [62], to be separated in space and time providing a direct route to the scalable, robust technology of SWCNT growth.

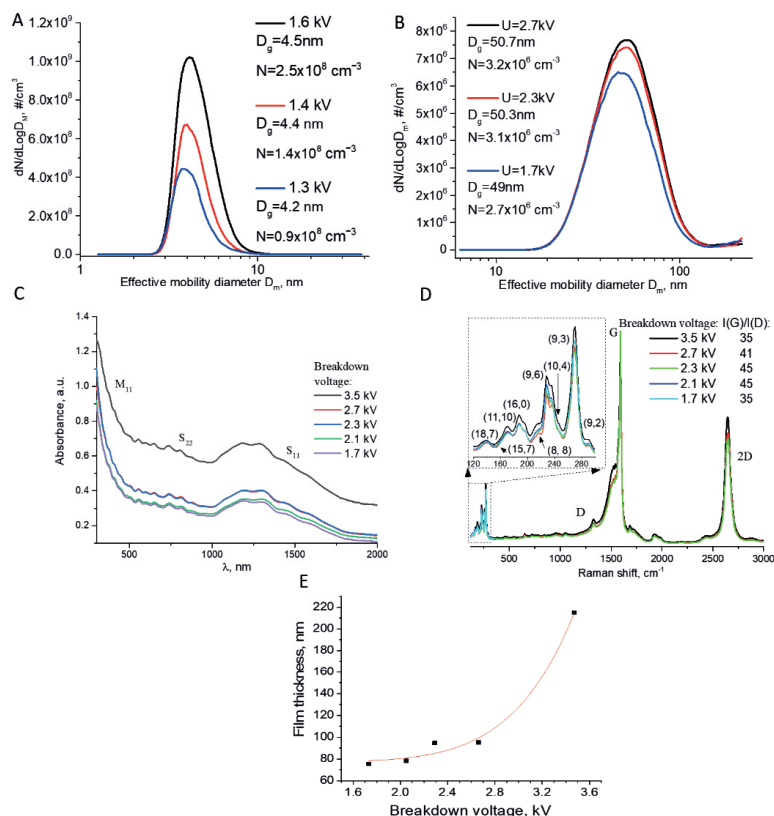


Figure 4.5: Influence of breakdown voltage between the electrodes on nanoparticle generation and SWCNT growth: DMA number size distributions of a) iron nanoparticles at the end of the spark apparatus ($I=0.5 \text{ mA}$; $U \sim 1.3 \text{ kV}$); b) carbon nanotubes produced in the reactor under complementary spark generator parameters ($880 \text{ }^\circ\text{C}$; 2 LPM N_2 ; 4 LPM CO); c) UV-vis-NIR spectra of SWCNT thin films; d) Raman spectra of SWCNT thin films obtained at different breakdown voltage parameters of spark discharge generator, the inset shows enlarged zone of radial breathing modes; e) the dependence of the film thickness on the breakdown voltage.

An increase of the carrier gas flow rate results in a significant decrease of iron particle diameter (Fig. 4.6 a, b), while the influence on the SWCNT growth is more complicated: the higher flow rate of nitrogen dilutes the carbon monoxide reducing the rate of CNT growth due to the lower partial pressure of the carbon source. This results in volcano-like

dependence of the effective aerosol size of the nanotubes (Fig. 4.6 c) and the yield (Fig. 4.6 d) while changes in the diameter distribution according to the TEM statistics are rather minor (Fig. 4.7). The iron nanoparticles observed in Figure 4.7 correspond to non-activated catalyst particles. Indeed, the DMA measurements of the Fe nanoparticles show only a small fraction of metal species exceeding 5 nm. As under CVD conditions the particle size and SWCNT diameter are almost the same [3], [5] and due to the feature of Boudouard reaction (no formation of multi-walled carbon nanotubes [15], [44]), the particles larger than 5 nm would not provide SWCNT nucleation. As CO decomposition is still possible on the surface of such nanoparticles, a certain carbon concentration is reached under the growth conditions providing a graphitic core at the room temperature due to a dramatic decrease of the carbon solubility.

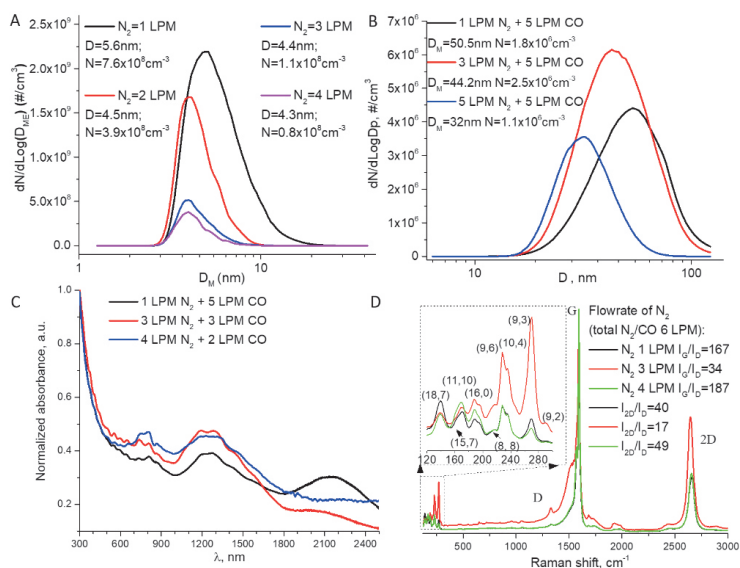


Figure 4.6: Influence of the carrier gas flow rate on nanoparticle generation and SWCNT growth: DMA number size distributions of a) iron nanoparticles at the end of the spark apparatus ($I=0.5 \text{ mA}$; $U\sim 1.3 \text{ kV}$); b) carbon nanotubes produced in the reactor under complementary spark generator parameters ($880 \text{ }^\circ\text{C}$; total flow of 6 LPM, $N_2+\text{CO}$); c) UV-vis-NIR spectra of SWCNT films, the dependence of the film thickness on

the breakdown voltage is in inset; d) Raman spectra of SWCNT films obtained at different carrier gas flow rate in the spark discharge generator, the inset shows enlarged zone of radial breathing modes.

The crucial role of the carbon monoxide feeding was confirmed by controlling the amount of carbon monoxide while the residence time varied (Fig. 4.8): this resulted in the same parameter dependence as the abovementioned breakdown voltage and the current SWCNT growth – diameter distribution and observed defectiveness (Fig. 4.8 a, c) are almost the same. However, the particle size distribution obtained by DMA shows an interesting dependence, while the total concentration of the particles constantly grows, the mean observed diameter shows an extremum value at a flow rate of 1.7 LPM.

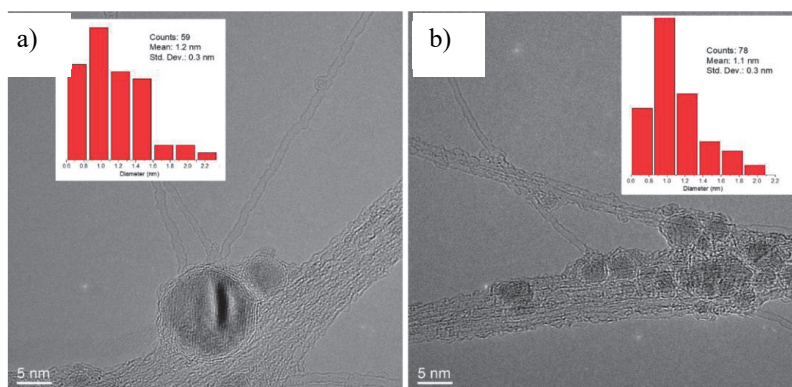


Figure 4.7: TEM SWCNTs microphotographs produced at different nitrogen flow rates through the spark discharge generator: a) 0.5 LPM N₂, b) 2 LPM N₂ (880 °C; the total flow of N₂+CO=6 LPM); the insets show the diameter distributions based on TEM statistics.

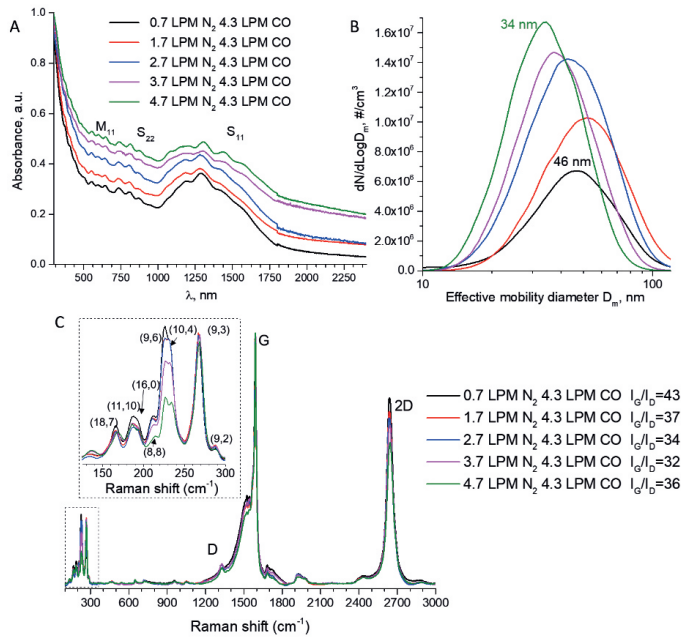


Figure 4.8: Influence of the nitrogen flow rate on Fe particle generation and SWCNT growth under (at) a constant CO flow: a) UV-vis-NIR spectra of SWCNT films ($I=0.8$ mA; $U\sim 2$ kV); b) DMA number size distributions of SWCNTs (880 °C); c) Raman spectra of SWCNT thin films obtained at different nitrogen flow rates in the spark discharge generator, the inset shows enlarged zone of radial breathing modes. The colors of the samples at figures a)-c) are the same: black line – 0.7 LPM of N_2 through the spark discharge generator, 4.3 LPM of CO through the side flow after the generator; red – 1.7 LPM N_2 , 4.3 LPM CO; blue – 2.7 LPM N_2 , 4.3 LPM CO; magenta – 3.7 LPM N_2 , 4.3 LPM CO; olive – 4.7 LPM N_2 , 4.3 LPM CO.

Using this interesting feature we have optimized the length of SWCNTs to be lower than 500 nm (eight times lower than in [46]) according to AFM statistics (Fig 4.9) providing a route for scalable production of the individual nanotubes for drug delivery and transistors. It should be remained, that the volcano-like (single-extremum) dependence might be implied on the basis of the AFM data (Fig 4.9).

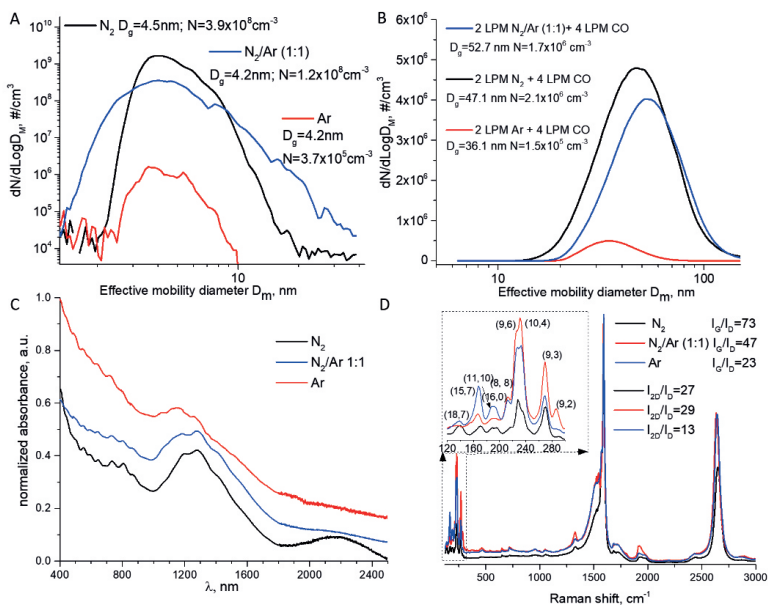


Figure 4.9: a), b) typical AFM images of SWCNTs on SiO₂ substrate; the length distributions based on AFM statistics for different contact time within the reactor: c) 7 s (2 LPM N₂, 2.5 LPM CO); d) 5 s (2 LPM N₂, 4 LPM CO); e) 2.5 s (4 LPM N₂, 9 LPM CO).

Obviously, the carrier gas nature should affect the breakdown voltage providing a smooth control of the nanoparticles produced. We have employed nitrogen, argon, and hydrogen as model gases for SWCNT growth. Moreover, hydrogen is considered to be a promoter in the SWCNT growth process in the aerosol CVD approach [8]. We have found the carrier gas nature to have a crucial impact of SWCNT growth when using the spark discharge generator as a catalyst source (Fig. 4.10). Number size distributions of both Fe nanoparticles and formed SWCNTs show a significant decrease of the material produced coinciding with phenomenological Pachsens' law for discharge [63]. Moreover, the introduction of hydrogen stopped the production of SWCNTs providing more than 1000 ppm of water in the exhaust. This may be due to hydrogen ionization in spark generator hot zone. Nevertheless, the Ar/N₂ mixtures can be considered as a route for smooth tuning of the defective structure of SWCNT.

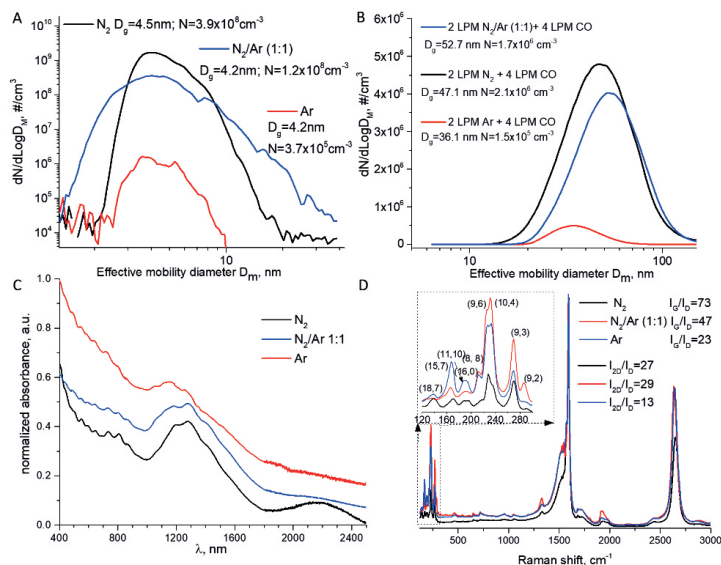


Figure 4.10: Influence of the carrier gas nature in the spark discharge generator on the production of Fe nanoparticles and SWCNT growth: DMA number size distributions of a) iron nanoparticles at the end of the spark apparatus ($I=0.5$ mA; $U\sim 1.3$ kV); b) carbon nanotubes produced in the reactor under complementary spark generator parameters (880 °C; 2 LPM of a carrier gas; 4 LPM CO); c) UV-vis-NIR spectra of SWCNT thin films; d) Raman spectra of SWCNT thin films in different carrier gas nature spark discharge generator, the left inset shows enlarged zone of radial breathing modes.

Thus, there has been observed a rare (in terms of the SWCNT growth) case of independent product characteristics – the changes in the current between the Fe electrodes affects the yield, but not the diameter distribution, while the breakdown voltage has neglectable influence on the defect concentration of SWCTNs providing parabolic boost in the yield. The ability for tuning the defectiveness though changes in the nature of a media within the generator was shown: the substitution of nitrogen on argon as a carrier gas drops the quality of nanotubes. This is may be due to the separation of the nanoparticle formation and carbon nanotube nucleation processes – the most part of agglomeration occurs in plasma or nearby hot zone of the generator while the effect of the

following transport to the SWCNT synthesis zone of the reactor is rather minor. This feature, unusual for SWCNT growth reactors, grants us an extra degree of freedom in terms of fine-tuning of the materials produced.

4.4. THE ROLE OF TEMPERATURE AND CO₂ CONTENT

The SWCNT growth in the ferrocene reactor has been widely studied during the last 15 years [7], [15], [27], [45], [57], [64]–[68]. When CO is applied as a carbon source, the temperature usually shows a narrow optimum condition ~ 880 °C. While the addition of CO₂ [27] leads to an increase in the mean diameter, lowers defectiveness, and has volcano-like dependence for the yield. However, the corresponding parameters for a spark discharge reactor have not yet been studied. In this section, to provide a justified comparison, we consider the influence of the CO₂ and the temperature on SWCNT growth in the spark discharge reactor.

Carbon dioxide acts as a promotor enhancing the catalytic activity of Fe particles for ferrocene reactor. However, in the case of the spark-discharge reactor, we observe an opposite influence: increase of CO₂ concentration inhibits SWCNT growth (Fig. 4.11). A decrease of the observed effective size of aerosol particles (Fig. 4.11a) can be attributed to either reduced catalytic activity of Fe species (leading to shorter nanotubes) or to suppressed activation of the catalyst (leading to a lower amount of SWCNTs in bundles). However, the SWCNT length distribution based on AFM statistics clearly rejects the former hypothesis (Fig. 4.11 b, c). Thus, low amounts of CO₂ do not affect the rate of steady-state SWCNT growth.

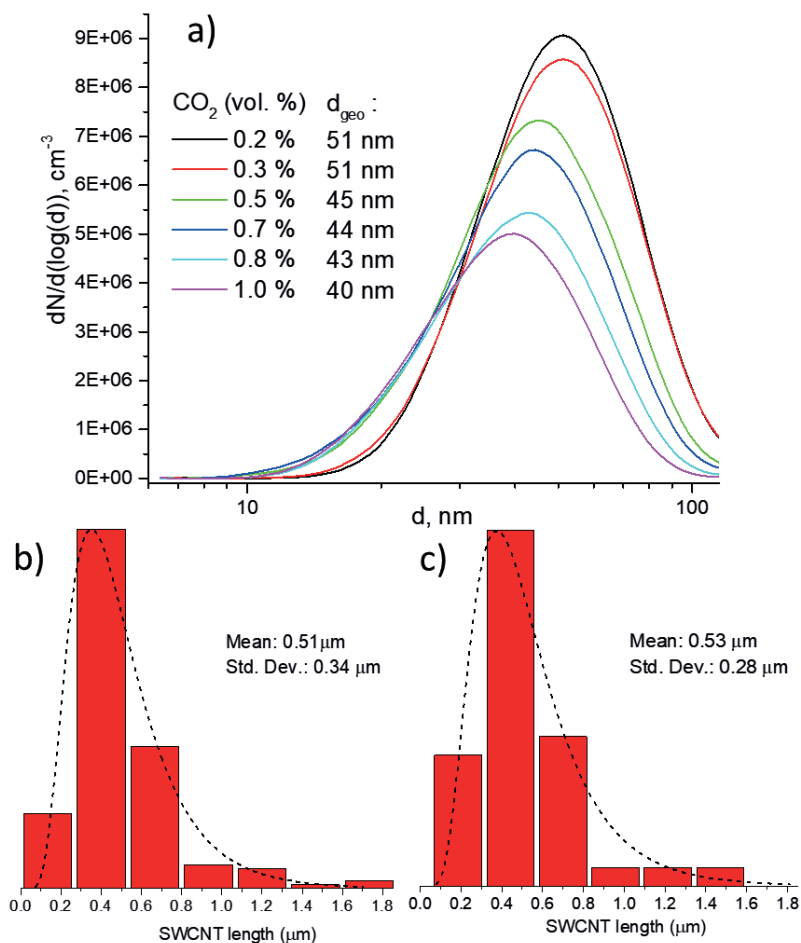


Figure 4.11: Influence of CO₂ on the SWCNT growth in the spark discharge reactor: a) DMA number size distributions of SWCNTs produced under different concentration of CO₂, the arrow shows the shoulder of oxidized Fe particles; the length distribution of SWCNTs based on AFM statistics for the sample produced without CO₂ (b) and with 0.5 vol. % of CO₂ (c).

The effect of CO₂ on SWCNT nucleation is not limited to the fraction of active Fe particles. The mean diameter of SWCNTs (a parameter defined during the nucleation) tends to increase with the addition of carbon dioxide to the spark discharge reactor (Fig 4.12 a) similarly to the effect observed for the ferrocene reactor [27], [69]. This can be explained as follows. The addition of CO₂ shifts the size-dependent equilibrium of the Boudouard reaction on the catalyst surface leading to the etching of

small-diameter nanotube caps during the nucleation stage. The hypothesis of partial etching of the most unstable or defective species in the ensemble is supported (Fig 4.12 b) by the increase of the ratio of intensities of G and D modes (I_G/I_D) of Raman spectra (corresponds to a reverse defect concentration[70]). Moreover, apart from the etching of defective species, the I_G/I_D growth can also be affected by the shift in SWCNT diameter distribution (thicker nanotubes correspond to higher I_G/I_D [71], [72]).

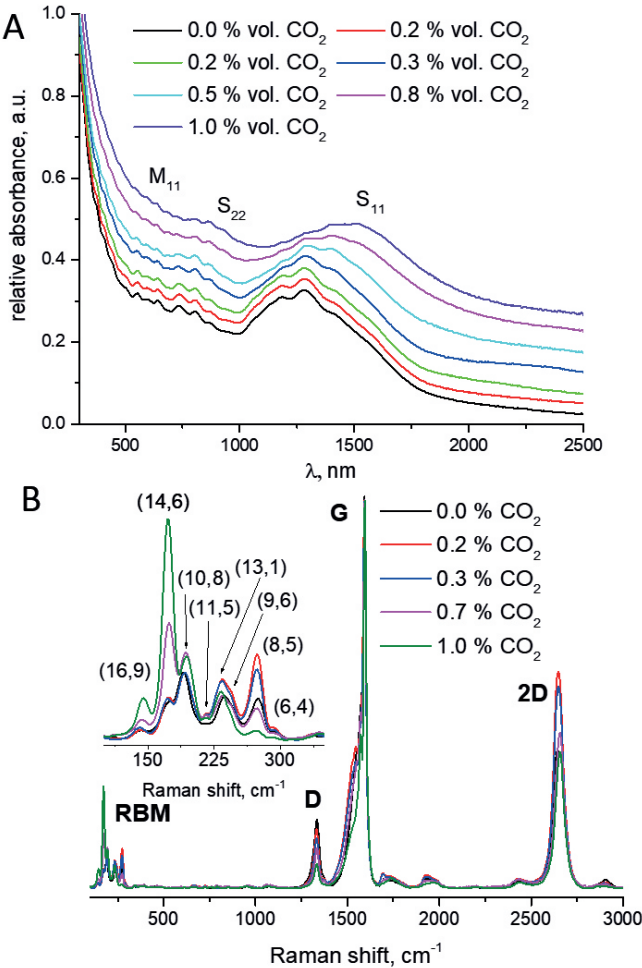


Figure 4.12: Influence of CO₂ on the UV-vis-NIR spectra (a) and Raman spectra (b) in the spark discharge reactor.

The temperature dependence of the yield shows a volcano-like dependence (Fig. 4.13 a) with an optimal point c.a. 880-980 °C similar to 40

the ferrocene reactor. I_G/I_D constantly increases with temperature (Fig. 4.13 b) that corresponds to the behavior observed in literature [73].

Interestingly, a small shift in diameter when heated (Fig. 4.13 b) shows apparent activation energy of 9 kJ/mol. Similar value can be obtained if the coagulation of aerosol nanoparticles is considered to be the rate-limiting step during the SWCNT nucleation. Indeed, the coagulation-limited process results in a value of the apparent activation energy of RT (where R is the gas constant). Under the SWCNT growth temperatures ($T \sim 1000$ K), the value of RT is ~ 8 - 10 kJ/mol.

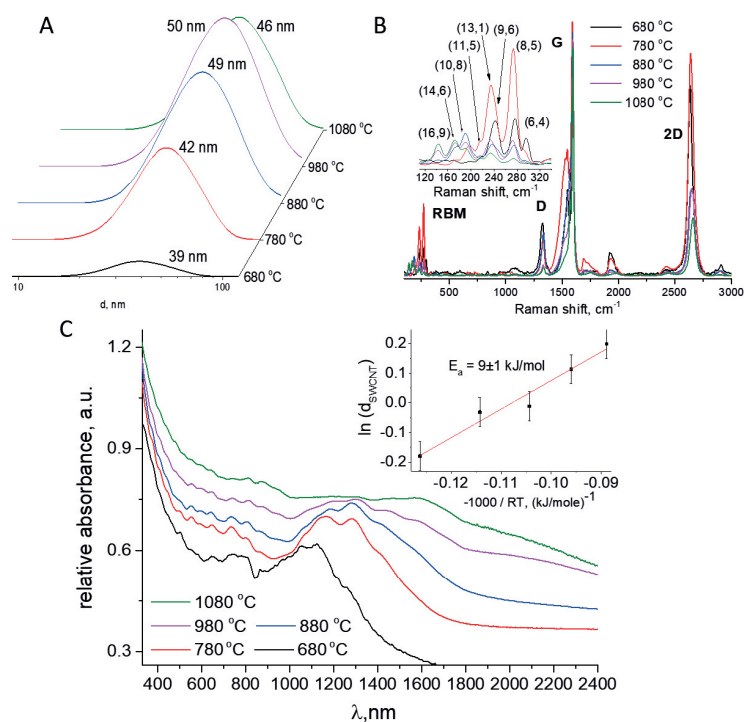


Figure 4.13: Effect of the temperature on the SWCNT growth in the spark discharge reactor: a) DMA number size distributions of SWCNTs produced; b) Raman spectra of SWCNT thin films obtained, the inset shows enlarged zone of radial breathing modes; c) UV-vis-NIR spectra of SWCNT thin films, the inset corresponds to the Arrhenius plot of the film thickness.

Thus, despite a minor loss in the yield, the spark discharge reactor provides simple and precise way to increase the productivity of the process without any harm to the diameter distribution or defectiveness of the carbon nanotubes [74], unlike the case of the ferrocene based reactor.

4.5. COMPARISON OF THE SPARK DISCHARGE AND THE FERROCENE REACTORS

A distinctive feature of the spark discharge reactor is the separation of the active component sintering and Fe saturation with carbon – the two steps preceding the SWCNT nucleation [5], [59], [60]. Fig. 4.14 schematically illustrates the difference in the SWCNT nucleation procedure. While the influence of the growth temperature was shown to be similar for both the ferrocene and spark discharge reactors the differences in the role of carbon dioxide are more distinctive.

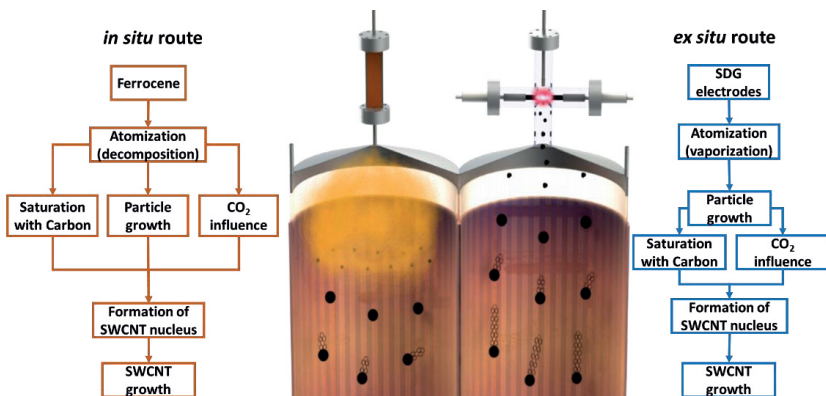


Figure 4.14: Schematic representation of the differences in the SWCNT nucleation in the ferrocene (left) and the spark discharge (right) reactors.

Unlike the ferrocene reactor, carbon dioxide addition does not result in a volcano-like dependence with a promotion of SWCNT growth followed by the inhibition (Fig. 4.15). However, trends corresponding to a decrease in the catalyst productivity presumably have the analogous mechanism: the reaction order with respect to carbon dioxide is ~ 0.5 . Thus, as discussed in the previous section, the CO_2 decreases the fraction of active catalytic particles. The increase of the

activity in the case of the ferrocene reactor can be attributed to the following processes. Similar to the role of the water vapor in the supergrowth process [75], the CO₂ can etch the amorphous carbon species on the catalyst surface. As CO is one of the most stable carbon species (along with methane) the amorphous carbon is provided mostly by the ferrocene residuals, which absent in the case of the spark-discharge reactor.

The ferrocene reactor provides a higher SWCNT yield (Fig. 4.15) at comparable catalyst concentrations. This can be attributed to the peculiarities of the activation procedure: *ex situ* activation in the case of the spark discharge reactor (Fig 4.14) leads to lognormal particle size distribution. This results in the higher fraction of large Fe nanoparticles when compared to *in situ* activation (ferrocene reactor) reducing the SWCNT yield.

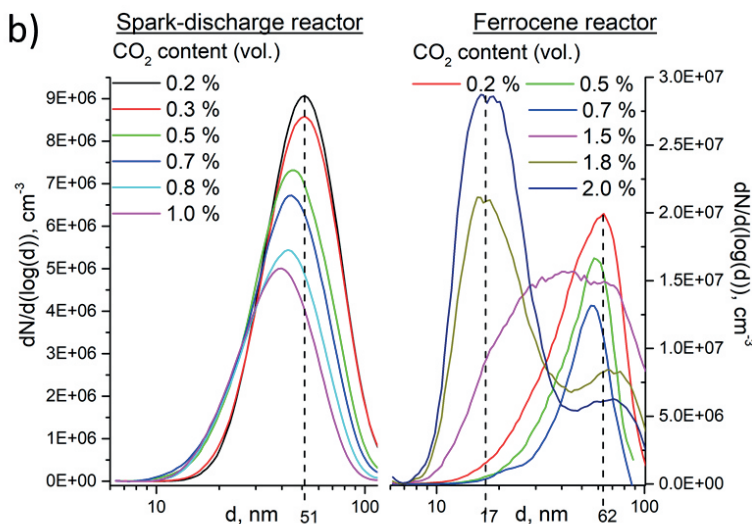
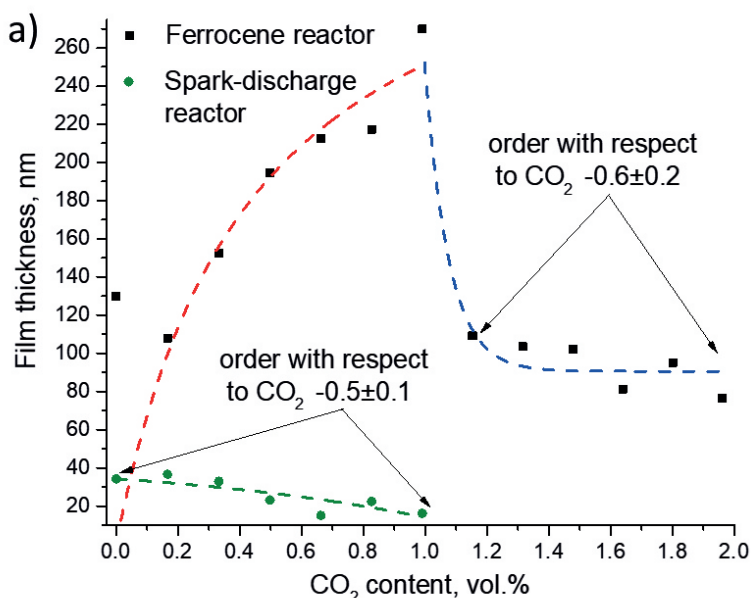


Figure 4.15: Comparison of the SWCNT growth under different CO₂ content in the spark discharge and ferrocene reactors in terms of the yield (a); DMA number size distributions of SWCNTs produced in different reactors (b).

The increase of the SWCNT mean diameter and I_G/I_D is similar for both reactors implying that the role of CO₂ during the nucleation step is roughly the same (Fig. 4.16). Thus, the difference in the architecture of the aerosol CVD reactors equipped with ferrocene

cartridge and spark discharge generator of Fe nanoparticles affects the nucleation patterns of the SWCNT growth providing both *ex situ* (spark discharge reactor) and *in situ* (ferrocene reactor) activation of the Fe catalyst. On the one hand, *ex situ* activation (spark discharge reactor) leads to lognormal particles size distribution inhibiting the yield by decreased utilization degree due to the fraction of large Fe nanoparticles; on the other, the SWCNT growth in the spark discharge reactor shows a simple relation between the carbon dioxide content and the diameter distribution while the yield can be independently tuned in a wide range by the parameters of the spark discharge [74]. The temperature variation shows a minor effect on the diameter with the apparent activation energy $\sim RT$.

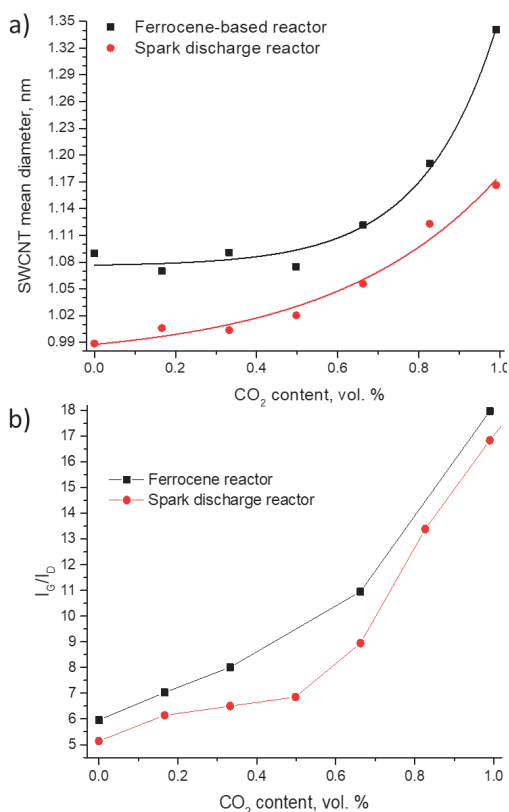


Figure 4.16: Comparison of the SWCNT growth under different CO₂ content in the spark discharge and ferrocene reactors on the mean diameter (a), defectiveness (b).

Thus, the spark discharge reactor developed provides a route for independent tuning of the yield (breakdown voltage, the current), diameter distribution (CO₂ content), defectiveness (inert gas nature, temperature, CO₂ content) opening an avenue for scalable aerosol CVD growth of SWCNTs with tailored properties.

5. DATA ANALYSIS AND PROCESSING

5.1. DATA PREPARATION

The complexity of mechanisms of the nanotube nucleation, growth, and termination inhibited the progress towards the control of the product with defined parameters by a general kinetic model for the SWCNT growth. The lack of the model (a quantitative correlation between the synthesis process and SWCNT performance) and systematic datasets are still key barriers to controlled synthesis and, therefore, for a wide range of applications [3], [5], [76]. Here, for the first time, we employ the methodology of artificial neural network (ANN) (Fig.5.1) that proved itself for complex multi-parameter tasks [77], [78] of processing of the experimental data to enhance the control over single-walled carbon nanotube(s) under synthesis conditions and to predict the experimental results.

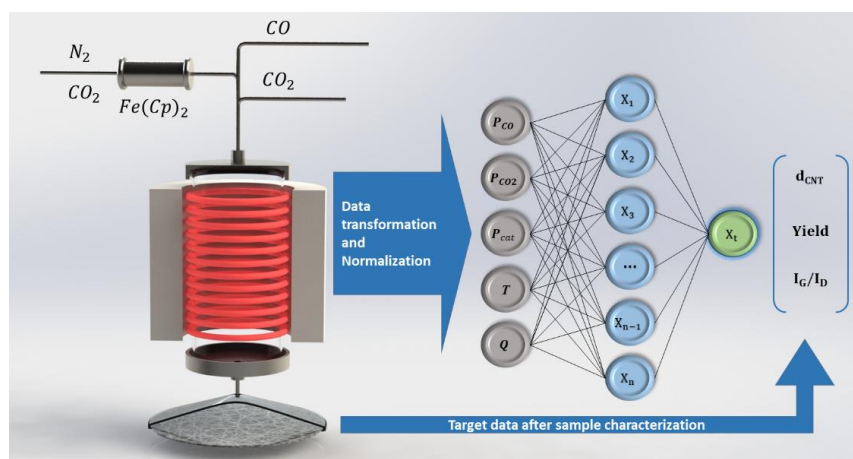


Figure 5.1: A schematic representation of the hierarchical architecture of the experimental setup and artificial neural network connection for controlled and predictive SWCNT synthesis.

The aerosol CVD synthesis based on Boudouard reaction ($2CO=C+CO_2$), the method employed within the thesis, is the most suitable for the ANN processing – this relatively simple method allows us to minimize the number of input parameters avoiding the influence of a

substrate, catalyst activation procedure and to decrease a variety of possible chemical reactions during the synthesis.

We define five key input parameters, namely, the partial pressure of CO, CO₂ and ferrocene as well as the residence time and temperature, for a comprehensive description of the process within the experimental architecture used. Undoubtedly, the key input parameters are not the only variables affecting the SWCNT growth. However, the other things kept constant (*e.g.*, catalyst composition, way of catalyst production, reactor type) and can be added in further studies. At the same time, the complex effect of each input parameter on SWCNT characteristics [79] (*e.g.*, both CO₂ content, as well as T affect the diameter distribution, defectiveness and the yield [7], [27], [50], [57]; even the partial pressure of the carbon source (CO) affects both the nucleation and the growth providing a non-trivial dependences [5]) inhibiting simple processing, thereby, becoming the main driver leading us to ANN employment.

Using such a set of input parameters, we acquired a dataset of 98 points (Table S1) with 4 key performance SWCNT parameters: the diameter distribution (mean and standard deviation (hereinafter d_{CNT} and σ_d), the yield, the ratio of intensities of G and D modes of a Raman spectrum (I_G/I_D). Fig. 5.1 shows a typical range of key performance parameters within the dataset: Raman spectroscopy provides the I_G/I_D ratio, UV-vis-NIR spectroscopy allows us to estimate the thickness of the film, which is proportional to the absorbance (according to the Berr-Lambert law), and the diameter distribution that can be reliably calculated in the case of CO-based process from the Van Hove singularities of the S_{11} transition [23], [74] (Fig.5.2 a). The thickness of the film provided by UV-vis-NIR spectroscopy corresponds to the yield and allows(ensures) more precise validation than gravimetric studies owing to the low weight of thin SWCTN films we dealing with.

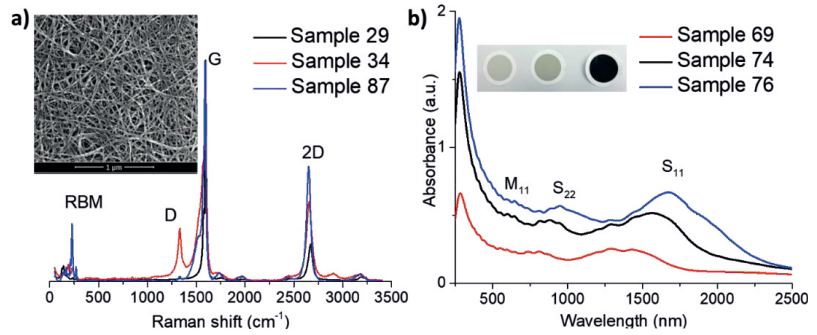


Figure 5.2: Typical data describing SWCNTs: (a) Raman spectra with a typical SEM microphotograph (the inset); b) UV-vis-NIR spectra with the photograph inset of the SWCNT films of different thicknesses.

5.2. DESIGN OF ANN MODEL

Self-geometry of the ANN is based on a sequential model developed in Python programming language using the Keras open-source neural-network library. We vary hyperparameters of the ANN (the number of hidden layers, number of nodes, activation function, optimizer, batch size, number of training epochs as shown in Table 5.1) to define the optimal ANN architecture and conditions providing minimal errors. For simplification of the training process we use 4 independent ANN with the same key input parameters and 4 single outputs: either d_{CNT} , σ_d , the yield or I_G/I_D (Table S1). We use the mean absolute error (standard deviation) as a loss and mean absolute percentage error (relative standard deviation) as statistical criteria for the accuracy of the ANN prediction.

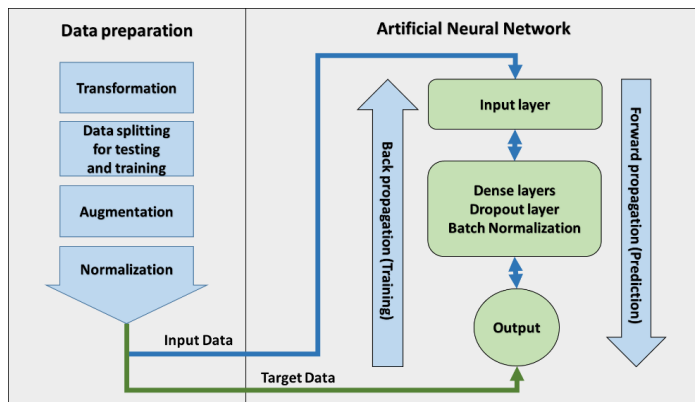


Figure 5.3: Scheme for the data preparation and processing in the ANN.

Input data are handled in the following way (Fig.5.3). First, we transform the experimental data (temperature distribution, gas flowrates and reactor geometry) into five key input parameters (partial pressures of gaseous components, residence time and reactor temperature). Then, we shuffle the samples and randomly split the data into training (80%) and validation (20%) datasets. We obtain the input as an array of n -dimensional vectors $[[\mathbf{X}_{11} \dots \mathbf{X}_{1n}] \dots [\mathbf{X}_{i1} \dots \mathbf{X}_{in}]]$, where $n = 5$ is the number of key input parameters, i is the index number in the dataset from 1 to 98. Third, we employ a common data augmentation [80] that provides a dataset of a size acceptable for the ANN training and, thereby, significantly improves the prediction performance (table 5.2). Each experimental vector can be transformed in a family of vectors (20 in our case) by normal randomization of each coordinate with a dispersion, which is equal to the standard deviation of the corresponding key input parameter. As the key input parameters have 4 orders of magnitude deviation, in prior to feeding the input neurons, the data were normalized as $X=(X-X_{\text{mean}})/\sigma$, where σ is the dispersion of a parameter.

Table 5.1: Hyperparameters for different targets.

| Hyperparameters | The ANN for the mean diameter | The ANN for the Yield | The ANN for the I_G/I_D | The ANN for the σ_d |
|---------------------------|-------------------------------|-----------------------|---------------------------|----------------------------|
| Number of hidden layers | 3 | 3 | 3 | 3 |
| Number of nodes | [512, 256, 128] | [512, 256, 128] | [512, 256, 128] | [512, 256, 128] |
| Activation function | Relu* | Relu | Relu | Relu |
| Optimizer | Adam** | Adam | Adam | Adam |
| Batch size | 16 | 32 | 32 | 28 |
| Number of training epochs | 800 | 120 | 60 | 60 |
| Batch Normalization | "+" | "+" | "+" | "+" |
| Dropout | 0.5 | 0.3 | 0.3 | 0.3 |

*Relu – **R**ectified **L**inear **U**nit used as an activation function in a machine learning, a standard component of the Keras library [81]

**Adam is an algorithm for the first-order gradient-based optimization of stochastic functions integrated into the Keras library as one of the standard functions[82]

We manually vary hyperparameters of the ANN to define the optimal ANN architecture and conditions providing minimal errors. However, the Keras library also supports automatic optimization of hyperparameters as 'Tensor Flow' backend support GPU calculation for the faster training process.

5.3. PERFORMANCE VALIDATION OF ANN

The ANN training (Fig. 5.3; Table 5.1) can be represented as a simple iteration algorithm consisted of a set of epochs: forward(direct) propagation of input vectors through the ANN is followed by back propagation of errors (error distribution for the nodes to correct the weights).

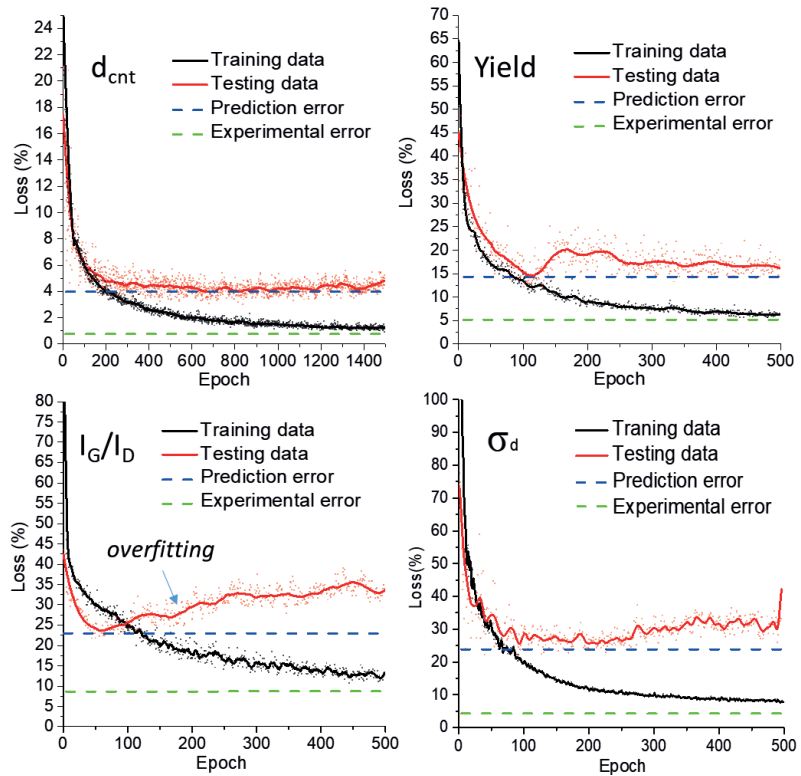


Figure 5.4: Evolution of losses of the key performance parameters of the SWCNT synthesis using ANN. The values for corresponding experimental and prediction errors are 8% and 23% (I_G/I_D), 5% and 14% (Yield), 0.7% and 4.0% (d_{CNT}), 4 and 22% (σ_d), respectively.

Table 5.2: Losses for key output parameters corresponding experimental and prediction errors (with and without data augmentation)

| Key output parameter | Experimental error | Prediction with data augmentation | Prediction without data augmentation |
|----------------------|--------------------|-----------------------------------|--------------------------------------|
| I_G/I_D | 8% | 23% | 45% |
| Yield | 5% | 14% | 25% |
| d_{CNT} | 0.7% | 4.0% | 10% |
| σ_d | 4 % | 22% | 51% |

We achieve the modelling error comparable with the experimental error (based on the parameter dispersion throughout repetitive experiments; Fig. 5.5) proving the methodology proposed (Fig.5.4; Table 5.1). After a certain number of epochs (iterations), we naturally observed the common overfitting by the ANN that can be attributed to the description of the training data too closely that it fails to process additional dataset (testing data) accurately [83]. It is worth noting that the ANN show a good prediction of the experimental output parameters when compared to real values. For instance, the mean absolute percentage error for the diameter is 0.7%, which corresponds to the ANN accuracy of the prediction <0.1 nm. The approach employed can be extended to the other performance parameters of the collected SWCNT thin films: sheet resistance, length distribution, chirality distribution, *etc.*

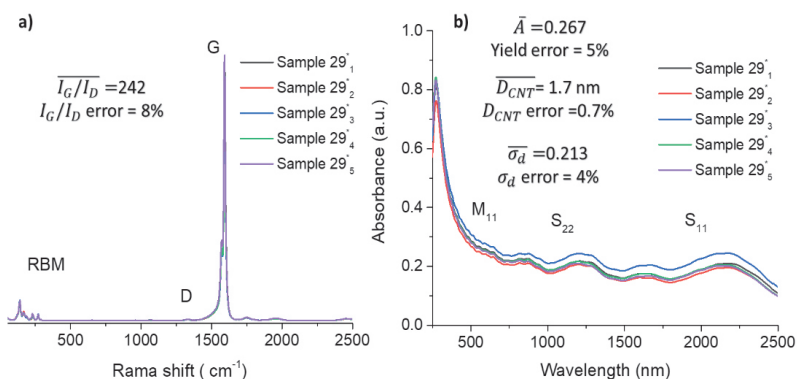


Figure 5.5: Estimation of the experimental error (standard deviation) based on repetitive experiments under the same synthesis conditions (Sample 29): Raman spectra with a typical SEM microphotograph (a); UV-vis-NIR spectra (b).

Thus, for the first time, we employ the artificial neural network methodology for the synthesis of SWCNTs. Using relatively small set of training data (98 points), we achieve a good agreement between the key input parameters of the nanotube growth (partial pressures of CO, CO₂, the catalyst precursor as well as the residence time and the reaction temperature) and the prediction of the key performance characteristics of the SWCNT synthesis (the yield, mean and standard deviation of nanotube diameter distribution, I_G/I_D intensity ratio of Raman spectra). Thus, the results obtained justify further studies. We believe this methodology is to provide a facile resource-efficient path for processing and collecting the comprehensive data. Moreover, it makes possible to reveal hidden dependencies in the case of multiple input parameters. However, such results are the subject of our future research. The ANN employment within the thesis provides a simple route for the synthesis of SWCNTs with predefined properties.

6. LASER TREATMENT OF SWCNT FILMS

The optoelectronic performance of thin SWCNT films is mainly affected by the transmittance and conductivity. However, an increase of the transmittance usually inevitably yields to a decrease in the conductivity. The problem is generally addressed by a modification of the SWCNT films either by patterning [17], or by chemical doping, hybridization with other materials [18] to get high T/R ratio [19,20]. The chemical doping is shown to be one of the most efficient, allowing the decrease of the sheet resistance of the CNT films. However, they still require further improvement to reach the performance of the ITO. While the chemical doping targets the resistance of the CNT films, the transmittance can be improved by the film patterning. However, for a continuous SWCNT film, the improvement of the transmittance (without radical changes in the resistance) could be realized by removal of impurities from the nanotubes, which are often represented in the form of byproducts like amorphous carbon and catalyst particles and might contribute to the light absorption by the SWCNT films. Synthesized nanotubes remain attached to the catalyst particles being trapped in the carbon shell. The light absorption of the catalyst particles like metallic Fe particles influences the overall SWCNT film transmittance.

In this chapter, we have developed a method based on the laser irradiation of SWCNT films to minimize the effect of the undesired byproducts and therefore, to improve their optical properties. Generally, the laser treatment has been already used to change the CNT structure mainly driven by the rapid increase of the film temperature under the induced energy. Low power density radiation stimulates some changes at defect sites of the CNTs, which ordinarily remain undamaged. At a higher power density, the nanotubes are transformed into different nanocarbon forms. Moreover, laser treatment, as a scalable, “dry” and local method could be beneficial for the improvement of electrical contact resistance at carbon nanotube/metal interface, reported as laser-assisted nanowelding.

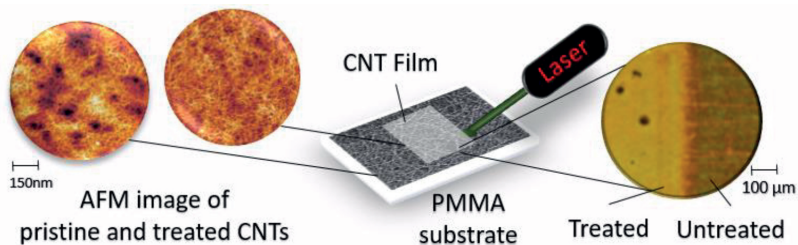


Figure 6.1: Schematic presentation of the laser treatment of SWCNT films on a PMMA substrate.

The treatment of the SWCNT films was conducted by a continuous wave laser with a wavelength of 532 nm. The diameter of the laser spot was about 35 μm . Depending on the film absorption, we varied the laser power and the exposure time to find optimal parameters which would allow us to apply the maximum power preserving the polymeric substrate. The laser treatment was conducted in the power density range from 7.0 to 32.0 kWcm^{-2} with a spot exposure time varied from 0.075 to 0.15 s. The optimized values used for the treatment were recalculated to the energies: 6.05, 4.24, 1.37 and 1.08 kJ cm^{-2} respectively applied to treat the films with thicknesses of 160, 130 nm, 80, 35 and 25 nm.

The optical image of the SWCNT film treated by a laser is presented in Fig. 6.2 a. The results show a clear difference between treated and untreated film areas. The treatment affects the optical characteristics of the SWCNT film, in particular, the treated area is more transparent. At the same time, SEM results indicate the absence of significant changes in the film morphology after laser treatment when compared to the untreated film (Fig. 6.2 b). By AFM studies, we demonstrate that both treated and untreated SWCNT films appear to be morphologically almost the same. However, the overall height difference is about 25 % lower for the processed films, which indicate that the irradiated films are more flattened or densified (Fig.6.2 c,d).

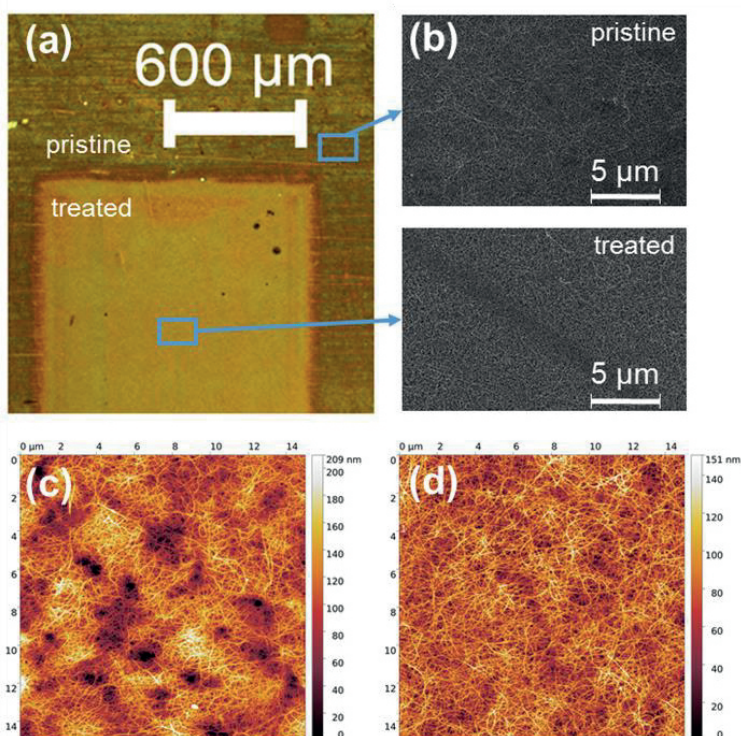


Figure 6.2: Optical overview and morphology evaluation of pristine and laser treated (5.54 kJcm^{-2}) 130 nm SWCNT films placed on a PMMA substrate: a) optical microscopy image; b) SEM micrographs; AFM topography images of c) pristine and d) laser treated areas, $15 \times 15 \mu\text{m}^2$.

In order to evaluate the influence of the laser treatment on the structure of the SWCNTs, we have recorded Raman spectra of the pristine and treated SWCNT films (Fig. 6.3). G/D ratio of the peak intensities changes insignificantly from 160 to 130. RBMs of the treated sample is shape-identical to the RBMs of the pristine one, which confirms the material composition, i.e. tube diameters, to be virtually unchanged. Thus, the short-term exposure of the laser radiation on SWCNT films positioned on the PMMA substrate does not have a great effect on the structure of the SWCNTs composing the film.

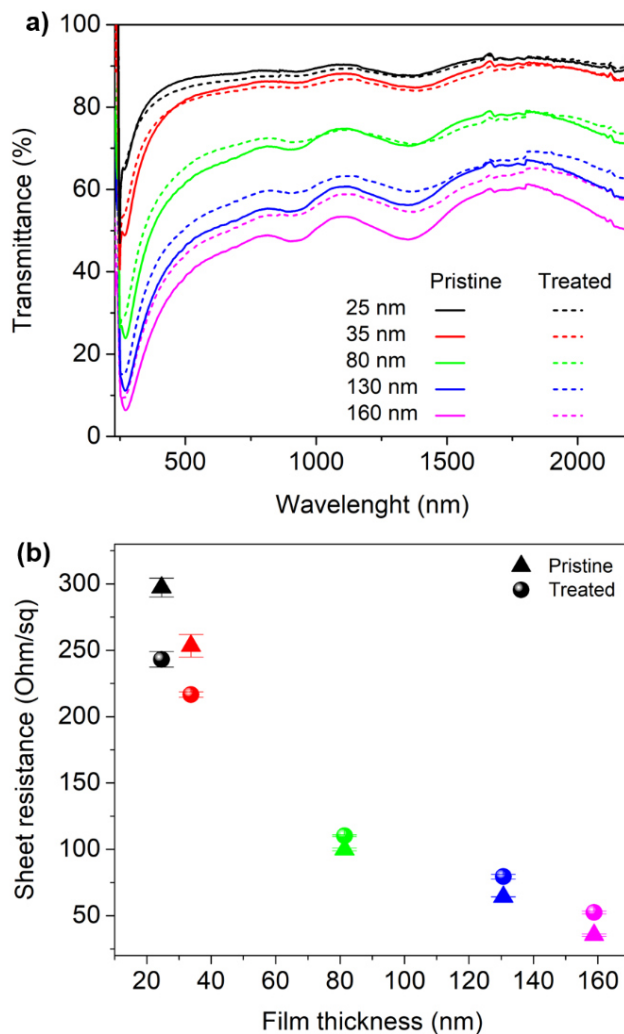


Figure 6.3: Sheet resistance versus thickness of the SWCNT-PMMA samples of the pristine (triangle) and the treated films (circles).

We have evaluated the sheet resistance and transmittance of the pristine and the treated SWCNTs films depending on the film thickness. Laser treatment results in SWCNT films with increased transmittance (up to 4%). At the same time, the sheet resistance changes are not pronounced and are within the accuracy of the estimation.

To further examine and compare the chemical composition of the pristine and the laser-treated films, we have studied the XPS spectra. We have observed (Table 6.1) an increase and a slight shift towards higher

binding energies of Fe-oxide peaks in the case of the treated film while the peak of metallic iron reduces confirming the oxidation of iron particles [84]. Although oxidized Fe is identified even in the pristine film (appeared following oxidation of inactive catalyst particles), its concentration increases in the treated films. XPS spectrum of oxygen indicates the adsorbed oxygen (or C=O bond), the oxygen chemically bonded to carbon (C-O), and O-Fe bond.

Table 6.1: Total atomic concentration of C, O and Fe of the pristine and the treated (5.54 kJcm⁻²) SWCNTs film, 130 nm, placed over(onto) polymeric substrate.

| Sample | Pristine | Treated |
|---|-----------------|----------------|
| C (at.%) | 94.7 | 94.7 |
| O _{Total} (at.%) | 5.0 | 5.0 |
| Fe _{Total} (at.%) | 0.3 | 0.3 |
| Fe _x O _y (at.%) | 0.5 | 1.0 |
| Fe _x O _y /Fe _{Total} | 0.3 | 0.7 |

Table 6.2: Sheet resistance and equivalent sheet resistance of pristine and treated SWCNTs (532 nm, 5.54 kJcm⁻²) placed over(onto) polymeric substrate depending on the film thickness.

| SWCNT film thickness, nm | 160 | 130 | 80 | 35 | 25 |
|--|------------|------------|-----------|-----------|-----------|
| <i>R_e</i>, Ohm/sq (pristine) | 382 | 382 | 469 | 438 | 300 |
| <i>R_e</i>, Ohm/sq (treated) | 364 | 471 | 372 | 483 | 385 |

Thus, we have developed a technique for improving the optoelectronic performance (table 6.2) of SWCNT films. The laser treatment has no significant effect on the SWCNT structure and, thereby, on conductivity while laser-induced oxidation of the Fe catalyst particles leads to an increase in transmittance (to 4% at 550 nm).

7. APPLICATIONS OF THIN FILMS

7.1. BOLOMETERS

Infrared (IR) detectors play an important role in modern technologies and are widely used in various fields, including military applications. Photonic and thermal detectors are two main types of IR detectors which are currently employed. In photonic detectors, radiation is absorbed by the material as a result of direct interaction of photons with charge carriers. These detectors include photovoltaic and photoemission detectors, photoconductive detectors, quantum well detectors, etc.

In thermal detectors, incident radiation is absorbed by the material, which leads to a temperature rise and a subsequent change in some physical properties of the material, such as resistance. Unlike thermal detectors, photon detectors exhibit wavelength-selective sensitivity, better signal-to-noise ratio and high response time. The advantages of thermal detectors are the simplicity of the design and the absence of necessity in cryogenic cooling, which significantly reduces energy consumption and cost of this type of devices, making them most common for civil applications [85]–[87].

The search for new sensor materials for IR detectors is still urgent. Over the past ten years, carbon nanotubes have been used in the development of detectors based on different mechanisms of conductivity variation due to electromagnetic radiation [88].

Further studies of the CNT bolometer development have been conducted mainly in two directions. The first direction represents the use of thin suspended films of pristine nanotubes [89], while the second one assumes the development of a bolometric sensor based on a composite of various polymers and nanotubes [90]–[93].

Carbon nanotubes have a number of properties that allow one to consider them as a promising bolometric sensor. They have a low thermal capacity, high thermal conductivity and high strength. Moreover, the use of various chemical and physical methods for nanotube modification makes it possible to vary their optical and electrical

properties over a wide range (in the present research, the studied IR absorption range is 1-30 μm). The voltage sensitivity of a bolometric element is determined by the expression [94]:

$$R_v = IR\alpha R_{th}\varepsilon, \quad (7.1)$$

where $R_{th} = G_{th}^{-1}$ is thermal resistance; G_{th} is thermal conductivity between a sensor and a substrate; ε is the coefficient of IR radiation absorption; $\alpha = R^{-1} \frac{dR}{dT}$ is the temperature coefficient of resistance; R is the sensor resistance; and I is the current through the sensor. Thus, the higher the coefficients α and ε and the lower the thermal conductivity, the higher the detector sensitivity. On the other hand, the bolometer operating speed is determined by a characteristic response time of the sensor to the change in irradiance:

$$\tau = C/G_{th}, \quad (7.2)$$

where C is the heat capacity of the absorber and sensor. Consequently, the lower the sensors heat capacity, the faster it reacts to changes in the intensity of IR radiation.

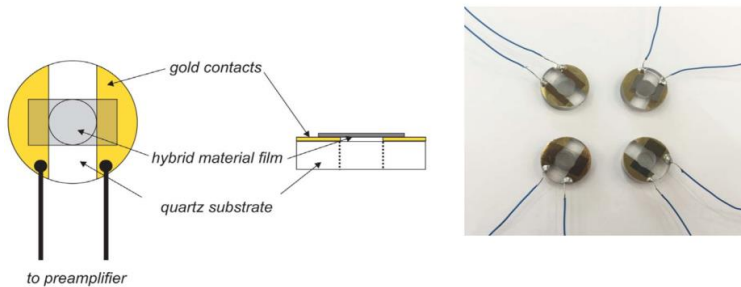


Figure 7.1: Bolometer devices based on free-standing SWCNT films.

In this chapter, we examine bolometric characteristics and parameters of pristine SWCNT films suspended over the hole. This allowed us to design a bolometer with a unique speed of response parameters owing to the low heat capacity of the sensor (film thickness ~ 40 nm) and to increase its sensitivity due to the low thermal conductivity between the sensor and substrate. Fig. 7.2 shows the main characteristics of the samples.

More precise conclusions on the bolometer efficiency can be derived in accordance with the absolute voltage sensitivity, time constant and noise-equivalent power (NEP). These measurements were carried out at room temperature and a pressure of 1 mbar. The waveform response to the modulated radiation represents a train of rectangular pulses. By measuring the sample response speed to switching on/off laser radiation at a pressure of 1 mbar, and room temperature a time constant of 2,6 ms. was obtained.

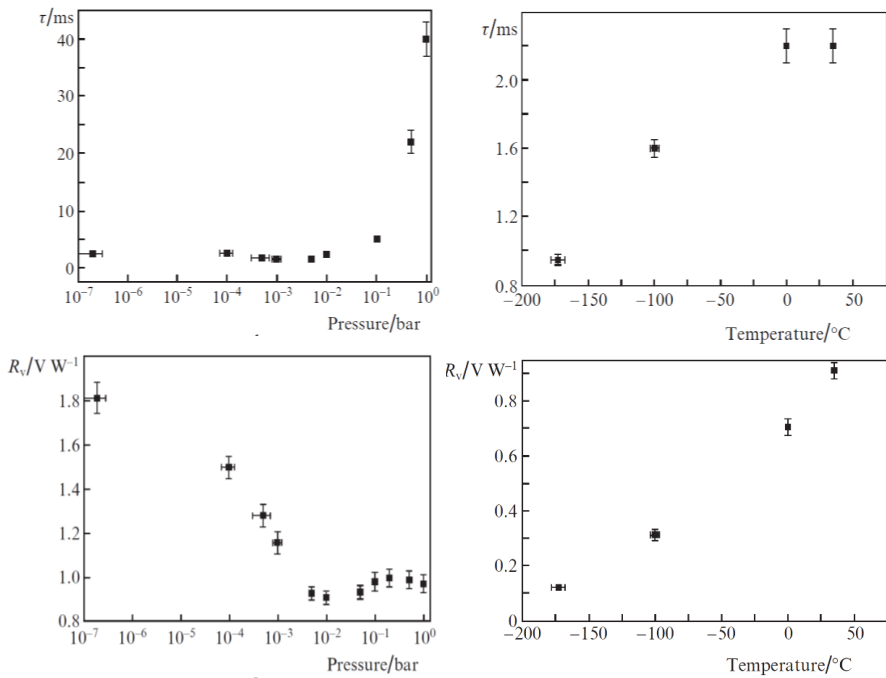


Figure 7.2: Demonstration of voltage sensitivity and response time from environmental temperature and pressure.

Obviously, with decreasing pressure, the time constant, which is inversely proportional to the thermal conductivity, increases. This is actually observed at pressures below 1 – 10 mbar: the time constant under high vacuum increases 1.5 – 2 times. On the other hand, the sample response time sharply enlarges at pressures above 100 mbar. Apparently, this reflects the influence of the layer of air to the thermal capacity of the system. The irradiated sample heats the adjacent layer of air, the thermal conductivity of which is low. As a result, the sample reacts slowly to the changes in irradiation.

Thus, concerning the response time, the pressure range from 10^3 – 10^{-1} bar is optimal for a bolometer of this type, even though the sensitivity is better at lower pressures. Also, a high vacuum is technologically more difficult to maintain.

The sensitivity drops significantly with lowering the sample temperature. This may be stipulated for several reasons. First, with decreasing temperature, the temperature coefficient of the sample resistance also decreases. Secondly, due to the fact that the SWCNTs we have used to have the metallic nature of the resistance dependence on temperature (Fig 7.3), the sample resistance decreases several times down to liquid nitrogen temperature. It is also possible that the thermal conductivity of the sample grows with cooling. The latter assumption is confirmed by the temperature dependence of the time constant. A decrease in temperature from $+33^\circ\text{C}$ to -173°C increases twice the sample response time. The noise equivalent power increases with decreasing temperature, which is associated with a reduction in the sample sensitivity. Thus, the NEP increases only fivefold, whereas the signal level falls nine times. Obviously, this is because the total noise level and the temperature-related resistance also decrease with lowering temperature. From this, we may conclude that the additional cooling of the bolometer based on the nanotubes we have used in this work is inadvisable due to a strong reduction in sensitivity while cooling. The sensors made of nanotubes with semiconductor properties can have different nature of the temperature sensitivity dependence due to an increase in the temperature coefficient of resistance at liquid nitrogen temperatures.

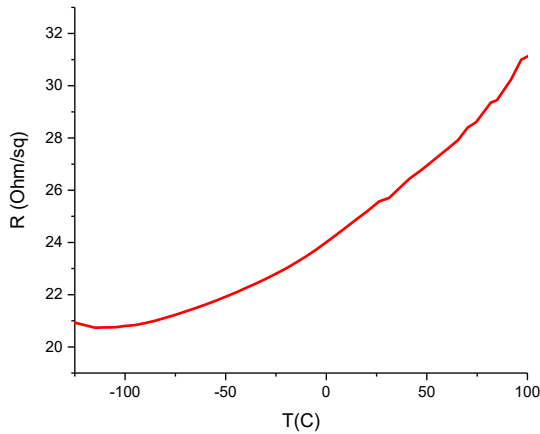


Figure 7.3: Temperature dependence of the sheet resistance of SWCNT films.

Thus, a bolometric sensor based on free-standing thin SWCNT film was shown to possess a small response time of 2.6 ms (at room temperature and 1 mbar pressure). This is several times better than the response time of corresponding commercial bolometers. Moreover, the response time may be reduced (up) to 1 ms at the temperature– 175°C.

7.2. SATURABLE ABSORBERS

Since last decade pulse fiber lasers have proven to be a reliable source for applications in medicine, optical tomography and spectroscopy, and material processing. Saturable absorbers (SAs) play a crucial role in the passive pulse generation of the fiber lasers. If a wave train propagates through a SA, then shortening of the pulse duration is observed because of strong nonlinear absorption (low intensity of the wave train exhibits higher absorption compared to high intensity ones). In this case, SWCNT electronic structure with van Hove singularities could be considered as a classical two-level system favorable for the SA operation».

Nowadays, there is a number of novel materials that have been thoroughly investigated as an alternative of a standard SESAM (Semiconductor Saturable Absorber Mirror) for an ultrafast fiber optics:

graphene [95], [96], black phosphorous [97], [98], topological insulators [99] and transition-metal dichalcogenides (MoS₂ [100], MoSe₂ [101]) etc. In parallel, carbon nanotubes have been widely explored and demonstrated to provide a good performance because of their excellent properties, such as wideband operation, fast recovery time, and stability [102]. The first pulsed fiber laser based on a SWCNT saturable absorber with mode-locked pulses was demonstrated in 2004 [103]. It is worth mentioning that 66 fs-long mode-lock pulse generation has been achieved with a carbon nanotube saturable absorber [104], which is close to the world record of 37 fs pulse generation in erbium-doped fiber lasers [105]. The most widely used approach implies SA based on SWCNTs (SWCNT-SA) in the form of an SWCNT polymer composite. However, when compared to SWCNT films, the polymer might substantially decrease the stability of SWCNT-SA due to lower thermal damage threshold of polymers compared to SWCNTs [106]–[108]. In this chapter, thin film of SWCNTs was directly deposited [22], [109] on the fiber ferrule to work in the erbium and bismuth all fiber laser scheme. In order to avoid the damage of SWCNTs (the laser power is limited), we attach SA on a side-polished or tapered fiber [104], [110]–[117], so that only the evanescent tail of the light, propagating through the fiber, interacts with the SWCNTs. This method dramatically increases the limit of the output laser power (up) to hundreds of mW.

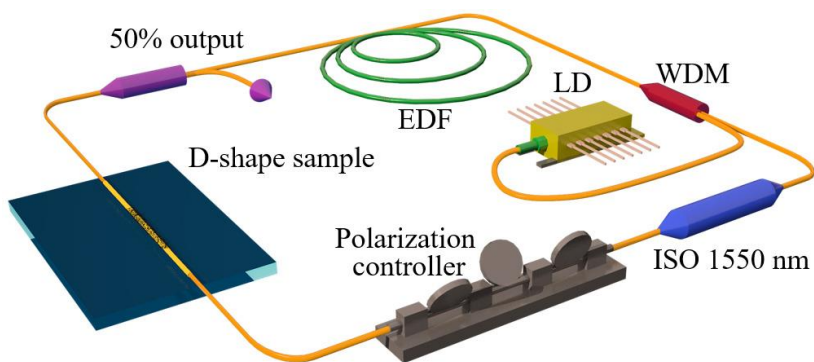


Figure 7.4: Principle scheme of SWCNT-SA.

The diameter distribution of SWCNTs was adjusted for the absorption peak fit to the emission line of the erbium-doped fiber laser (1560 nm).

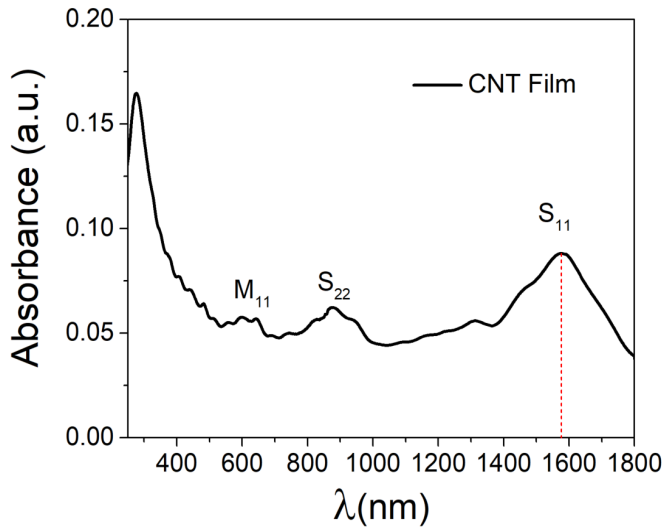


Figure 7.5: Absorbance spectra of SWCNT used for SA.

D-shape fibers are produced by Phoenix Photonics with a standard single-mode fiber (SMF28) with a 17 mm side-polished region. It correspondingly has insertion losses of 0.1 and 56 dB with air and index-matched oil with the refractive index of 1.5. To deposit SWCNTs from the filter onto the D-shape fiber, we use the dry transfer technique: SWCNTs collected on the filter are simply transferred by pressing towards the D-shape fiber surface (Fig. 7.6). The weak adhesion of the SWCNT films to the nitrocellulose filter and the strong adhesion to the quartz ensure nanotubes stick to the D-shape fiber surface. The absorption of the saturable absorber can be controlled by the thickness and the length of the deposited SWCNT film.

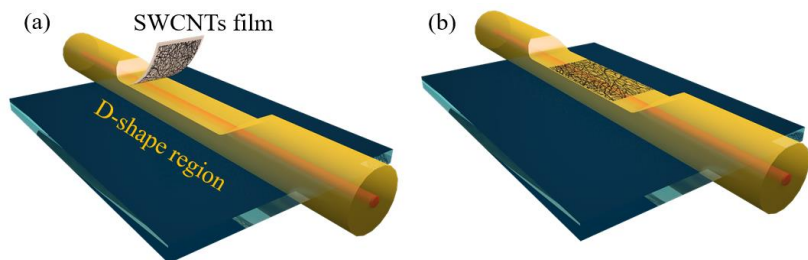


Figure 7.6: Schematic view of the SWCNT deposition onto the D-shape fiber using the dry transfer technique: (a) filter with the collected SWCNTs approaches and being pressed to the D-shape fiber, (b) SWCNTs deposited onto the D-shape fiber.

To test the saturable absorber, we implement it into the ring cavity fiber laser with relatively short resonator optimized for a stable laser generation. We use 1.4 meters highly doped erbium fiber with a dispersion of 45.9 ps^2 at 1555 nm (shown in Fig. 7.4). The laser is pumped by a diode laser at 980 nm with a maximum output power of 450 mW. It is followed by polarization insensitive isolator, a polarization controller, a sample and a 50/50 output coupler. The total length of the resonator is 7.65 m and the net dispersion is -0.07 ps^2 (anomalous dispersion).

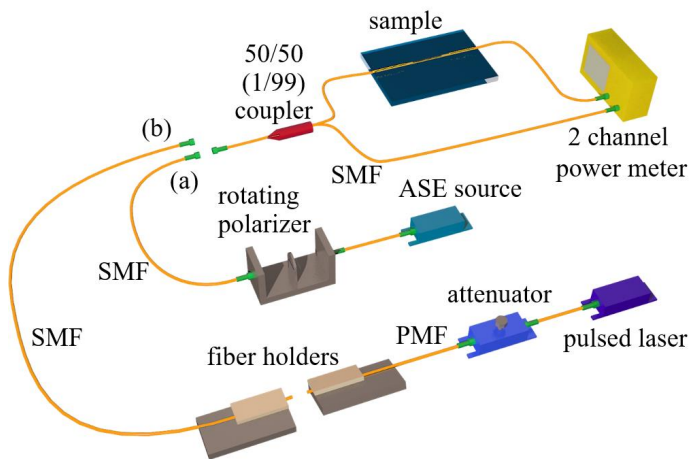


Figure 7.7: Experimental setup for measurements of a) polarization depended losses (PDL) of the SWCNT-SA on a D-shape fiber with a rotating polarizer, b) sample nonlinear transmittance.

For a saturable absorber on a side-polished fiber, the rotation of a polarization controller can switch laser generation between different pulse regimes [118]. Further, we demonstrate the Q-switched regime and harmonic mode-lock (HML) generation obtained by proper polarization controller adjustment. We believe that the polarization controller rotation changes the linear and nonlinear loss amplitudes resulting in switching between different pulsating regimes [119]. By rotation of the polarization controller, we find a Q-switched pulse generation shown in Fig. 7.8 a. The pulse parameters obtained from Fig. 7.8 for a pump power of 450 mW are the following: output power is 20 mW, Q-switched pulse duration measured from the pulse train is 1.27 μs , the pulse energy is 0.114 μJ , the spectral FWHM is 0.19 nm (Fig. 7.8 b), and the repetition rate is 175 kHz. By rotation of the polarization controller, we find the soliton pulses with minimal energy pulse spectra of all HML orders, from the 1st to the 27th. We can see that the central wavelength does not change. Spectral FWHM increases from 1.1 to 2.8 nm with the HML order increase from the 1st to the 27th (ones).

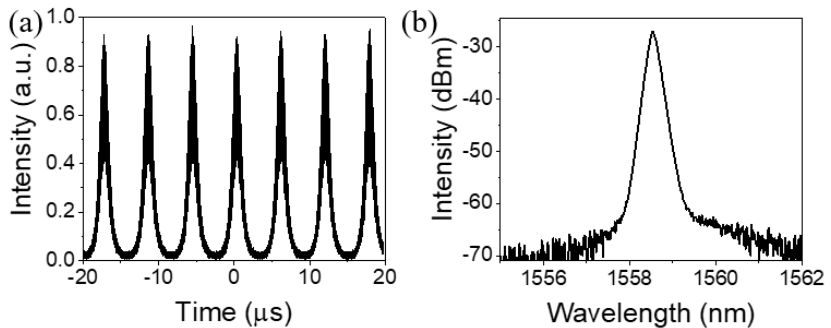


Figure. 7.8: Q-switched pulse generation: (a) pulse train with the FWHM of 1.27 μs and repetition rate of 175 kHz, (b) pulse spectrum with the FWHM of 0.19 nm.

Thus, we have demonstrated a dry transfer technique for a polymer-free single-walled carbon nanotube saturable absorber fabrication on a side-polished fiber. Fine-tuning of SWCNT properties allows fitting for particular absorbance peak on the sated wavelength of laser radiation. Moreover, dry transfer of thin SWCNT films on a surface of the side-

polished fiber allows enhancing the power density carbon nanotube saturable absorber fabrication in evanescent field interaction configuration in an easy, robust and controllable (manageable) way. The saturable absorber was fabricated with relatively low loss of 3.4 dB in nonpolarized light and possessed polarization-dependent on a loss of 1.3 dB to exclude nonlinear polarization evolution contribution to the pulse shaping.

7.3. FIBER BRAGG GRATINGS

Fiber Bragg gratings (FBGs) are used in many optical and optoelectronic applications. Possessing unique spectral characteristics, FBGs are employed as mirrors of fiber laser cavities and optical converters for stabilizing the wavelength of semiconductor lasers as narrow-band filters and dispersion compensators in fiber-optic communication systems as sensing elements of fiber-optic sensors for a variety of applications [120] and other purposes.

The resonance wavelength of an FBG written into a single-mode fiber is determined by the phase matching condition $\lambda_{BG} = 2n_{eff}\Lambda$ (where n_{eff} is the effective refractive index of the fundamental mode of the fiber and Λ is the FBG period). Controlled precision tuning of the resonance wavelength of an FBG, required to tune the frequency of laser sources, as well as in fiber-optic sensors, optical modulators, switches and gates, is typically ensured by longitudinal deformation of the FBG-containing fiber section or by varying its temperature [121]. In the case of fiber deformation, the change in λ_{BG} is mostly due to the change in grating period Λ , whereas the temperature primarily influences n_{eff} [122]. The longitudinal fiber deformation allowed λ_{BG} to be tuned over several tens of nanometers in ~ 1 ms, without significant changes in the shape of the FBG spectrum. If an FBG is heated by thin-film resistive coatings, the resonance wavelength tuning range is narrower, but the fiber is not subject to deformation, and there is no need to firmly secure it in a deformation system. In particular, Limberger *et al.* [121] demonstrated an λ_{BG} shift by 2.15 nm with an efficiency of 4.1 nm W^{-1} as a result of resistive heating of silica fiber coated with a thin platinum layer. A high

tuning efficiency (13.4 nm W^{-1}) was achieved using optical fiber based on polymethyl methacrylate (PMMA), whose refractive index is a stronger function of temperature [123].

A SWCNT-film applied as a coating on the lateral surface of a long-period fiber grating (LPFG) makes it possible to substantially improve the sensitivity of the resonance wavelength of such gratings to changes in the refractive index of the ambient medium [124]. We examine the feasibility of tuning the resonance wavelength of an FBG via the resistive heating of an SWCNT-based film produced on the lateral surface of fiber in the FBG region. We have studied characteristics of the coating based on single-wall carbon nanotubes applied to the lateral surface of an optical fiber via dry transfer. The proposed technique for producing a coating from nanotubes obtained by chemical vapor deposition on a filter has been shown to ensure a high uniformity of the electrical and thermal properties of the coating along the fiber length and allow the fiber temperature to be tuned over a wide range by resistive heating of the coating. Note that the proposed technique for producing a nanotube coating on the fiber surface is sufficiently simple: it requires no specialized process equipment.

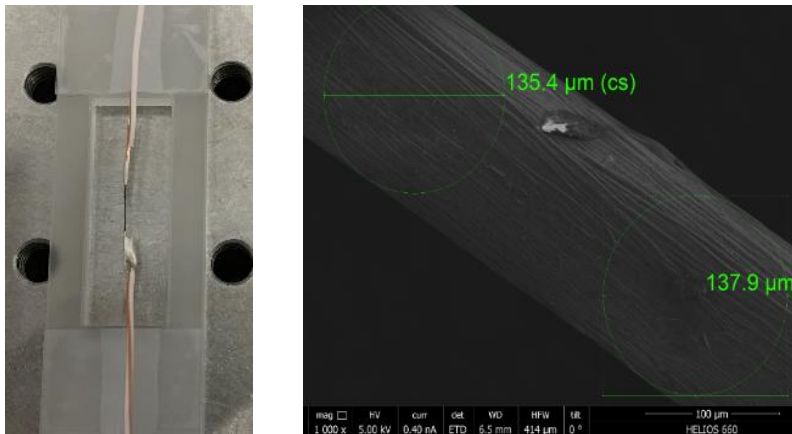
Fiber Bragg gratings were UV written into an SMF-28e standard telecom fiber by a frequency-doubled Ar⁺ laser (244 nm) using a Lloyd interferometer-based writing system [10]. To improve the photosensitivity of the fiber, it was first subjected to low-temperature hydrogen in a chamber at a pressure of ~ 100 atm and a temperature of $90 \text{ }^\circ\text{C}$ for 20 h. Molecular hydrogen remaining in the glass network after FBG inscription was removed by a similar heat treatment. The resonance wavelength of the FBGs was near $1.55 \text{ }\mu\text{m}$. The gratings ($\sim 4 \text{ mm}$ in length) had a high reflectivity ($\sim 99\%$) and a bandwidth (FWHM) of $\sim 0.5 \text{ nm}$.

Before FBG inscription, a $\sim 10\text{-mm}$ -long section of the fiber was mechanically stripped of the protective polymer coating. After grating inscription, a coating consisting of several tens of SWCNT-containing layers was produced on this section. The films were transferred from the filter surface to the lateral surface of the stripped fiber section containing

the FBG as follows: the film on the filter was pressed against the fiber and adhered to it. Next, it was wound onto the fiber (40 – 50 turns).

Fig. 7.9 shows a photograph of the device and scanning electron microscopy image of the lateral fiber surface coated with SWCNTs. An analysis of the SEM image showed that the coating was highly uniform along the fiber axis (there were no folds or other heterogeneities) and that its thickness was $\sim 2.2 \mu\text{m}$ (number of layers multiplied by the thickness of a single layer, *i.e.* SWCNT film thickness).

Figure 7.9: Optical and scanning electron microscopy image of an



optical fiber with SWCNT coating.

The electrical resistance of the coating was measured as a function of its length by the four-probe method using an MPI TS150 probe station and Keysight 34410A multimeter, and the results confirmed that the coating was spatially uniform. As seen in Fig. 7.10, the experimental data are well represented by a straight line with a slope of $1.3 \Omega\text{mm}^{-1}$

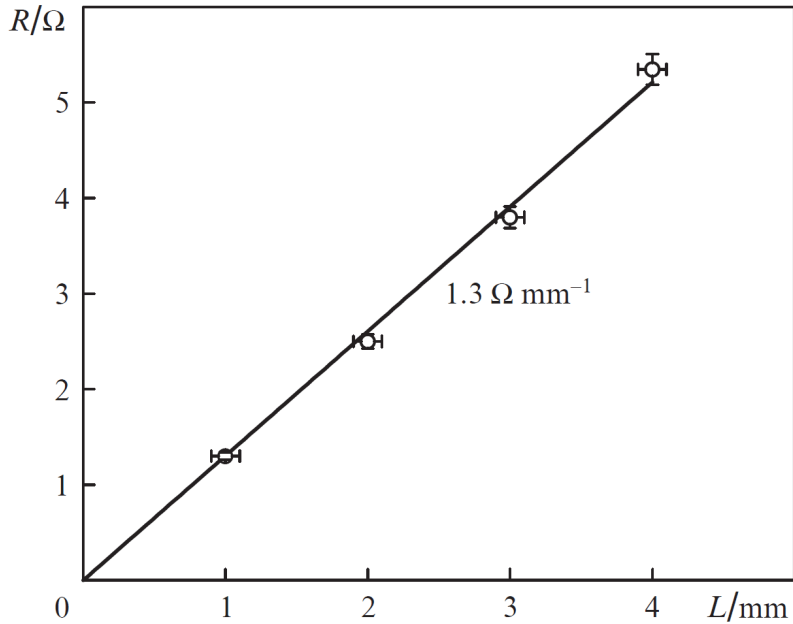


Figure 7.10: Electrical resistance of the coating measured as a function of the separation between the inner contacts by the four-probe method.

The experimental data presented in Fig. 7.11 demonstrate that, in the considered range, DIBG is a linear function of the electric power delivered to the coating, with a slope of 8.7 nm W^{-1} , which corresponds to the resonance wavelength tuning efficiency $\text{DIBG}/P = 4.3 \text{ nm cm W}^{-1}$ for an FBG of unit length. The right vertical axis in Fig. 7.11 represents the temperature change ΔT in the SWCNT-coated fiber section as estimated from the temperature sensitivity of IBG. It is seen that 0.2 W of electric power is sufficient for heating the fiber to 150°C . This power correlates with the value reported by Costantini et al. [18] for heating using the resistive metallic coating, assuming that the metallic coating was four times longer. In the case of steady-state heating, the temperature of the fiber is a linear function of the electric power delivered to it, which is well consistent with the data presented in Fig. 7.11. The heat transfer coefficient H of the surface of the SWCNT-coated fiber is $0.05 \text{ W K}^{-1} \text{ m}^{-1}$, which is derived from the slope of the line in Fig. 7.11. This value

coincides with that obtained by Costantini et al. [18] for a metal-coated fiber.

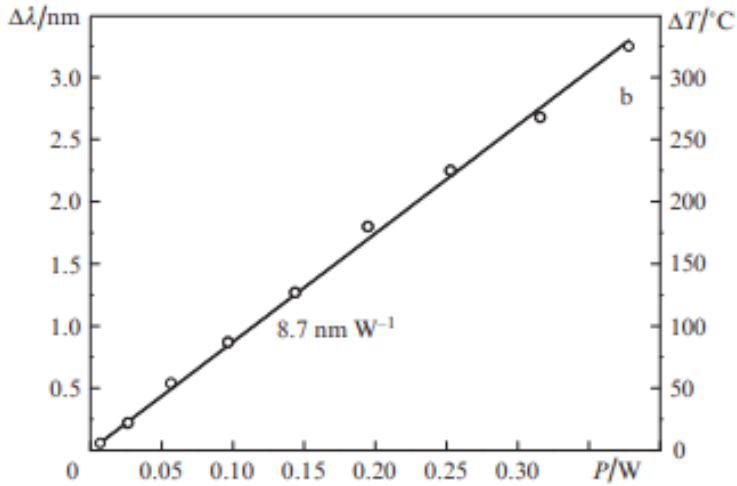


Figure 7.11: Effect of the electric power delivered to the coating on the resonance wavelength of the FBG.

A SWCNT films applied as a coating of a FBG-containing fiber section allowed us to tune the resonance wavelength of the grating over more than 3 nm with an efficiency of 8.7 nm W^{-1} , varying the electric power delivered to the coating. The present results demonstrate that the proposed fiber coating is a viable alternative to resistive metallic coatings and can be used not only to tune the resonance wavelength of FBGs but also to control (stabilize) the phase of a wave in fiber-optic interferometers and phase modulators if the desired phase change time exceeds 100 ms.

8. CONCLUSIONS

The problem of the synthesis of single-walled carbon nanotubes with tailored characteristics was addressed by the thorough study of the synthesis and data processing, followed by a demonstration of advanced applications of SWCNT films. The research resulted in the following achievements:

A new reactor for aerosol CVD growth of SWCNTs equipped with a spark discharge generator of catalyst nanoparticles was developed. The new design resulted in a more robust apparatus compared to ferrocene type of aerosol CVD reactors. Precise control over the size of a catalyst particle within a wide range of operating regimes makes the system for the SWCNT synthesis more scalable and stable.

Advanced control over the diameter distribution, defectiveness, and the yield was achieved by using for the first time the artificial neural networks. This allowed establishing a correlation between reactor parameters and key SWCNT characteristics. The new methodology turned to be useful for the adjustment of the diameter of the SWCNTs, the yield and the improvement of the quality of SWCNTs by minimization of amorphous carbon.

A novel technique for the post-synthesis improvement of electro-optical characteristics of SWCNT films by laser treatment was developed. In this process short pulse irradiation results in an increase of the transparency of SWCNT films without any changes in conductivity presumably due to oxidation of the catalyst residuals.

All new techniques and methods allowed to improve the synthesis of SWCNTs with defined characteristics and to create a new possibility for their use for various applications. Thesis work includes a description of three electro-optical devices at the state of the art performance level: i) a bolometer based on a freestanding SWCNT film showing response time of 2.6 ms at room temperature and 1 mbar pressure (several times higher than the corresponding industrially applied devices); ii) SWCNT-based heating element of fiber Bragg grid for smooth tuning of the resonant wavelength and a stable laser signal; iii) a saturable absorber based on SWCNTs showing femtosecond pulse generation and low degradation rate.

9. REFERENCES

- [1] S. Iijima, "Helical microtubules of graphitic carbon.," *Nature*, vol. 354, no. 6348, pp. 56–58, 1991.
- [2] H. Amara and C. Bichara, "Modeling the Growth of Single-Wall Carbon Nanotubes," *Top. Curr. Chem.*, vol. 375, no. 3, p. 55, Jun. 2017.
- [3] V. Jourdain and C. Bichara, "Current understanding of the growth of carbon nanotubes in catalytic chemical vapour deposition," *Carbon N. Y.*, vol. 58, pp. 2–39, Jul. 2013.
- [4] J.-P. J.-P. Tessonnier *et al.*, "Analysis of the structure and chemical properties of some commercial carbon nanostructures," *Carbon N. Y.*, vol. 47, no. 7, pp. 1779–1798, 2009.
- [5] K. J. MacKenzie, O. M. Dunens, and A. T. Harris, "An Updated Review of Synthesis Parameters and Growth Mechanisms for Carbon Nanotubes in Fluidized Beds," *Ind. Eng. Chem. Res.*, vol. 49, no. 11, pp. 5323–5338, 2010.
- [6] S. W. Jeong, J. Kim, and D. H. Lee, "Effect of operating variables on synthesis of multi-walled carbon nanotubes in fluidized beds," *Chem. Eng. Sci.*, vol. 134, pp. 496–503, 2015.
- [7] D. P. Brown, A. G. Nasibulin, and E. I. Kauppinen, "CFD-aerosol modeling of the effects of wall composition and inlet conditions on carbon nanotube catalyst particle activity," *J. Nanosci. Nanotechnol.*, vol. 8, no. 8, pp. 3803–3819, 2008.
- [8] O. Reynaud, A. G. Nasibulin, A. S. Anisimov, I. V. Anoshkin, H. Jiang, and E. I. Kauppinen, "Aerosol feeding of catalyst precursor for CNT synthesis and highly conductive and transparent film fabrication," *Chem. Eng. J.*, vol. 255, pp. 134–140, 2014.
- [9] A. E. Agboola, "Development and model formulation of scalable carbon nanotube processes: HiPCO and CoMoCAT process models," 2005.
- [10] M. F. L. De Volder, S. H. Tawfick, R. H. Baughman, and A. J. Hart, "Carbon nanotubes: present and future commercial applications," *Science (80-.)*, vol. 339, no. 6119, pp. 535–539, 2013.
- [11] R. Rao *et al.*, "Carbon Nanotubes and Related Nanomaterials: Critical Advances and Challenges for Synthesis toward Mainstream Commercial Applications," *ACS Nano*, p. acsnano.8b06511, 2018.
- [12] L. A. Girifalco, M. Hodak, and R. S. Lee, "Carbon nanotubes, buckyballs, ropes, and a universal graphitic potential," *Phys. Rev. B*, vol. 62, no. 19, pp. 13104–13110, Nov. 2000.
- [13] A. G. Nasibulin *et al.*, "Charging of aerosol products during ferrocene vapor decomposition in N₂ and CO atmospheres," *J. Phys. Chem. C*, vol. 112, no. 15, pp. 5762–5769, 2008.
- [14] P. C. Ma, N. A. Siddiqui, G. Marom, and J. K. Kim, "Dispersion and functionalization of carbon nanotubes for polymer-based nanocomposites: A review," *Composites Part A: Applied Science and Manufacturing*, vol. 41, no. 10, pp. 1345–

1367, 2010.

[15] A. Moisala, A. G. Nasibulin, D. P. Brown, H. Jiang, L. Khriachtchev, and E. I. Kauppinen, "Single-walled carbon nanotube synthesis using ferrocene and iron pentacarbonyl in a laminar flow reactor," *Chem. Eng. Sci.*, vol. 61, no. 13, pp. 4393–4402, 2006.

[16] Q. Zhang, J. Q. Huang, W. Z. Qian, Y. Y. Zhang, and F. Wei, "The road for nanomaterials industry: A review of carbon nanotube production, post-treatment, and bulk applications for composites and energy storage," *Small*, vol. 9, no. 8, pp. 1237–1265, 2013.

[17] K. A. Shah and B. A. Tali, "Synthesis of carbon nanotubes by catalytic chemical vapour deposition: A review on carbon sources, catalysts and substrates," *Mater. Sci. Semicond. Process.*, vol. 41, pp. 67–82, 2016.

[18] Y. Maniwa *et al.*, "Multiwalled carbon nanotubes grown in hydrogen atmosphere: An x-ray diffraction study," *Phys. Rev. B*, vol. 64, no. 7, p. 73105, 2001.

[19] F. Ding, A. R. Harutyunyan, and B. I. Yakobson, "Dislocation theory of chirality-controlled nanotube growth," *Proc. Natl. Acad. Sci.*, vol. 106, no. 8, pp. 2506–2509, 2009.

[20] R. Zhang, Y. Zhang, Q. Zhang, H. Xie, W. Qian, and F. Wei, "Growth of half-meter long carbon nanotubes based on Schulz–Flory distribution," *ACS Nano*, vol. 7, no. 7, pp. 6156–6161, 2013.

[21] M. M. J. Treacy, T. W. Ebbesen, and J. M. Gibson, "Exceptionally high Young's modulus observed for individual carbon nanotubes," *Nature*, vol. 381, no. 6584, pp. 678–680, 1996.

[22] A. G. Nasibulin *et al.*, "Multifunctional free-standing single-walled carbon nanotube films," *ACS Nano*, vol. 5, no. 4, pp. 3214–3221, 2011.

[23] Y. Tian *et al.*, "Analysis of the Size Distribution of Single-Walled Carbon Nanotubes Using Optical Absorption Spectroscopy," *J. Phys. Chem. Lett.*, vol. 1, no. 7, pp. 1143–1148, Apr. 2010.

[24] S. D. Shandakov, M. V. Lomakin, and A. G. Nasibulin, "The effect of the environment on the electronic properties of single-walled carbon nanotubes," *Tech. Phys. Lett.*, vol. 42, no. 11, pp. 1071–1075, 2016.

[25] A. Kaskela *et al.*, "Aerosol-synthesized SWCNT networks with tunable conductivity and transparency by a dry transfer technique," *Nano Lett.*, vol. 10, no. 11, pp. 4349–4355, 2010.

[26] G. M. Mikheev, A. G. Nasibulin, R. G. Zonov, A. Kaskela, and E. I. Kauppinen, "Photon-drag effect in single-walled carbon nanotube films," *Nano Lett.*, vol. 12, no. 1, pp. 77–83, 2011.

[27] Y. Liao *et al.*, "Tuning Geometry of SWCNTs by CO₂ in Floating Catalyst CVD for High-Performance Transparent Conductive Films," *Adv. Mater. Interfaces*, vol. 1801209, pp. 1–10, 2018.

[28] V. L. Kuznetsov, A. N. Usoltseva, A. L. Chuvilin, E. D. Obraztsova, and J. M. Bonard, "Thermodynamic analysis of nucleation of carbon deposits on metal

- particles and its implications for the growth of carbon nanotubes," *Phys. Rev. B - Condens. Matter Mater. Phys.*, vol. 64, no. 23, pp. 2354011–2354017, 2001.
- [29] VI. Kuznetsov *et al.*, "Multi-walled carbon nanotubes with ppm level of impurities," *Phys. status solidi*, vol. 247, no. 11-12, pp. 2695–2699, 2010.
- [30] I. (Ib) Chorkendorff and J. W. Niemantsverdriet, *Concepts of modern catalysis and kinetics*. Wiley-VCH, 2007.
- [31] N. M. Mubarak, E. C. Abdullah, N. S. Jayakumar, and J. N. Sahu, "An overview on methods for the production of carbon nanotubes," *J. Ind. Eng. Chem.*, vol. 20, no. 4, pp. 1186–1197, 2014.
- [32] J.-P. Tessonnier and D. S. Su, "Recent progress on the growth mechanism of carbon nanotubes: a review.," *ChemSusChem*, vol. 4, no. 7, pp. 824–847, 2011.
- [33] I. Rafique, A. Kausar, Z. Anwar, and B. Muhammad, "Exploration of epoxy resins, hardening systems, and epoxy/carbon nanotube composite designed for high performance materials: a review," *Polym. Plast. Technol. Eng.*, vol. 55, no. 3, pp. 312–333, 2016.
- [34] C. H. See and A. T. Harris, "A Review of Carbon Nanotube Synthesis via Fluidized-Bed Chemical Vapor Deposition," *Ind. Eng. Chem. Res.*, vol. 46, no. 4, pp. 997–1012, 2007.
- [35] D. Sun *et al.*, "Flexible high-performance carbon nanotube integrated circuits," *Nat. Nanotechnol.*, vol. 6, no. 3, pp. 156–161, 2011.
- [36] T. Wang, D. Zhao, N. Alvarez, V. N. Shanov, and W. R. Heineman, "Optically transparent carbon nanotube film electrode for thin layer spectroelectrochemistry," *Anal. Chem.*, vol. 87, no. 19, pp. 9687–9695, 2015.
- [37] P. M. Rajanna *et al.*, "Enhanced efficiency of hybrid amorphous silicon solar cells based on single-walled carbon nanotubes and polymer composite thin film," *Nanotechnology*, vol. 29, no. 10, p. 105404, 2018.
- [38] D. S. Kopylova, N. Y. Boldyrev, V. Y. Iakovlev, Y. G. Gladush, and A. G. Nasibulin, "A bolometer based on single-walled carbon nanotubes and hybrid materials," *Quantum Electron.*, vol. 46, no. 12, p. 1163, 2016.
- [39] C. Dekker, S. J. Tans, and A. R. M. Verschueren, "Room-temperature transistor based on a single carbon nanotube," *Nature*, vol. 393, no. 6680, pp. 49–52, 1998.
- [40] A. A. Mkrtychyan, Y. G. Gladush, D. Galiakhmetova, V. Yakovlev, V. T. Ahtyamov, and A. G. Nasibulin, "Dry-transfer technique for polymer-free single-walled carbon nanotube saturable absorber on a side polished fiber," *Opt. Mater. Express*, vol. 9, no. 4, pp. 1551–1561, 2019.
- [41] S. Maruyama, "<http://www.photon.t.u-tokyo.ac.jp/~maruyama/kataur>," <http://www.photon.t.u-tokyo.ac.jp/~maruyama/kataur>, 2018. .
- [42] A. Jorio, E. Kauppinen, and A. Hassanien, "Carbon-nanotube metrology," in *Carbon Nanotubes*, Springer, 2007, pp. 63–100.
- [43] A. C. Ferrari and D. M. Basko, "Raman spectroscopy as a versatile tool

for studying the properties of graphene," *Nat. Nanotechnol.*, vol. 8, no. 4, p. 235, 2013.

[44] A. Moisala, A. G. Nasibulin, S. D. Shandakov, H. Jiang, and E. I. Kauppinen, "On-line detection of single-walled carbon nanotube formation during aerosol synthesis methods," *Carbon N. Y.*, vol. 43, no. 10, pp. 2066–2074, 2005.

[45] S. D. Shandakov *et al.*, "Effect of gaseous and condensate products of ethanol decomposition on aerosol CVD synthesis of single-walled carbon nanotubes," *Carbon N. Y.*, vol. 126, pp. 522–531, 2018.

[46] A. Kaskela, K. Mustonen, P. Laiho, Y. Ohno, and E. I. Kauppinen, "Toward the Limits of Uniformity of Mixed Metallicity SWCNT TFT Arrays with Spark-Synthesized and Surface-Density-Controlled Nanotube Networks," *ACS Appl. Mater. Interfaces*, vol. 7, no. 51, pp. 28134–28141, 2015.

[47] K. Mustonen *et al.*, "Gas phase synthesis of non-bundled, small diameter single-walled carbon nanotubes with near-armchair chiralities," *Appl. Phys. Lett.*, vol. 107, no. 1, p. 013106, Jul. 2015.

[48] M. Fulem, K. Růžička, C. Červinka, M. A. A. Rocha, L. M. Santos, and R. F. Berg, "Recommended vapor pressure and thermophysical data for ferrocene," *J. Chem. Thermodyn.*, vol. 57, pp. 530–540, 2013.

[49] K. Kuwana, H. Endo, K. Saito, D. Qian, R. Andrews, and E. A. Grulke, "Catalyst deactivation in CVD synthesis of carbon nanotubes," *Carbon N. Y.*, vol. 43, no. 2, pp. 253–260, 2005.

[50] A. G. Nasibulin *et al.*, "Multifunctional free-standing single-walled carbon nanotube films," *ACS Nano*, vol. 5, no. 4, pp. 3214–3221, 2011.

[51] A. Roch *et al.*, "Optical absorption spectroscopy and properties of single walled carbon nanotubes at high temperature," *Synth. Met.*, vol. 197, pp. 182–187, 2014.

[52] P. Kulkarni, P. A. Baron, and K. Willeke, Eds., *Aerosol Measurement*. Hoboken, NJ, USA: John Wiley & Sons, Inc., 2011.

[53] K. Voelskow, M. J. Becker, W. Xia, M. Muhler, and T. Turek, "The influence of kinetics, mass transfer and catalyst deactivation on the growth rate of multiwalled carbon nanotubes from ethene on a cobalt-based catalyst," *Chem. Eng. J.*, vol. 244, pp. 68–74, 2014.

[54] A. Bazargan, Y. Yan, C. W. Hui, and G. McKay, "A Review: Synthesis of Carbon-Based Nano and Micro Materials by High Temperature and High Pressure," *Ind. Eng. Chem. Res.*, vol. 52, no. 36, pp. 12689–12702, Sep. 2013.

[55] A. S. Andreev *et al.*, "Internal field 59 Co NMR study of cobalt-iron nanoparticles during the activation of CoFe₂/CaO catalyst for carbon nanotube synthesis," *J. Catal.*, vol. 358, pp. 62–70, 2018.

[56] A. Voloshko, "Nanoparticle formation by means of spark discharge at atmospheric pressure," Université Jean Monnet - Saint-Etienne, 2015.

[57] A. G. Nasibulin, D. P. Brown, P. Queipo, D. Gonzalez, H. Jiang, and E. I. Kauppinen, "An essential role of CO₂ and H₂O during single-walled CNT synthesis from carbon monoxide," *Chem. Phys. Lett.*, vol. 417, no. 1–3, pp. 179–184, 2006.

- [58] Y. Tian *et al.*, "Cutting floating single-walled carbon nanotubes with a 'CO₂ blade,'" *Carbon N. Y.*, vol. 143, pp. 481–486, Mar. 2019.
- [59] O. S. S. Rabinovich, V. A. a. Borodulya, A. N. N. Blinova, V. L. L. Kuznetsov, A. I. I. Delidovich, and D. V. V. Krasnikov, "Simulation of transient processes of the catalytic synthesis of carbon nanotubes in a fluidized bed," *Theor. Found. Chem. Eng.*, vol. 48, no. 1, pp. 1–12, 2014.
- [60] E. Pigos, E. S. Penev, M. a. Ribas, R. Sharma, B. I. Yakobson, and A. R. Harutyunyan, "Carbon nanotube nucleation driven by catalyst morphology dynamics," *ACS Nano*, vol. 5, no. 12, pp. 10096–10101, 2011.
- [61] V. L. V. L. Kuznetsov, D. V. D. V. Krasnikov, A. N. A. N. Schmakov, and K. V. K. V. Elumeeva, "In situ and ex situ time resolved study of multi-component Fe-Co oxide catalyst activation during MWNT synthesis," *Phys. Status Solidi Basic Res.*, vol. 249, no. 12, pp. 2390–2394, 2012.
- [62] A. Monzon, G. Lolli, S. Cosma, S. B. Mohamed, and D. E. Resasco, "Kinetic Modeling of the SWNT Growth by CO Disproportionation on CoMo Catalysts," *J. Nanosci. Nanotechnol.*, vol. 8, no. 11, pp. 6141–6152, 2008.
- [63] V. Kurochkin and L. Kravchenko, "Numerical Simulation Of Impact Of The Spark Discharge Parameters And Electrode Material On The Intensity Of Spectral Lines In The Emission Spectral Analysis," *METHODS OBJECTS Chem. Anal.*, vol. 10, no. 4, pp. 195–201, 2015.
- [64] M. He *et al.*, "Growth modes and chiral selectivity of single-walled carbon nanotubes," *Nanoscale*, vol. 10, no. 14, pp. 6744–6750, 2018.
- [65] K. Mustonen, P. Laiho, A. Kaskela, T. Susi, A. G. Nasibulin, and E. I. Kauppinen, "Uncovering the ultimate performance of single-walled carbon nanotube films as transparent conductors," *Appl. Phys. Lett.*, vol. 107, no. 14, p. 143113, 2015.
- [66] A. Kaskela *et al.*, "Aerosol-synthesized SWCNT networks with tunable conductivity and transparency by a dry transfer technique," *Nano Lett.*, vol. 10, no. 11, pp. 4349–4355, 2010.
- [67] A. G. Nasibulin *et al.*, "Studies on mechanism of single-walled carbon nanotube formation," in *Journal of Nanoscience and Nanotechnology*, 2006, vol. 6, no. 5, pp. 1233–1246.
- [68] Y. Liao *et al.*, "Direct Synthesis of Colorful Single-Walled Carbon Nanotube Thin Films (supporting information)," *J. Am. Chem. Soc.*, vol. 140, no. 31, pp. 8–11, 2018.
- [69] Y. Tian *et al.*, "Growth of single-walled carbon nanotubes with controlled diameters and lengths by an aerosol method," *Carbon N. Y.*, vol. 49, no. 14, pp. 4636–4643, 2011.
- [70] A. Jorio and A. G. S. Filho, "Raman Studies of Carbon Nanostructures," *Annu. Rev. Mater. Res.*, vol. 46, pp. 357–382, 2016.
- [71] D. V. Krasnikov *et al.*, "Influence of the Growth Temperature on the Defective Structure of the Multi-Walled Carbon Nanotubes," *Phys. Status Solidi*, vol. 1700255, p. 1700255, Sep. 2017.

- [72] V. L. V. L. Kuznetsov *et al.*, "Raman spectra for characterization of defective CVD multi-walled carbon nanotubes," *Phys. Status Solidi*, vol. 251, no. 12, pp. 2444–2450, 2014.
- [73] D. V Krasnikov *et al.*, "Influence of the Growth Temperature on the Defective Structure of the Multi-Walled Carbon Nanotubes," *Phys. status solidi*, vol. 255, no. 1, p. 1700255, 2018.
- [74] D. V. Krasnikov *et al.*, "A spark discharge generator for scalable aerosol CVD synthesis of single-walled carbon nanotubes with tailored characteristics," *Chem. Eng. J.*, pp. 462–470, Apr. 2019.
- [75] K. Hata, D. Futaba, K. Mizuno, T. Namai, M. Yumura, and S. Iijima, "Water-assisted highly efficient synthesis of impurity-free single-walled carbon nanotubes.," *Science*, vol. 306, no. 5700, pp. 1362–1364, 2004.
- [76] O. Rabinovich, A. Tsytzenka (Blinova), V. Kuznetsov, S. Moseenkov, and D. Krasnikov, "A model for catalytic synthesis of carbon nanotubes in a fluidized-bed reactor: Effect of reaction heat," *Chem. Eng. J.*, vol. 329, pp. 305–311, 2017.
- [77] Z. Zhang, Y. Hong, B. Hou, Z. Zhang, M. Negahban, and J. Zhang, "Accelerated discoveries of mechanical properties of graphene using machine learning and high-throughput computation," *Carbon N. Y.*, vol. 148, pp. 115–123, Jul. 2019.
- [78] Z. Yang, W.-M. Qiao, and X.-Y. Liang, "Modelling and optimization of the pore structure of carbon aerogels using an artificial neural network," *NEW CARBON Mater.*, vol. 32, no. 1, 2017.
- [79] Q. Zhang, N. Wei, P. Laiho, and E. I. Kauppinen, "Recent Developments in Single-Walled Carbon Nanotube Thin Films Fabricated by Dry Floating Catalyst Chemical Vapor Deposition," *Top. Curr. Chem.*, vol. 375, no. 6, pp. 1–30, 2017.
- [80] L. Taylor and G. Nitschke, "Improving Deep Learning with Generic Data Augmentation," in *Proceedings of the 2018 IEEE Symposium Series on Computational Intelligence, SSCI 2018*, 2019, pp. 1542–1547.
- [81] F. Chollet, "Keras: Deep learning library for theano and tensorflow," *URL <https://keras.io/k>*, vol. 7, no. 8, p. T1, 2015.
- [82] D. P. Kingma and J. Ba, "Adam: A method for stochastic optimization," *arXiv Prepr. arXiv1412.6980*, 2014.
- [83] D. M. Hawkins, "The Problem of Overfitting," *J. Chem. Inf. Comput. Sci.*, vol. 44, no. 1, pp. 1–12, Jan. 2004.
- [84] J. F. Moulder, W. F. Stickle, P. E. Sobol, and K. D. Bomben, *Handbook of X-ray photoelectron spectroscopy*. Physical Electronics, Inc., 1995.
- [85] A. Rogalski, "History of infrared detectors," *Opto-Electronics Rev.*, vol. 20, no. 3, pp. 279–308, 2012.
- [86] A. Rogalski, "Infrared detectors: An overview," *Infrared Phys. Technol.*, vol. 43, no. 3–5, pp. 187–210, 2002.
- [87] S. Smuk, K. Yu, and M. Petrosenko, "Solomitskii D. Infrakrasnye datchiki dlinnovolnovogo diapazona na kvantovykh yamakh," *Kompon. i tekhnologii*,

no. 1, pp. 152–157, 2014.

[88] G. D. Ado Jorio and M. S. Dresselhaus, *Carbon nanotubes: Advanced topics in the synthesis, structure, properties and applications*, vol. 11, no. 3. 2008.

[89] R. Lu, Z. Li, G. Xu, and J. Z. Wu, “Suspending single-wall carbon nanotube thin film infrared bolometers on microchannels,” *Appl. Phys. Lett.*, vol. 94, no. 16, pp. 92–95, 2009.

[90] B. Pradhan, K. Setyowati, H. Liu, D. H. Waldeck, and J. Chen, “Carbon nanotube-polymer nanocomposite infrared sensor,” *Nano Lett.*, vol. 8, no. 4, pp. 1142–1146, 2008.

[91] A. E. Aliev, “Bolometric detector on the basis of single-wall carbon nanotube/polymer composite,” *Infrared Phys. Technol.*, vol. 51, no. 6, pp. 541–545, 2008.

[92] A. Y. Glamazda, V. A. Karachevtsev, W. B. Euler, and I. A. Levitsky, “Achieving high mid-IR bolometric responsivity for anisotropic composite materials from carbon nanotubes and polymers,” *Adv. Funct. Mater.*, vol. 22, no. 10, pp. 2177–2186, 2012.

[93] G. Vera-Reveles, T. J. Simmons, M. Bravo-Sánchez, M. A. Vidal, H. Navarro-Contreras, and F. J. González, “High-sensitivity bolometers from self-oriented single-walled carbon nanotube composites,” *ACS Appl. Mater. Interfaces*, vol. 3, no. 8, pp. 3200–3204, 2011.

[94] A. Rogalski, “Organic field-effect transistors,” *Opto-Electronics Rev.*, vol. 18, no. 2, pp. 121–136, 2010.

[95] Q. Wang, T. Chen, B. Zhang, M. Li, Y. Lu, and K. P. Chen, “All-fiber passively mode-locked thulium-doped fiber ring laser using optically deposited graphene saturable absorbers,” *Appl. Phys. Lett.*, vol. 102, no. 13, p. 131117, 2013.

[96] B. Fu, Y. Hua, X. Xiao, H. Zhu, Z. Sun, and C. Yang, “Broadband graphene saturable absorber for pulsed fiber lasers at 1, 1.5, and 2 μm ,” *IEEE J. Sel. Top. Quantum Electron.*, vol. 20, no. 5, pp. 411–415, 2014.

[97] J. Sotor, G. Sobon, M. Kowalczyk, W. Macherzynski, P. Paletko, and K. M. Abramski, “Ultrafast thulium-doped fiber laser mode locked with black phosphorus,” *Opt. Lett.*, vol. 40, no. 16, pp. 3885–3888, 2015.

[98] H. Yu, X. Zheng, K. Yin, and T. Jiang, “Thulium/holmium-doped fiber laser passively mode locked by black phosphorus nanoplatelets-based saturable absorber,” *Appl. Opt.*, vol. 54, no. 34, pp. 10290–10294, 2015.

[99] M. Jung *et al.*, “A femtosecond pulse fiber laser at 1935 nm using a bulk-structured Bi₂Te₃ topological insulator,” *Opt. Express*, vol. 22, no. 7, pp. 7865–7874, 2014.

[100] Y. Cui, F. Lu, and X. Liu, “MoS₂-clad microfiber laser delivering conventional, dispersion-managed and dissipative solitons,” *Sci. Rep.*, vol. 6, p. 30524, 2016.

[101] J. Koo, J. Park, J. Lee, Y. M. Jhon, and J. H. Lee, “Femtosecond harmonic mode-locking of a fiber laser at 3.27 GHz using a bulk-like, MoSe₂-based

- saturable absorber," *Opt. Express*, vol. 24, no. 10, pp. 10575–10589, 2016.
- [102] S. Yamashita, Y. Saito, and J. H. Choi, *Carbon nanotubes and graphene for photonic applications*. Elsevier, 2013.
- [103] S. Y. Set, H. Yaguchi, Y. Tanaka, and M. Jablonski, "Laser mode locking using a saturable absorber incorporating carbon nanotubes," *J. Light Technol.*, vol. 22, no. 1, p. 51, 2004.
- [104] Z. Yu, Y. Wang, X. Zhang, X. Dong, J. Tian, and Y. Song, "A 66 fs highly stable single wall carbon nanotube mode locked fiber laser," *Laser Phys.*, vol. 24, no. 1, p. 15105, 2013.
- [105] D. Ma, Y. Cai, C. Zhou, W. Zong, L. Chen, and Z. Zhang, "37.4 fs pulse generation in an Er: fiber laser at a 225 MHz repetition rate," *Opt. Lett.*, vol. 35, no. 17, pp. 2858–2860, 2010.
- [106] H. D. Yun *et al.*, "High performance all-carbon composite transparent electrodes containing uniform carbon nanotube networks," *J. Alloys Compd.*, vol. 675, pp. 37–45, 2016.
- [107] S. Y. Ryu, K.-S. Kim, J. Kim, and S. Kim, "Degradation of optical properties of a film-type single-wall carbon nanotubes saturable absorber (SWNT-SA) with an Er-doped all-fiber laser," *Opt. Express*, vol. 20, no. 12, pp. 12966–12974, 2012.
- [108] S. F. Bartolucci *et al.*, "Laser-induced thermo-oxidative degradation of carbon nanotube/polypropylene nanocomposites," *Compos. Sci. Technol.*, vol. 105, pp. 166–173, 2014.
- [109] S. Kivistö *et al.*, "Carbon nanotube films for ultrafast broadband technology," *Opt. Express*, vol. 17, no. 4, pp. 2358–2363, 2009.
- [110] Y.-W. Song, S. Yamashita, E. Einarsson, and S. Maruyama, "All-fiber pulsed lasers passively mode locked by transferable vertically aligned carbon nanotube film," *Opt. Lett.*, vol. 32, no. 11, pp. 1399–1401, 2007.
- [111] Y.-W. Song, S. Yamashita, and S. Maruyama, "Single-walled carbon nanotubes for high-energy optical pulse formation," *Appl. Phys. Lett.*, vol. 92, no. 2, p. 21115, 2008.
- [112] H. Jeong, S. Y. Choi, F. Rotermund, Y.-H. Cha, D.-Y. Jeong, and D.-I. Yeom, "All-fiber mode-locked laser oscillator with pulse energy of 34 nJ using a single-walled carbon nanotube saturable absorber," *Opt. Express*, vol. 22, no. 19, pp. 22667–22672, 2014.
- [113] Y.-W. Song, S. Yamashita, C. S. Goh, and S. Y. Set, "Carbon nanotube mode lockers with enhanced nonlinearity via evanescent field interaction in D-shaped fibers," *Opt. Lett.*, vol. 32, no. 2, pp. 148–150, 2007.
- [114] H. H. Liu, K. K. Chow, S. Yamashita, and S. Y. Set, "Carbon-nanotube-based passively Q-switched fiber laser for high energy pulse generation," *Opt. Laser Technol.*, vol. 45, pp. 713–716, 2013.
- [115] S. Y. Choi, H. Jeong, B. H. Hong, F. Rotermund, and D.-I. Yeom, "All-fiber dissipative soliton laser with 10.2 nJ pulse energy using an evanescent field

interaction with graphene saturable absorber," *Laser Phys. Lett.*, vol. 11, no. 1, p. 15101, 2013.

[116] J. Boguslawski *et al.*, "Mode-locked Er-doped fiber laser based on liquid phase exfoliated Sb₂Te₃ topological insulator," *Laser Phys.*, vol. 24, no. 10, p. 105111, 2014.

[117] C. S. Jun *et al.*, "Low noise GHz passive harmonic mode-locking of soliton fiber laser using evanescent wave interaction with carbon nanotubes," *Opt. Express*, vol. 19, no. 20, pp. 19775–19780, 2011.

[118] J. Ko, H. Jeong, S. Y. Choi, F. Rotermund, D.-I. Yeom, and B. Y. Kim, "Single-walled carbon nanotubes on side polished fiber as a universal saturable absorber for various laser output states," *Curr. Appl. Phys.*, vol. 17, no. 1, pp. 37–40, 2017.

[119] H. Jeong, S. Y. Choi, F. Rotermund, and D.-I. Yeom, "Pulse width shaping of passively mode-locked soliton fiber laser via polarization control in carbon nanotube saturable absorber," *Opt. Express*, vol. 21, no. 22, p. 27011, Nov. 2013.

[120] A. Cusano, A. Cutolo, and J. Albert, *Fiber Bragg grating sensors: recent advancements, industrial applications and market exploitation*. Bentham Science Publishers, 2011.

[121] H. G. Limberger, N. H. Ky, D. M. Costantini, R. P. Salathé, C. A. P. Muller, and G. R. Fox, "Efficient miniature fiber-optic tunable filter based on intracore Bragg grating and electrically resistive coating," *IEEE Photonics Technol. Lett.*, vol. 10, no. 3, pp. 361–363, 1998.

[122] A. D. Kersey *et al.*, "Fiber grating sensors," *J. Light. Technol.*, vol. 15, no. 8, pp. 1442–1463, 1997.

[123] K. Kalli *et al.*, "Development of an electrically tuneable Bragg grating filter in polymer optical fibre operating at 1.55 μm ," *Meas. Sci. Technol.*, vol. 18, no. 10, p. 3155, 2007.

[124] Y. C. Tan, W. B. Ji, V. Mamidala, K. K. Chow, and S. C. Tjin, "Carbon-nanotube-deposited long period fiber grating for continuous refractive index sensor applications," *Sensors Actuators B Chem.*, vol. 196, pp. 260–264, 2014.

APPENDIX: SWCNT SYNTHESIS CONDITIONS

Table S1: Dataset used for the ANN calculations.

| Sample | T(K) | INPUT | | | | OUTPUT | | |
|--------|------|--------|----------------------|----------|----------------------|--------------------------------|----------|---------|
| | | Pco(%) | Pco ₂ (%) | Pcat(%) | t _{res} (s) | I _g /I _p | Dent(nm) | Yield |
| 1 | 1073 | 1.00 | 0.000 | 1.78E-06 | 0.57 | 4.5E+00 | 1.0 | 3.2E-03 |
| 2 | 1073 | 1.00 | 0.005 | 1.78E-06 | 0.57 | 7.4E+00 | 1.0 | 7.4E-03 |
| 3 | 1073 | 0.99 | 0.010 | 1.78E-06 | 0.57 | 1.1E+01 | 1.1 | 3.4E-02 |
| 4 | 1073 | 0.99 | 0.015 | 1.78E-06 | 0.57 | 8.6E+01 | 1.2 | 1.3E-01 |
| 5 | 1073 | 0.98 | 0.018 | 1.78E-06 | 0.57 | 1.8E+02 | 1.9 | 2.4E-01 |
| 6 | 1073 | 0.98 | 0.020 | 1.78E-06 | 0.57 | 2.6E+02 | 1.7 | 4.2E-01 |
| 7 | 1073 | 0.98 | 0.022 | 1.78E-06 | 0.57 | 2.3E+02 | 1.7 | 1.5E-01 |
| 8 | 1073 | 0.98 | 0.025 | 1.78E-06 | 0.57 | 1.7E+02 | 2.0 | 4.7E-02 |
| 9 | 1073 | 0.97 | 0.030 | 1.78E-06 | 0.57 | 1.3E+02 | 1.9 | 8.3E-02 |
| 10 | 1098 | 1.00 | 0.000 | 1.78E-06 | 0.57 | 9.0E+00 | 1.1 | 1.2E-02 |
| 11 | 1098 | 1.00 | 0.005 | 1.78E-06 | 0.57 | 7.5E+01 | 1.1 | 6.5E-02 |
| 12 | 1098 | 0.99 | 0.008 | 1.78E-06 | 0.57 | 1.3E+02 | 1.3 | 1.8E-01 |
| 13 | 1098 | 0.99 | 0.010 | 1.78E-06 | 0.57 | 3.2E+02 | 1.4 | 3.9E-01 |
| 14 | 1098 | 0.99 | 0.012 | 1.78E-06 | 0.57 | 4.4E+02 | 1.7 | 6.3E-01 |
| 15 | 1098 | 0.99 | 0.013 | 1.78E-06 | 0.57 | 2.9E+02 | 1.8 | 3.8E-01 |
| 16 | 1098 | 0.99 | 0.014 | 1.78E-06 | 0.57 | 3.2E+02 | 1.9 | 3.9E-01 |
| 17 | 1098 | 0.99 | 0.015 | 1.78E-06 | 0.57 | 2.5E+02 | 1.9 | 2.4E-01 |
| 18 | 1098 | 0.98 | 0.016 | 1.78E-06 | 0.57 | 2.3E+02 | 1.8 | 2.3E-01 |
| 19 | 1098 | 0.98 | 0.018 | 1.78E-06 | 0.57 | 1.6E+02 | 1.7 | 1.7E-01 |
| 20 | 1098 | 0.98 | 0.020 | 1.78E-06 | 0.57 | 1.6E+02 | 1.6 | 1.6E-01 |
| 21 | 1098 | 0.98 | 0.025 | 1.78E-06 | 0.57 | 1.1E+02 | 1.4 | 2.4E-01 |
| 22 | 1098 | 0.97 | 0.030 | 1.78E-06 | 0.57 | 9.2E+01 | 1.3 | 3.8E-01 |
| 23 | 1123 | 1.00 | 0.000 | 1.78E-06 | 0.57 | 3.4E+01 | 1.1 | 3.1E-02 |
| 24 | 1123 | 0.98 | 0.020 | 1.78E-06 | 0.57 | 9.6E+01 | - | 4.0E-01 |
| 25 | 1123 | 1.00 | 0.002 | 1.78E-06 | 0.57 | 3.3E+01 | 1.1 | 5.2E-02 |
| 26 | 1123 | 1.00 | 0.005 | 1.78E-06 | 0.57 | 3.1E+01 | 1.1 | 1.2E-01 |
| 27 | 1123 | 0.99 | 0.008 | 1.78E-06 | 0.57 | 4.3E+01 | 1.2 | 2.2E-01 |
| 28 | 1123 | 0.99 | 0.010 | 1.78E-06 | 0.57 | 1.3E+02 | 1.3 | 4.5E-01 |
| 29 | 1123 | 0.99 | 0.012 | 1.78E-06 | 0.57 | 3.3E+02 | 1.5 | 8.6E-01 |
| 30 | 1123 | 0.99 | 0.013 | 1.78E-06 | 0.57 | 2.6E+02 | 1.8 | 6.3E-01 |
| 31 | 1123 | 0.99 | 0.014 | 1.78E-06 | 0.57 | 1.9E+02 | 1.8 | 5.4E-01 |
| 32 | 1123 | 0.99 | 0.015 | 1.78E-06 | 0.57 | 1.1E+02 | 1.7 | 5.0E-01 |
| 33 | 1123 | 0.98 | 0.018 | 1.78E-06 | 0.57 | 9.2E+01 | - | 4.5E-01 |
| 34 | 1123 | 0.98 | 0.025 | 1.78E-06 | 0.57 | 5.1E+00 | - | 3.4E-01 |
| 35 | 1153 | 0.72 | 0.000 | 2.52E-06 | 0.24 | 6.1E+00 | 1.1 | 1.7E+00 |
| 36 | 1153 | 0.72 | 0.002 | 2.51E-06 | 0.24 | 6.5E+00 | 1.1 | 1.4E+00 |
| 37 | 1153 | 0.71 | 0.003 | 2.51E-06 | 0.24 | 6.9E+00 | 1.1 | 2.0E+00 |
| 38 | 1153 | 0.71 | 0.005 | 2.50E-06 | 0.24 | 9.0E+00 | 1.1 | 2.6E+00 |
| 39 | 1153 | 0.71 | 0.007 | 2.50E-06 | 0.24 | 1.3E+01 | 1.1 | 2.8E+00 |
| 40 | 1153 | 0.71 | 0.008 | 2.50E-06 | 0.24 | 1.7E+01 | 1.2 | 2.9E+00 |
| 41 | 1153 | 0.71 | 0.010 | 2.49E-06 | 0.24 | 2.0E+01 | 1.3 | 3.6E+00 |
| 42 | 1153 | 0.71 | 0.012 | 2.49E-06 | 0.23 | 1.9E+01 | 1.2 | 1.4E+00 |
| 43 | 1153 | 0.71 | 0.013 | 2.48E-06 | 0.23 | 1.9E+01 | 1.2 | 1.4E+00 |
| 44 | 1153 | 0.71 | 0.015 | 2.48E-06 | 0.23 | 1.8E+01 | 1.1 | 1.4E+00 |
| 45 | 1153 | 0.70 | 0.016 | 2.48E-06 | 0.23 | 1.9E+01 | 1.2 | 1.1E+00 |
| 46 | 1153 | 0.70 | 0.018 | 2.47E-06 | 0.23 | 3.3E+01 | 1.3 | 1.3E+00 |
| 47 | 1153 | 0.70 | 0.020 | 2.47E-06 | 0.23 | - | 1.4 | 1.0E+00 |
| 48 | 1173 | 1.00 | 0.000 | 1.78E-06 | 0.57 | 7.4E+01 | 1.1 | 1.0E-01 |
| 49 | 1173 | 1.00 | 0.002 | 1.78E-06 | 0.57 | 5.7E+01 | 1.0 | 1.8E-01 |
| 44 | 1153 | 0.71 | 0.015 | 2.48E-06 | 0.23 | 1.8E+01 | 1.1 | 1.4E+00 |
| 50 | 1173 | 1.00 | 0.005 | 1.78E-06 | 0.57 | 6.5E+01 | 1.0 | 3.5E-01 |
| 51 | 1173 | 0.99 | 0.008 | 1.78E-06 | 0.57 | 7.5E+01 | 1.1 | 6.0E-01 |
| 52 | 1173 | 0.99 | 0.010 | 1.78E-06 | 0.57 | 1.1E+02 | 1.3 | 9.4E-01 |
| 53 | 1173 | 0.99 | 0.012 | 1.78E-06 | 0.57 | 2.0E+02 | 1.5 | 1.2E+00 |
| 54 | 1173 | 0.99 | 0.015 | 1.78E-06 | 0.57 | 1.7E+02 | 1.6 | 1.3E+00 |
| 55 | 1173 | 0.98 | 0.018 | 1.78E-06 | 0.57 | 4.4E+01 | 1.4 | 6.7E-01 |
| 56 | 1173 | 0.98 | 0.022 | 1.78E-06 | 0.57 | 5.8E+01 | 1.2 | 6.8E-01 |
| 57 | 1173 | 0.98 | 0.025 | 1.78E-06 | 0.57 | 3.0E+01 | 1.2 | 7.0E-01 |
| 58 | 1223 | 1.00 | 0.000 | 1.78E-06 | 0.57 | 5.2E+01 | 1.1 | 2.8E-01 |
| 59 | 1223 | 0.98 | 0.020 | 1.78E-06 | 0.57 | 2.5E+01 | - | 5.1E-01 |

| | | | | | | | | |
|----|------|------|-------|----------|------|---------|-----|---------|
| 60 | 1223 | 1.00 | 0.002 | 1.78E-06 | 0.57 | 6.2E+01 | 1.1 | 3.5E-01 |
| 61 | 1223 | 0.98 | 0.022 | 1.78E-06 | 0.57 | 2.6E+01 | - | 5.0E-01 |
| 62 | 1223 | 1.00 | 0.005 | 1.78E-06 | 0.57 | 4.9E+01 | 1.1 | 5.3E-01 |
| 63 | 1223 | 0.99 | 0.008 | 1.78E-06 | 0.57 | 5.3E+01 | 1.2 | 6.7E-01 |
| 64 | 1223 | 0.99 | 0.010 | 1.78E-06 | 0.57 | 1.1E+02 | 1.3 | 9.8E-01 |
| 65 | 1223 | 0.99 | 0.012 | 1.78E-06 | 0.57 | 1.5E+02 | 1.4 | 1.2E+00 |
| 66 | 1223 | 0.99 | 0.015 | 1.78E-06 | 0.57 | 3.9E+01 | - | 1.3E+00 |
| 67 | 1223 | 0.98 | 0.018 | 1.78E-06 | 0.57 | 3.9E+01 | - | 5.4E-01 |
| 68 | 1253 | 0.72 | 0.000 | 2.52E-06 | 0.24 | 8.3E+00 | 1.0 | 2.3E+00 |
| 69 | 1253 | 0.72 | 0.002 | 2.51E-06 | 0.24 | 9.1E+00 | 1.0 | 2.1E+00 |
| 70 | 1253 | 0.71 | 0.003 | 2.51E-06 | 0.24 | 1.1E+01 | 1.1 | 2.2E+00 |
| 71 | 1253 | 0.71 | 0.005 | 2.50E-06 | 0.24 | 9.6E+00 | 1.1 | 2.2E+00 |
| 72 | 1253 | 0.71 | 0.007 | 2.50E-06 | 0.24 | 9.0E+00 | 1.1 | 2.2E+00 |
| 73 | 1253 | 0.71 | 0.008 | 2.50E-06 | 0.24 | 1.4E+01 | 1.2 | 2.3E+00 |
| 74 | 1253 | 0.71 | 0.010 | 2.49E-06 | 0.24 | 2.0E+01 | 1.1 | 2.4E+00 |
| 75 | 1253 | 0.71 | 0.012 | 2.49E-06 | 0.23 | 3.0E+01 | 1.1 | 2.1E+00 |
| 76 | 1253 | 0.71 | 0.013 | 2.48E-06 | 0.23 | 4.0E+01 | 1.1 | 2.2E+00 |
| 77 | 1253 | 0.71 | 0.015 | 2.48E-06 | 0.23 | 3.9E+01 | 1.2 | 2.1E+00 |
| 78 | 1253 | 0.70 | 0.016 | 2.48E-06 | 0.23 | 4.4E+01 | 1.2 | 1.9E+00 |
| 79 | 1253 | 0.70 | 0.018 | 2.47E-06 | 0.23 | 3.0E+01 | 1.2 | 2.1E+00 |
| 80 | 1253 | 0.70 | 0.020 | 2.47E-06 | 0.23 | 2.4E+01 | 1.2 | 1.8E+00 |
| 81 | 1273 | 1.00 | 0.000 | 1.78E-06 | 0.57 | 5.5E+01 | 1.1 | 3.6E-01 |
| 82 | 1273 | 1.00 | 0.002 | 1.78E-06 | 0.57 | 1.7E+01 | 1.1 | 4.3E-01 |
| 83 | 1273 | 1.00 | 0.005 | 1.78E-06 | 0.57 | 4.7E+01 | 1.1 | 6.6E-01 |
| 84 | 1273 | 0.99 | 0.008 | 1.78E-06 | 0.57 | 5.0E+01 | 1.1 | 7.7E-01 |
| 85 | 1273 | 0.99 | 0.010 | 1.78E-06 | 0.57 | 5.0E+01 | 1.2 | 9.9E-01 |
| 86 | 1273 | 0.99 | 0.012 | 1.78E-06 | 0.57 | 4.6E+01 | 1.2 | 1.2E+00 |
| 87 | 1273 | 0.99 | 0.015 | 1.78E-06 | 0.57 | 2.7E+01 | 1.2 | 1.0E+00 |
| 88 | 1273 | 0.98 | 0.018 | 1.78E-06 | 0.57 | 1.9E+01 | - | 9.2E-01 |
| 89 | 1323 | 1.00 | 0.000 | 1.78E-06 | 0.57 | 4.7E+01 | 1.1 | 6.2E-01 |
| 90 | 1323 | 0.98 | 0.020 | 1.78E-06 | 0.57 | 1.6E+01 | - | - |
| 91 | 1323 | 1.00 | 0.004 | 1.78E-06 | 0.57 | 3.8E+01 | 1.1 | 6.7E-01 |
| 92 | 1323 | 0.99 | 0.006 | 1.78E-06 | 0.57 | 3.9E+01 | 1.1 | 7.5E-01 |
| 93 | 1323 | 0.99 | 0.008 | 1.78E-06 | 0.57 | 6.3E+01 | 1.2 | 8.3E-01 |
| 94 | 1323 | 0.99 | 0.010 | 1.78E-06 | 0.57 | 2.9E+01 | 1.2 | 9.2E-01 |
| 95 | 1323 | 0.99 | 0.012 | 1.78E-06 | 0.57 | 2.8E+01 | 1.1 | 9.5E-01 |
| 96 | 1323 | 0.99 | 0.014 | 1.78E-06 | 0.57 | 2.5E+01 | 1.1 | 8.8E-01 |
| 97 | 1323 | 0.98 | 0.016 | 1.78E-06 | 0.57 | 2.2E+01 | 1.1 | 1.1E+00 |
| 98 | 1323 | 0.98 | 0.018 | 1.78E-06 | 0.57 | 1.3E+01 | - | - |

Single-walled carbon nanotubes (SWCNTs) are of a unique family of materials emerging high-performance applications in electronics and optoelectronics. However, despite significant progress over the last 25 years, the problem of SWCNT production with tailored characteristics, the absence of the growth models and post-synthesis methods to improve specific SWCNT properties are still the main barriers towards a wide range of applications. The methods of the SWCNT synthesis, data processing and SWCNT treatment developed so far are still not fully optimized.

In the current thesis, the abovementioned problems were addressed with the following demonstration of advanced applications of SWCNT films:

A new reactor for the aerosol CVD growth of SWCNTs equipped with a spark discharge generator of catalyst nanoparticles was developed. The design proposed resulted in a robust apparatus when compared with the ferrocene CVD reactor. The stability and scalability of the SWCNT synthesis are the main benefits of the spark discharge generator.

An advanced control on the diameter distribution, defectiveness, and the yield for the first time was achieved through the use of the artificial neural networks (ANN). This allowed us to achieve a precise control towards mutual relation between the reactor parameters and key SWCNT characteristics. The methodology proposed can help with adjusting the diameter distribution, yield and quality of SWCNTs with prediction error 4%, 14%, 23% respectively for very a limited data set.

A novel technique for the post-synthesis improvement of electro-optical characteristics of SWCNT films by a laser treatment was proposed. In this process by a short pulse laser irradiation, the transparency of SWCNT films increases without any changes in conductivity presumably due to the oxidation of the catalyst particles. We improved transparency by 4%, and decreased equivalent sheet resistance by 21%.

All developed techniques and methods contributed to the synthesis of SWCNTs with defined characteristics open a new possibility for their applications. Thesis work includes three different electro-optical devices with advanced performance: I) a bolometer based on a freestanding SWCNT film showing response time of 2.6 ms at room temperature and 1 mbar (several times faster than the corresponding industrially applied devices); II) an SWCNT-based heating element of fiber Bragg grid for smooth tuning of the resonant wavelength and a stable laser signal; III) a saturable absorber based on SWCNT films showing femtosecond pulse generation and low degradation rate.



ISBN 978-952-60-8739-9 (printed)
ISBN 978-952-60-8740-5 (pdf)
ISSN 1799-4934 (printed)
ISSN 1799-4942 (pdf)
Aalto University
School of Science
Department of Applied Physics
www.aalto.fi

**BUSINESS +
ECONOMY**

**ART +
DESIGN +
ARCHITECTURE**

**SCIENCE +
TECHNOLOGY**

CROSSOVER

**DOCTORAL
DISSERTATIONS**